2012-06-06

Active Noise Control of a Centrifugal Fan Mounted in a Mock Laptop Enclosure

John J. Esplin
Brigham Young University - Provo

BYU ScholarsArchive Citation

Esplin, John J., "Active Noise Control of a Centrifugal Fan Mounted in a Mock Laptop Enclosure" (2012). *All Theses and Dissertations*. 3577.
https://scholarsarchive.byu.edu/etd/3577

Active Noise Control of a Centrifugal Fan

Mounted in a Mock Laptop Enclosure

J. James Esplin

A thesis submitted to the faculty of
Brigham Young University
in partial fulfillment of the requirements for the degree of

Master of Science

Scott D. Sommerfeldt, Chair
Kent L. Gee
Jonathan D. Blotter

Department of Physics and Astronomy

Brigham Young University

June 2012

ABSTRACT

Active Noise Control of a Centrifugal Fan Mounted in a Mock Laptop Enclosure

J. James Esplin
Department of Physics and Astronomy, BYU
Master of Science

Noise from information technology (IT) equipment is a significant problem in today's modern society. Active Noise Control (ANC) has shown promise in reducing the effect of IT fan noise on users. Though ANC has been applied to axial fans (such as those found in desktop computers), it has not been applied to centrifugal fans, such as those found in laptop computers. This work applies an ANC method to a centrifugal fan mounted in a mock laptop enclosure. This method is applied in four steps. First, secondary sources are placed in the vicinity of the fan. Second, an accurate model of the radiation from the fan and secondary sources is constructed. Third, the total power radiated from this system is minimized. This creates nodal lines in the vicinity of the fan. Fourth, ANC error sensors are placed on the nodal lines predicted by the model. This creates these nodal lines experimentally, thus creating the minimum power condition. The noise from the exhaust and inlets of the fan will first be controlled individually. Then the method will be applied to the combined system. Global sound power radiation will be measured in all cases.

Keywords: [active noise control, ANC, centrifugal fan, sound power, laptop]

ACKNOWLEDGMENTS

I’d like to thank my graduate advisor, Dr. Scott Sommerfeldt, for all of his work with me over the course of this project. Without him, this document and the work behind it would not have been possible.

I’d like to thank my graduate committee members, Dr. Kent Gee and Dr. Johnathan Blotter, for their help, both during the project and in the writing of this thesis.

I’d like to thank John K. Boyle for his invaluable assistance over the course of this project. Many of the results of this work are due in part to him.

I’d like to thank my fellow acoustics graduate students at BYU for their friendship and support. I will miss the many times we stood in front of a whiteboard together with dry-erase markers in hand, helping me with my homework or my research.

Finally, I’d like to thank my wife, daughter, and son. Their encouragement has helped me push through what would have otherwise been near insurmountable obstacles.

Table of Contents

List of Figures & Tables

Chapter 1

Introduction

Noise from information technology (IT) equipment is a significant problem in today's contemporary society.[1] From computers and projectors to printers and copiers, IT equipment noise permeates many facets of our everyday lives in a technology-driven world. Due to its prevalence, there is an intense interest in reducing, controlling, and eliminating IT equipment noise in its many forms, including noise produced by fans of IT equipment.[2] Active Noise Control (ANC) has shown promise in reducing IT fan noise.

1.1 Active Noise Control

Active Noise Control is the acoustician's equivalent of "fighting fire with fire." In essence, it uses generated sound from one or more loudspeakers to reduce or eliminate the unwanted sound radiating from the noise source. This is done through three different techniques.

The first technique is destructive wave interference.[3] This is where a primary source (or noise source) is controlled by a secondary source (or control source) at a specific point in space. This technique is rather easy to design and is very robust. However, it only succeeds in reducing/eliminating the unwanted noise in a specific region. This is called *local control*. An error sensor is required in the center of the controlled region, which is typically in the far-field of the primary and secondary sources.

The second technique is mutual coupling.[3] This is where closely-spaced sources modify each other's radiation impedance. This results in a net reduction of sound power in all directions, or *global control.* The amount of power radiated by this scenario depends on how close the secondary source is to the primary source. For one monopole secondary source in free field it is given by $\Pi_{min} = \Pi_p \left(1 - \frac{\sin(kd)}{kd}\right)$, where Π_{min} is the minimized sound power, Π_p is the uncontrolled power, k is the wavenumber, and d is the distance between the two sources (see Appendix B for a more detailed explanation). Thus, sources must be closely spaced relative to a wavelength for global control to occur. With this technique, error sensors can be placed in the far-field or the near-field of the primary and secondary sources. Though more difficult to design, this can lead to a more compact (and practical) system.

The third technique is modal coupling.[3] This is where sources modify each other's radiation impedance through the natural modes of an enclosure, again resulting in global control. Since this method utilizes the modes of the enclosure, sources do not have to be closely spaced relative to a wavelength. However, this technique can only be used in an enclosed sound field. It can be very effective for a low modal density sound field, but largely ineffective otherwise. Like mutual coupling, it is more difficult to design a modal coupling system than a destructive wave interference system. However, error sensors can be placed in the near field of the primary and secondary sources with this technique, leading to a compact ANC system.

To summarize, though destructive wave interference solutions are the easiest to implement, they result in only local control. Both mutual and modal coupling solutions are more difficult to design than their destructive wave interference counterparts, but can lead to global control of unwanted noise with a compact, practical system. This is why ANC of IT fan noise has concentrated primarily on mutual and modal coupling in order to achieve global control of the noise.

1.2 ANC of Axial Fans

Much of the previous work involving ANC on fan-induced IT noise has concentrated on axial cooling fans, such as those found in desktop computers and servers.[4-10] This previous approach was based on minimizing sound power in a computational model of fan radiation. This model included primary source(s) (which model the fan) and secondary source(s) (which model loudspeakers placed close to the fan) that were then placed in an infinite baffle. The radiated power was minimized by coupling the secondary sources with the primary sources, as described

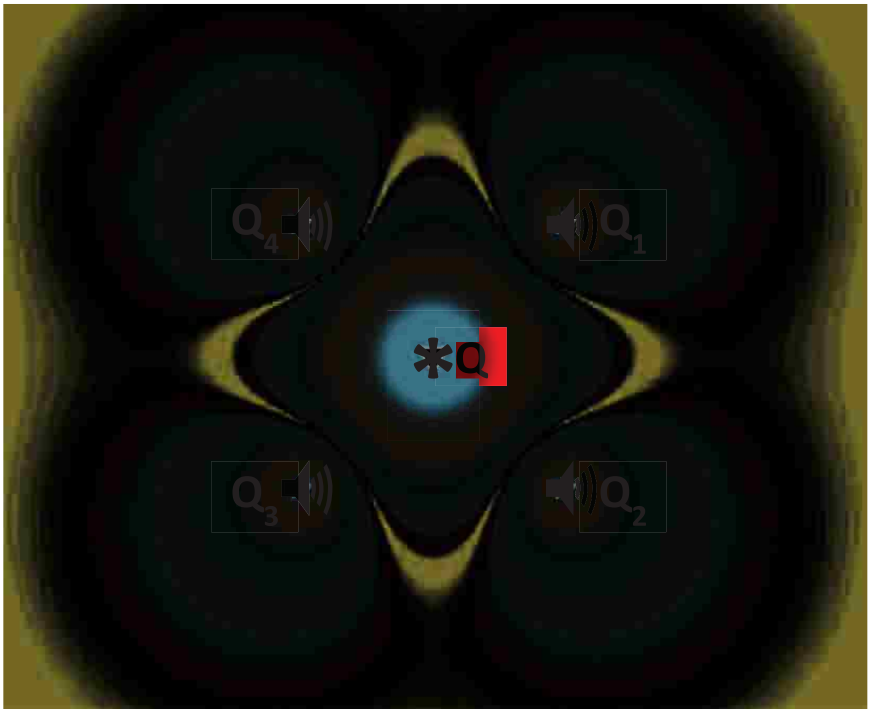

Figure 1-1 – Near-field pressure corresponding to the minimized power of the monopole model of axial fan radiation. The primary source is Q, while the secondary sources are Q_1 through Q_4. The magnitude of pressure in dB is proportional to the color scale, with red being high and blue being low.

in Sec. 1.1. This resulted in optimal secondary source strengths which could then be used to calculate the resulting pressure field in the near-field of the fan and secondary sources. Figure 1-1 shows the near-field pressure that results from this power minimization as given in Gee *et al*.[4-6] When the power is minimized, one or more near-field nodal lines develop. These nodal lines correspond to the predicted optimum location(s) for near-field error sensor(s), as shown in Fig. 1-1.[10]

Gee *et al*. then attempted to recreate this analytical result experimentally.[4-6] To do this, they took an axial cooling fan and surrounded it with four loudspeakers in a configuration mimicking Fig. 1-1. They then placed error sensors along the near-field nodal line predicted by the power minimization model. This experimental setup is shown in Fig. 1-2.[4-6]

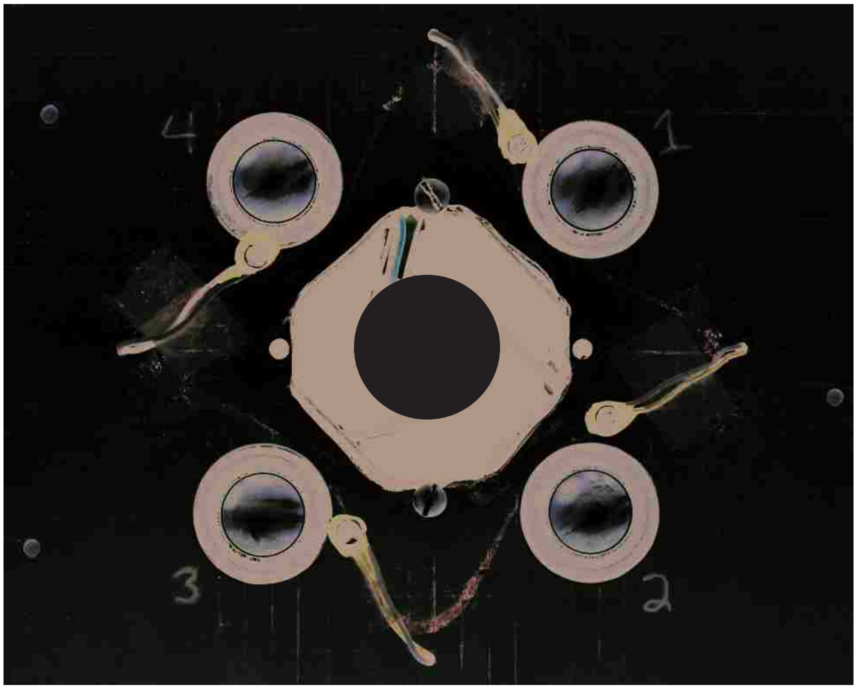

Figure 1-2 – Experimental setup mimicking the prediction shown in Fig. 1-1. The primary source (axial fan) is in the center and the secondary sources (loudspeakers) are shown surrounding the primary source. The green line duplicates the near-field nodal line shown in Fig. 1-1. One can see four error sensors that were placed on this nodal line.

There were several assumptions that went into the model that Gee *et al*. constructed, such as monopole-like primary and secondary sources and the presence of an infinite baffle, none of which are realizable.[4-6] However, running the experiment resulted in significant global sound power reduction. Figure 1-3 shows a typical result of these experiments, where the black mesh represents the uncontrolled sound field and the colored surface represents the controlled sound field. (For both controlled and uncontrolled results, radius of the surface is proportional to sound pressure level.) One can see that the controlled sound field is significantly lower in amplitude than the uncontrolled field in every direction. In addition, when both fields are summed across the entire hemisphere, there is a reduction in the global radiated sound power on the order of 15 dB.[4-6]

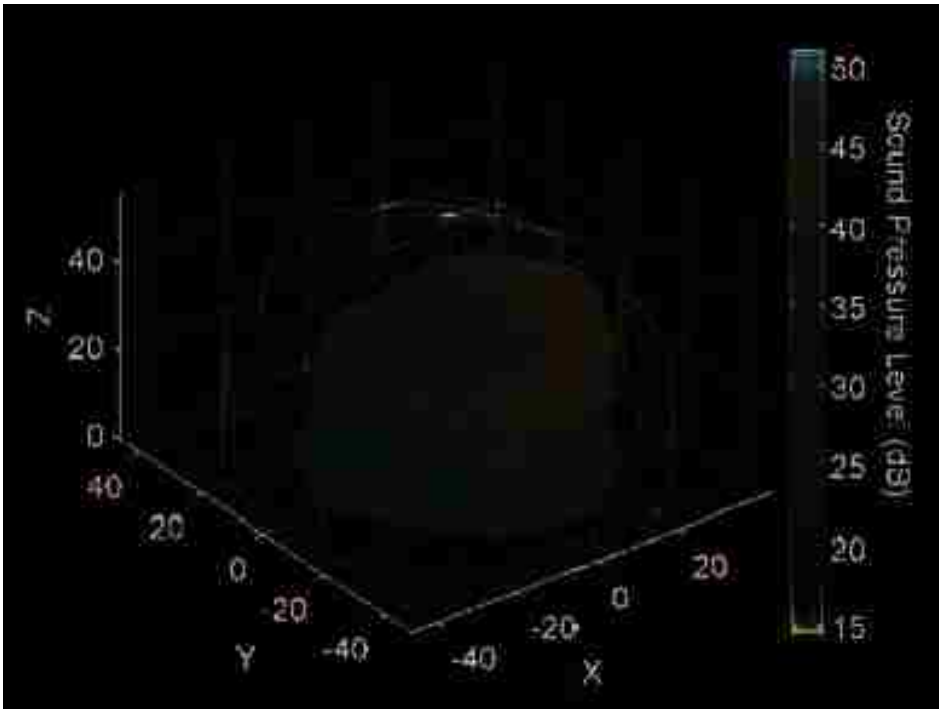

Figure 1-3 – Experimental results for axial fan ANC as given by Gee *et al.*[4–6] The black mesh represents the uncontrolled sound field while the colored surface represents the controlled sound field. The axes and color scale units are dB re 20 μPa.

1.3 ANC of Centrifugal Fans

Recently, there has been interest in using ANC to control the noise emitted from centrifugal fans used in IT equipment. Centrifugal fans are built such that their exhaust flow direction is perpendicular to their inlet flow direction. This contrasts with axial fans, whose exhaust and inlet flow directions are parallel.

Though there are variations in centrifugal fans, all have the same basic design as shown in Fig. 1-4.[11] Air enters the fan parallel to the axis of rotation and is forced outwards by the fan's blades (or impeller). The air then travels along the casing and is pushed out the exhaust outlet. The outlet flow is separated from the inlet flow by the cutwater. An example of a centrifugal fan is pictured in Fig. 1-5.

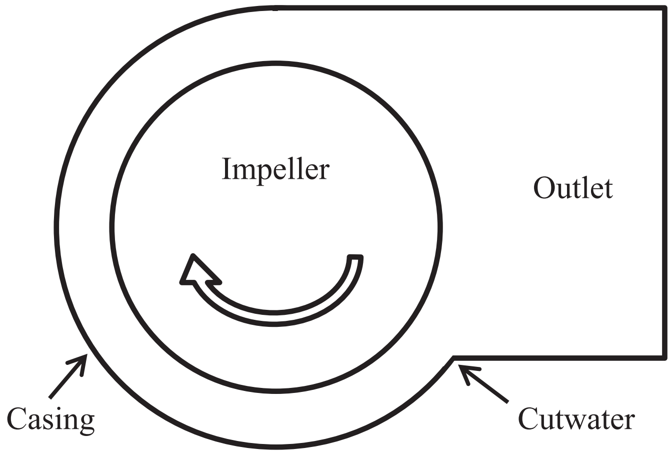

Figure 1-4 – Schematic for typical centrifugal fan, based on Embleton.[11]

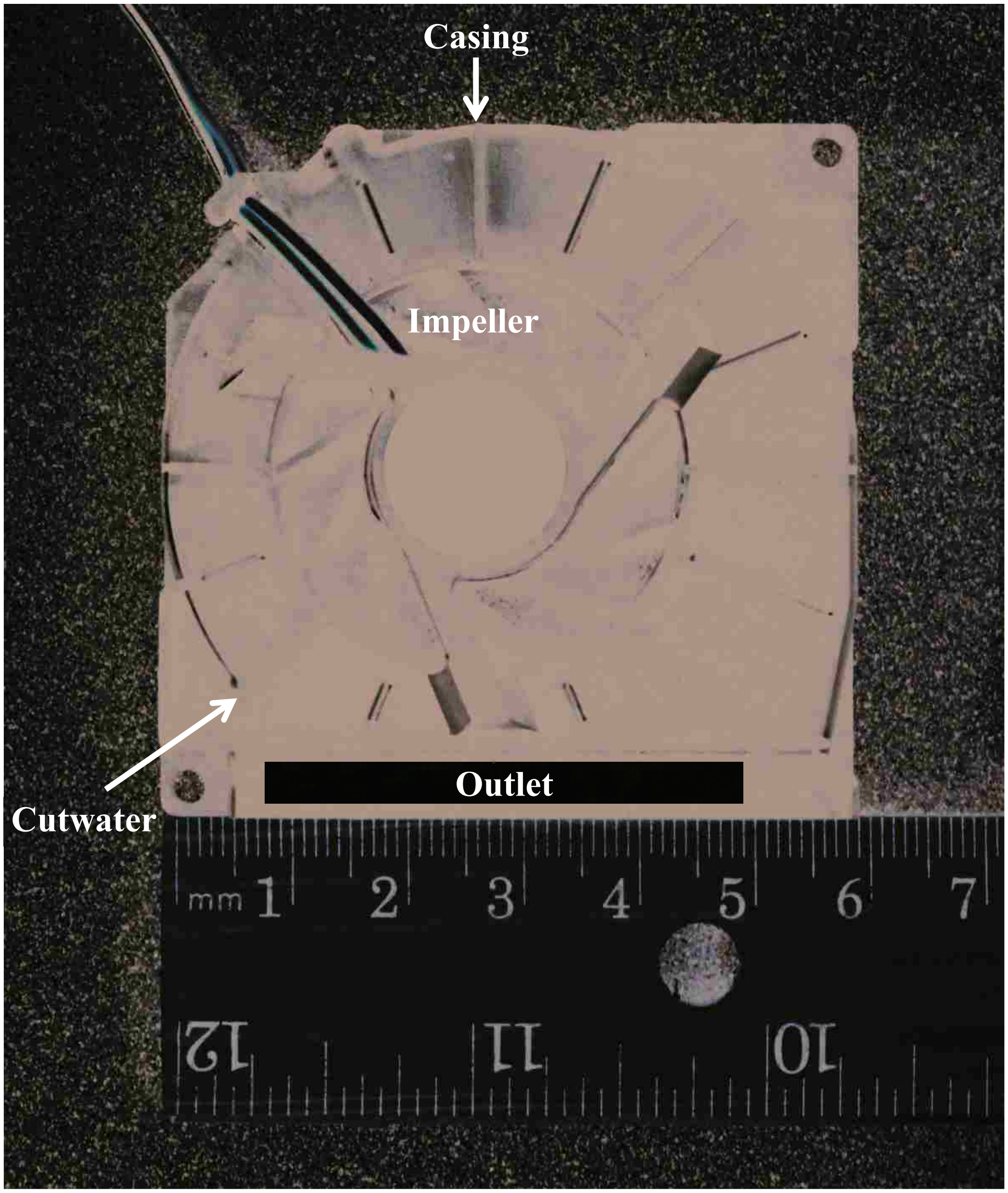

Figure 1-5 – Photograph of the centrifugal fan used in this study. Airflow is directed into the fan perpendicular to the page and is pushed by its impeller through its outlet. Relevant parts are indicated according to Fig. 1-4. The ruler is included for scale.

There are two types of noise that radiate from a centrifugal fan—broadband and tonal. Broadband noise originates from the turbulent structures formed by the fan's flow. Tonal noise radiates from an effective source located at the cutwater if the clearance between the impeller and the cutwater is small.[11,12] A sample spectrum of the noise from the centrifugal fan is shown in Fig. 1-6. Note the broadband noise floor caused by turbulent structure. Additionally, there are two sets of harmonic tones. The first set occurs at integer multiples of the fan's speed in revolutions per second (rps). These tones are generated by the fan's motor. The second set occurs at integer multiples of the blade passage frequency (bpf), given by

$$\text{bpf} = (\#\ \text{impeller blades}) \times \text{rps}. \tag{1-1}$$

These tones are generated as the impeller blades pass the cutwater which creates an oscillatory pressure.

Previous research applying ANC to centrifugal fans has concentrated on large centrifugal fans, such as those used in HVAC systems.[13-18] However, little research has applied ANC to

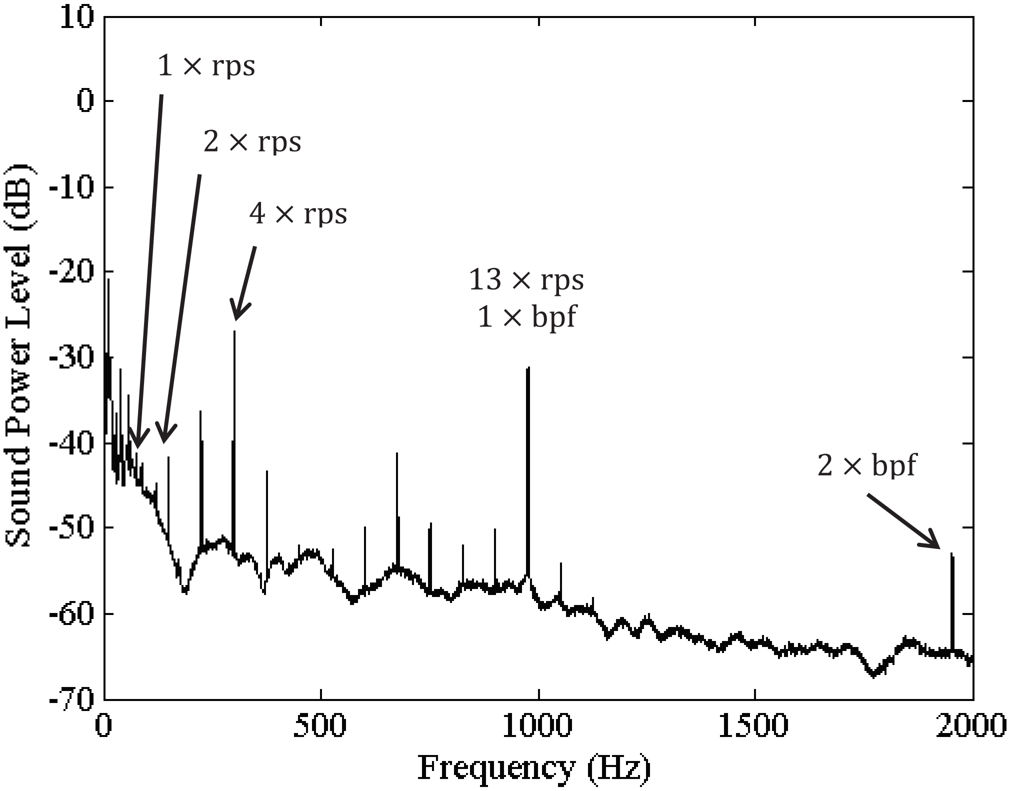

Figure 1-6 – Typical noise spectrum for the centrifugal fan tested. The motor speed for this spectrum is approximately 75 Hz, while bpf is at approximately 980 Hz.

small centrifugal fans, such as those used in laptops,[19,20] and none has used the power minimization techniques that have been applied to axial fans as described in Sec. 1-2

1.4 Overview

The purpose of this research is to modify the model used with axial fan ANC in order to develop an approach to implement ANC on the bpf (located nominally at 1 kHz) of a small, ducted centrifugal fan mounted in a mock laptop (notebook) enclosure. This model will predict tonal noise coming from both the inlets and the exhaust of the centrifugal fan and will estimate the sound power radiated to the far-field. From these results, both the secondary source strengths needed to minimize the radiated sound power and the near-field error sensor location(s) will be determined, akin to the axial fan case explained in Sec. 1.2. This work will implement an experimental ANC setup on the ducted centrifugal fan mounted in the mock laptop case using the developed models as a guide. The reduction in radiated sound power will be measured and compared to predicted values.

Chapter 2 illustrates the model developed for the exhaust of the centrifugal fan, while Chapter 3 explains the model developed for the inlets of the centrifugal fan. Chapter 4 considers the combined full-laptop model, while Chapter 5 contains the final conclusions of this research.

Chapter 2

ANC of Fan Exhaust Noise

Section 1.4 stated that there are two different propagation paths for the fan's noise. The first is through the fan's exhaust, while the second is through the fan's inlets. Each of these propagation paths requires a different analytical model because each of these paths is dissimilar to the other. This chapter develops the model used to predict and guide control of the noise propagating through the fan's exhaust.

2.1 Sound Field for a Point Source in a Duct

Based on the conclusions drawn in Sec. 1.3, the sound field of the fan's exhaust is approximated as a point source located inside a finite-length duct. The duct in which the point source is placed has dimensions $L_x \times L_y \times L_z$ and has rigid boundaries in the x and y dimensions. The point source has a source strength Q and is located at the point (x_0, y_0, z_0). It has a rigid boundary condition at $z = 0$ and a finite, non-zero radiation impedance boundary condition at $z = L_z$. This is shown in Fig. 2-1 in a cross-sectional view and in Fig. 2-2 in an isometric view. The radiation impedance boundary condition Z_{rad} is first assumed to be constant for all cross modes. This assumption is relaxed in Sec. 2-2 and 2-3.

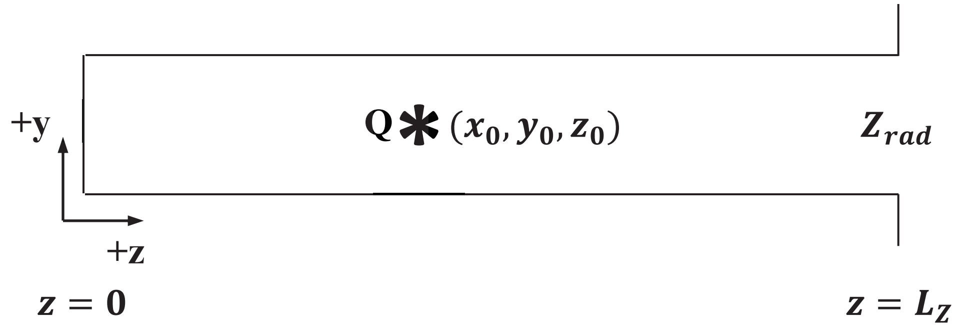

Figure 2-1 – Schematic of the idealized model setup. A point source is placed in a finite duct of length L_z at the location (x_0, y_0, z_0). The sides of the duct and the boundary at $z = 0$ are assumed rigid, but the end of the duct $(z = L_z)$ has a finite, non-zero radiation impedance boundary condition Z_{rad}.

When time-harmonic excitation is assumed, the equation for the pressure inside the duct is given by

$$\nabla^2 p + k^2 p = -j\rho_0 ckQ\, \delta(x - x_0)\, \delta(y - y_0)\, \delta(z - z_0), \tag{2-1}$$

where p is the complex pressure in the duct, k is the wavenumber given as ω/c, ω is the angular frequency, c is the acoustic phase speed, and ρ_0 is the density of the medium. $Q, x_0, y_0,$ and z_0 are as defined previously.

Equation (2-1) is solved through the use of Green's functions. The Green's function satisfies the equation

$$\nabla^2 G(r|r_0) + k^2 G(r|r_0) = -\delta(x - x_0)\, \delta(y - y_0)\, \delta(z - z_0), \tag{2-2}$$

where $G(r|r_0)$ is the Green's function for the duct, dependent on the source point $r_0 = (x_0, y_0, z_0)$ and the field point $r = (x, y, z)$. When the Green's function, $G(r|r_0)$, is expressed in terms of a modal expansion, it can be represented as

$$G(r|r_0) = \sum_{N=0}^{\infty} A_N \Psi_N(x, y, z), \tag{2-3}$$

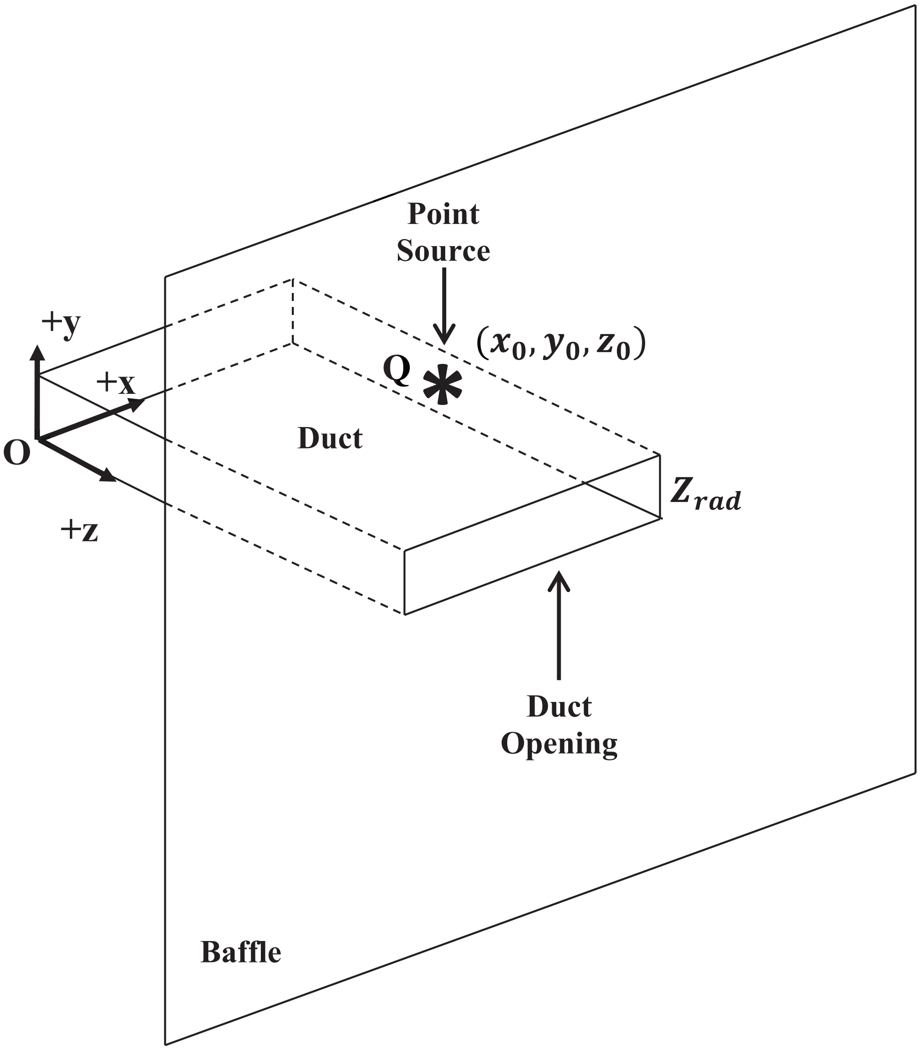

Figure 2-2 – Isometric view of the ideal system the model attempts to simulate. The primary source that models the fan is located at (x_0, y_0, z_0) with a source strength Q.

where r_0 is the location (x_0, y_0, z_0) of the point source, A_N is the coefficient for the N^{th} mode, $\Psi_N(x, y, z)$ is the eigenfunction that satisfies the boundary conditions in the $x, y,$ and z dimensions, and N is the overall modal index.

Because there are similar boundary conditions in x and y but different conditions in z, the eigenfunction is broken into two terms

$$\Psi_N(x, y, z) = \psi_N(x, y)\, F_N(z), \tag{2-4}$$

where $\psi_N(x, y)$ depends only on x and y while $F_N(z)$ depends only on z. If the boundaries in x and y are assumed to be rigid, $\psi_N(x, y)$ is merely a product of two cosine functions given by

$$\psi_N(x, y) = \cos\left(\frac{m_x\pi}{L_x}x\right)\cos\left(\frac{m_y\pi}{L_y}y\right), \tag{2-5}$$

where m_x and m_y are integers.

If Eqs. (2-3) and (2-4) are substituted into Eq. (2-2), this leads to

$$\begin{aligned}\sum_{N=0}^{\infty} A_N\big(\nabla^2[\psi_N(x, y)\, F_N(z)] + k^2\psi_N(x, y)\, F_N(z)\big)\\ = -\delta(x - x_0)\,\delta(y - y_0)\,\delta(z - z_0).\end{aligned} \tag{2-6}$$

Due to the fact that the boundaries in the x and y directions are rigid, the cross-section eigenfunctions satisfy the Helmholtz equation, given by

$$\Delta^2\psi_N(x, y) + k_N^2\psi_N(x, y) = 0, \tag{2-7}$$

where Δ^2 is the two-dimensional Laplacian and k_N is the wavenumber corresponding to the N^{th} mode. They also satisfy the orthogonality relation

$$\frac{1}{S}\iint_S \psi_N^2(x, y)dS = \Lambda_N, \tag{2-8}$$

where S is the cross-sectional area and Λ_N are the mean values of ψ_N^2 averaged over the cross-section.

The derivatives in Eq. (2-6) are then expanded to obtain

$$\sum_{N=0}^{\infty} A_N\left[\frac{d^2F_N(z)}{dz^2}\psi_N(x, y) + F_N(z)\Delta^2\psi_N(x, y) + k^2\psi_N(x, y)\, F_N(z)\right] = -\delta(r - r_0). \tag{2-9}$$

Equation (2-7) is then inserted into Eq. (2-9) to find that

$$\sum_{N=0}^{\infty} A_N \left[\frac{d^2F_N(z)}{dz^2}\psi_N(x,y) + F_N(z)(k^2 - k_N^2)\psi_N(x,y)\right] = -\delta(r - r_0), \tag{2-10}$$

where $r = (x, y, z)$ and $r_0 = (x_0, y_0, z_0)$.

Next, Equation (2-10) is multiplied by $\psi_M(x, y)$, integrated over S (the cross-sectional area), and orthogonality is applied to find that

$$\sum_{N=0}^{\infty} A_N \iint_S \left(\frac{d^2F_N(z)}{dz^2}\psi_N(x,y)\psi_M(x,y) + F_N(z)(k^2 - k_N^2)\psi_N(x,y)\psi_M(x,y)\right) dS$$

$$= -\iint_S \psi_M(x,y)\delta(x - x_0)\,\delta(y - y_0)\,\delta(z - z_0)dS \Longrightarrow$$

$$A_N \left[\frac{d^2F_N(z)}{dz^2}S\Lambda_N + F_N(z)(k^2 - k_N^2)S\Lambda_N\right] = -\psi_N(x_0, y_0)\delta(z - z_0) \Longrightarrow$$

$$A_N\left(\frac{d^2}{dz^2} + k_z^2\right)F_N(z) = -\frac{1}{S\Lambda_N}\psi_N(x_0, y_0)\delta(z - z_0), \tag{2-11}$$

where $k_z = \sqrt{k^2 - k_N^2}$.

The eigenfunction in the z direction has now been expressed in terms of the cross-sectional eigenfunction. Boundary conditions must now be applied to solve for $F_N(z)$, shown in Eq. (2-4). This can be done by separating $F_N(z)$ into two sections,

$$F_N(z) = \begin{cases} F_{N1}(z) = A_{N1}e^{-jk_z(z-z_0)} + B_{N1}e^{jk_z(z-z_0)}, & z < z_0 \\ F_{N2}(z) = A_{N2}e^{-jk_z(z-z_0)} + B_{N2}e^{jk_z(z-z_0)}, & z > z_0 \end{cases}, \tag{2-12}$$

where $A_{N1}, B_{N1}, A_{N2},$ and B_{N2} are modal-dependent constants. These take the place of A_N, found in Eq. (2-11). Note that each individual solution is made up of two traveling waves—one which propagates in the $+z$ direction and one which propagates in the $-z$ direction.

There are four boundary conditions to satisfy. These are

$$F_{N1}(0) = 0, \tag{2-13a}$$

$$\left.\frac{F_{N2}(z)}{-\frac{1}{j\omega\rho_0}\frac{dF_{N2}(z)}{dz}}\right|_{z=L_z} = Z_{rad}, \tag{2-13b}$$

$$F_{N1}(z_0) = F_{N2}(z_0), \tag{2-13c}$$

and

$$\left.\frac{dF_N(z)}{dz}\right|_{z=z_0-\alpha}^{z=z_0+\alpha} + 2k_z^2\alpha F_N(z_0) = -\frac{\psi_N(x_0, y_0)}{S\Lambda_N}. \tag{2-13d}$$

Equations (2-13a) and (2-13b) satisfy the boundary conditions at $z = 0$ and $z = L_z$, while Eqs. (2-13c) and (2-13d) satisfy the pressure continuity and velocity discontinuity boundary conditions at $z = z_0$ required by the Green's function.

After evaluating each of these boundary conditions, the constants A_{N1}, B_{N1}, A_{N2}, and B_{N2} are solved. When this is done, it can be shown that

$$\begin{aligned} A_{N1} = &-\frac{\psi_N(x_0, y_0)}{D_N S\Lambda_N}\frac{e^{-jk_zL_z}}{(k_zZ_{rad} + \rho_0 ck)\cos(k_zz_0)} \\ &\times (k_zZ_{rad}\cos[k_z(L_z - z_0)] + j\rho_0 ck\sin[k_z(L_z - z_0)]), \end{aligned} \tag{2-14a}$$

$$\begin{aligned} B_{N1} = &-\frac{\psi_N(x_0, y_0)}{D_N S\Lambda_N}\frac{e^{-jk_z(L_z-2z_0)}}{(k_zZ_{rad} + \rho_0 ck)\cos(k_zz_0)} \\ &\times (k_zZ_{rad}\cos[k_z(L_z - z_0)] + j\rho_0 ck\sin[k_z(L_z - z_0)]), \end{aligned} \tag{2-14b}$$

$$A_{N2} = -\frac{\psi_N(x_0, y_0)}{D_N S\Lambda_N}, \tag{2-14c}$$

and

$$B_{N2} = -\frac{\psi_N(x_0, y_0)}{D_N S\Lambda_N}\frac{k_zZ_{rad} - \rho_0 ck}{k_zZ_{rad} + \rho_0 ck}e^{-2jk_z(L_z-z_0)}, \tag{2-14d}$$

where

$$D_N = \frac{2k_z e^{-jk_z(L_z - z_0)}}{k_z Z_{rad} + \rho_0 ck} \\ \times [k_z Z_{rad}(\sin[k_z(L_z - z_0)] + \tan(k_z z_0)\cos[k_z(L_z - z_0)]) \\ - j\rho_0 ck(\cos[k_z(L_z - z_0)] - \tan(k_z z_0)\sin[k_z(L_z - z_0)])]. \tag{2-14e}$$

The Green's function can now be solved for in terms of Eqs. (2-3), (2-4), (2-5), (2-12), and (2-14). This leads to

$$G(r|r_0) \\ = \begin{cases} \sum_{m_x,m_y=0}^{\infty} \cos\left(\frac{m_x\pi}{L_x}x\right)\cos\left(\frac{m_y\pi}{L_y}y\right)\left(A_{N1}e^{-jk_z(z-z_0)} + B_{N1}e^{jk_z(z-z_0)}\right), z < z_0 \\ \sum_{m_x,m_y=0}^{\infty} \cos\left(\frac{m_x\pi}{L_x}x\right)\cos\left(\frac{m_y\pi}{L_y}y\right)\left(A_{N2}e^{-jk_z(z-z_0)} + B_{N2}e^{jk_z(z-z_0)}\right), z > z_0 \end{cases}, \tag{2-15}$$

where A_{N1}, B_{N1}, A_{N2}, and B_{N2} are as defined in Eq. (2-14).

With that, the pressure field inside the duct is given by

$$p = j\rho_0 ckQG(r|r_0), \tag{2-16}$$

as seen from Eqs. (2-1) and (2-2).

2.2 Multimodal Radiation Impedance

Equations (2-15) and (2-16) were developed under the assumption that the radiation impedance was constant for all cross modes. This assumption is now relaxed by stating the radiation impedance should be different for every cross mode. This gives rise to what Kemp *et al*. called a multimodal radiation impedance, or a modally-dependent radiation impedance.[21]

Kemp *et al.* found that the multimodal radiation impedance for a rigid rectangular duct set in an infinite baffle (as shown in Fig. 2-3) is

$$
\begin{aligned}
Z_{m,n} = \frac{j\rho_0 c}{2\pi}\Bigg(& \int_0^{kL_x}\int_0^{kL_y} \frac{\left(1-\frac{u}{2kL_x}\right)\left(1-\frac{v}{2kL_y}\right)}{\sqrt{u^2+v^2}} \\
& \times\left[e^{-j\sqrt{u^2+v^2}}\frac{G(m_x,n_x,u)}{1-\frac{u}{2kL_x}}\frac{G(m_y,n_y,v)}{1-\frac{v}{2kL_y}}-f(m,n)\right]\mathrm{d}u\,\mathrm{d}v \\
& + f(m,n)\left[\int_0^{kL_x}\left(1-\frac{u}{2kL_x}\right)\left[\ln\left(kL_y+\sqrt{u^2+\left(kL_y\right)^2}\right)+\frac{u}{2kL_y}\right.\right. \\
& \left.\left.-\frac{1}{2kL_y}\sqrt{u^2+\left(kL_y\right)^2}\right]\mathrm{d}u-\frac{3}{4}kL_x\ln(kL_x)+\frac{7}{8}kL_x\right]\Bigg),
\end{aligned}
\qquad \textbf{(2-17)}
$$

where $Z_{m,n}$ is the radiation impedance for the m^{th} pressure mode and the n^{th} particle velocity mode (*i.e.* the radiation impedance that couples the pressure associated with the m^{th} mode to the particle velocity associated with the n^{th} mode), u and v are integration variables, m_x and m_y are the pressure modal indices, n_x and n_y are the particle velocity modal indices,

$$
\begin{aligned}
G(m_x, n_x, u) = N_{m_x} N_{n_x} \{ & \cos\left((m_x - n_x)\pi \frac{u}{2kL_x}\right) \\
& \times \frac{1}{2}\left[\left(2 - \frac{u}{kL_x}\right)\operatorname{sinc}\left((m_x + n_x)\pi\left(1 - \frac{u}{2kL_x}\right)\right)\right. \\
& \left. - \frac{u}{kL_x}\operatorname{sinc}\left((m_x + n_x)\pi \frac{u}{2kL_x}\right)\right] + \cos\left((m_x + n_x)\pi \frac{u}{2kL_x}\right) \\
& \times \frac{1}{2}\left[\left(2 - \frac{u}{kL_x}\right)\operatorname{sinc}\left((m_x - n_x)\pi\left(1 - \frac{u}{2kL_x}\right)\right)\right. \\
& \left. - \frac{u}{kL_x}\operatorname{sinc}\left((m_x - n_x)\pi \frac{u}{2kL_x}\right)\right],
\end{aligned}
\qquad \textbf{(2-18)}
$$

$$
\begin{aligned}
f(m, n) = N_{m_x} N_{n_x} N_{m_y} N_{n_y} & \times \left[\operatorname{sinc}\big((m_x + n_x)\pi\big) + \operatorname{sinc}\big((m_x - n_x)\pi\big)\right] \\
& \times \left[\operatorname{sinc}\left((m_y + n_y)\pi\right) + \operatorname{sinc}\left((m_y - n_y)\pi\right)\right],
\end{aligned}
\qquad \textbf{(2-19)}
$$

$$
\operatorname{sinc}(x) = \frac{\sin(x)}{x}, \qquad \textbf{(2-20)}
$$

and

$$
N_n = \begin{cases} 1, & n = 0 \\ \sqrt{2}, & n > 0 \end{cases}. \qquad \textbf{(2-21)}
$$

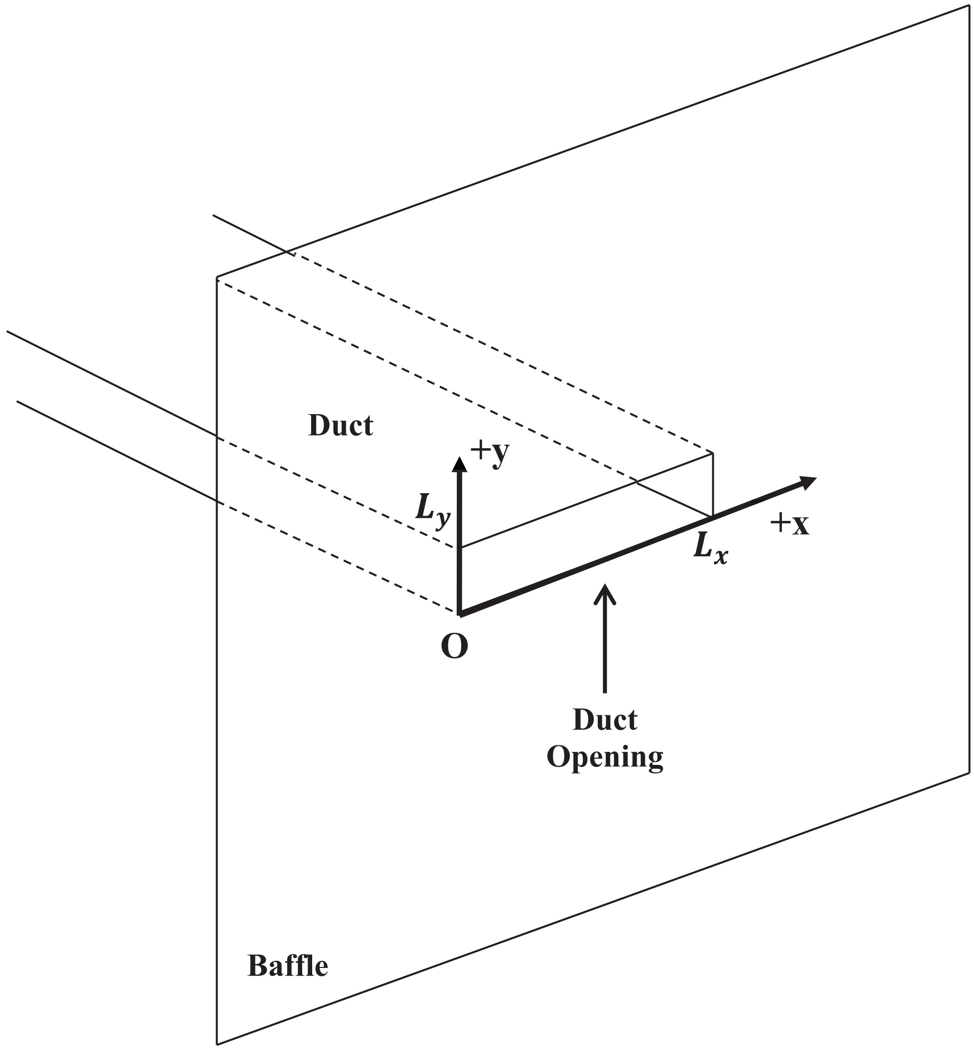

Figure 2-3 – Geometry of infinitely baffled rectangular duct, modeled after Kemp et al.[20]

Interested readers can find the derivation for the multimodal radiation impedance of a rigid duct set in an infinite baffle in Kemp *et al*.[21] Note that the plane-wave mode occurs when $m = 1$ (for pressure) or $n = 1$ (for particle velocity). The radiation impedance for a baffled rectangular piston occurs when both m and n equal 1.

When this formulation is applied to the fan's exhaust duct, a radiation impedance matrix is the result, shown graphically in Fig. 2-4. This matrix is the collection of results from Eq. (2-17) with different values for $m_x, n_x, m_y,$ and n_y. These are sorted in order of ascending

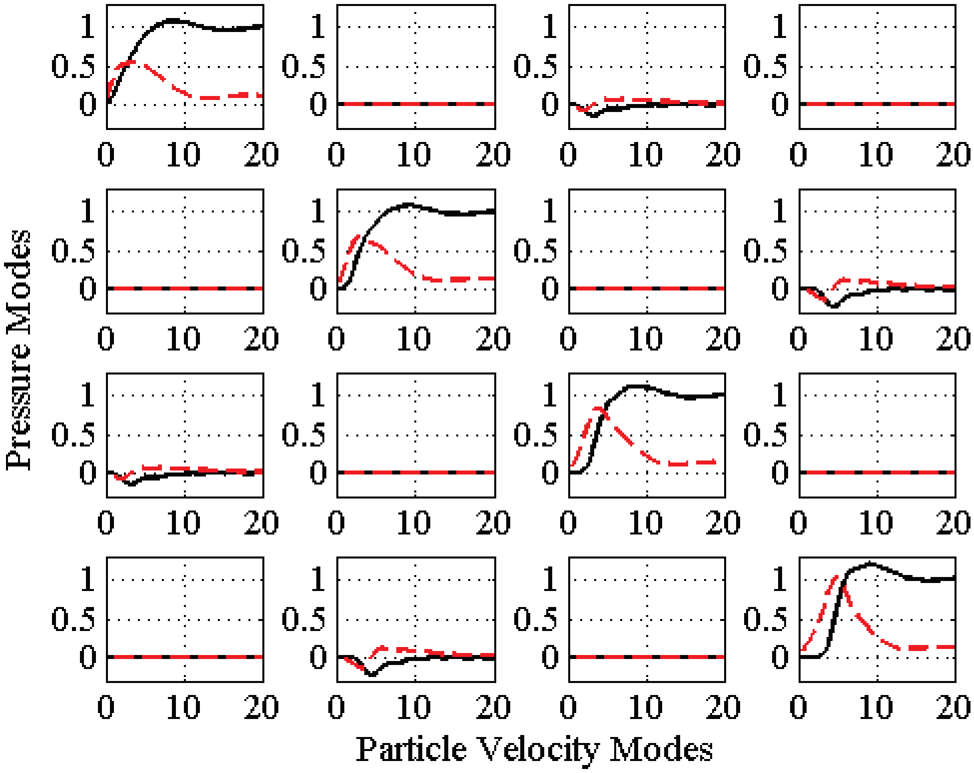

Figure 2-4 – Radiation impedance for the rectangular duct for the first four pressure and velocity modes. The black solid curves are the radiation resistance (the real part of the radiation impedance), while the red dashed curves are the radiation reactance (the imaginary part of the radiation impedance). The row index is the pressure mode number m while the column index is the particle velocity mode number n (*e.g.* the [1,3] entry is the radiation impedance due to coupling the pressure from the first mode with the particle velocity from the third mode). The x-axes units for each entry are the dimensionless quantity $k\sqrt{S}$, where k is the wavenumber and S is the cross-sectional area of the duct. The y-axes units for each entry are normalized impedance magnitude.

frequency and displayed in matrix form, with pressure modes incrementing with rows and particle velocity modes incrementing with columns. The black solid curves are the radiation resistance (the real part of the radiation impedance), while the red dashed curves are the radiation reactance (the imaginary part of the radiation impedance). For another example of radiation impedance matrices, see Ref. [22].

From Fig. 2-4 we draw a number of interesting conclusions. First, the dominant contributions to the radiation impedance are the result of like pressure modes coupling with like particle velocity modes. These form the main diagonal of the radiation impedance matrix. Second, there are small, but non-zero contributions to the total radiation impedance when an odd pressure mode couples with an odd particle velocity mode or when an even pressure mode couples with an even particle velocity mode. This occurs at alternating entries throughout the matrix. In both these cases, both the resistive and reactive parts of the radiation impedance couple. Third, there is no noticeable contribution to the total radiation impedance when odd pressure modes couple with even particle velocity modes or when even pressure modes couple with odd particle velocity modes. These entries form the remainder of the radiation impedance matrix. For more detailed analysis of the radiation impedance matrix, see Appendix A.

2.3 Pressure-Particle Velocity Modal Coupled Sound Field Solution

The results developed in Sec. 2.1 assumed that the radiation impedance was constant over all cross modes. This assumption was relaxed in Sec. 2.2 by developing a multimodal radiation impedance. Section 2.1 must now be modified to account for the multimodal radiation impedance developed in Sec. 2.2.

First, Eq. (2-12b) must be modified; instead of assuming a constant radiation impedance boundary condition, it is stated that

$$F_{N2}(L_z) = \sum_n Z_{m,n} \left(-\frac{1}{j\rho_0 ck} \frac{\partial F_{N2}(z)}{\partial z} \right) \Bigg|_{z=L_z}, \tag{2-22}$$

where the multimodal radiation impedance $Z_{m,n}$ replaces the constant radiation impedance Z_{rad} seen in Eq. (2-13b). Note that the sum on the right-hand side of the equation sums only over n, or the velocity modes. This is because the quantity inside the parentheses is equal to the velocity—thus the quantity is summed over all velocity modes to satisfy the equality.

If $F_{N2}(z)$ is expanded as shown in Eq. (2-12) and the notation of Kemp *et al.*is used, it can be shown that

$$\begin{aligned} &A_{N2,m}e^{-jk_{z,m}(L_z-z_0)} + B_{N2,m}e^{jk_{z,m}(L_z-z_0)} \\ &\qquad = -\frac{1}{j\rho_0 ck}\sum_n Z_{m,n}\big[-jk_{z,n}A_{N2,n}e^{-jk_{z,n}(L_z-z_0)} \\ &\qquad + jk_{z,n}B_{N2,n}e^{jk_{z,n}(L_z-z_0)}\big], \end{aligned} \tag{2-23}$$

where m is associated with pressure modes, while n is associated with velocity modes. Note that $k_{z,n}$ is associated with velocity modes, not pressure modes, unless $m = n$, (*i.e.* the pressure mode and velocity mode have the same modal index).

If the self-impedances ($m = n$, or the main diagonal terms of the radiation impedance matrix) are grouped on the left-hand side of Eq. (2-23) and the mutual impedances ($m \neq n$, or the off-diagonal terms of the radiation impedance matrix) are kept on the right hand of Eq. (2-23), this leads to

$$\begin{aligned} &A_{N2,m}\big(\rho_0 ck - k_{z,m}Z_{m,m}\big)e^{-jk_{z,m}(L_z-z_0)} + B_{N2,m}\big(\rho_0 ck + k_{z,m}Z_{m,m}\big)e^{jk_{z,m}(L_z-z_0)} \\ &\qquad = \sum_{n\neq m} k_{z,n}Z_{m,n}\big(A_{N2,n}e^{-jk_{z,n}(L_z-z_0)} - B_{N2,n}e^{jk_{z,n}(L_z-z_0)}\big). \end{aligned} \tag{2-24}$$

This can be set up as a matrix equation. Using Einstein notation, it can be shown that

$$\begin{aligned} &\big(\rho_0 ck\mathbf{I} - k_{z,n}Z_n^m e^{-jk_{z,n}(L_z-z_0)}\big)A_{N2,m} \\ &\qquad + \big(\rho_0 ck\mathbf{I} + k_{z,n}Z_n^m e^{jk_{z,n}(L_z-z_0)}\big)B_{N2,m} = 0 \Longrightarrow \end{aligned} \tag{2-25a}$$

$$\boldsymbol{R_1}\,\boldsymbol{A_{N2}} + \boldsymbol{S_1}\,\boldsymbol{B_{N2}} = \boldsymbol{0}, \tag{2-25b}$$

where m and n are the pressure and velocity modal indices as before, and $\boldsymbol{R_1}$ and $\boldsymbol{S_1}$ are the matrix quantities enclosed in parentheses in Eq. (2-25a).

When the other boundary conditions found in Eqs. (2-13a), (2-13c), and (2-13d) are applied, this leads to

$$\left(k_{z,n}\left[-j+\tan\left(k_{z,n}z_0\right)e^{jk_{z,n}(2z_0-L_z)}\right]\right)A_{N2,m} + \left(k_{z,n}\left[j+\tan\left(k_{z,n}z_0\right)e^{jk_{z,n}(2z_0-L_z)}\right]\right)B_{N2,m} = -\frac{1}{S}\frac{\psi_m(x_0,y_0)}{\Lambda_m} \Longrightarrow$$

$$\boldsymbol{R_2}\,\boldsymbol{A_{N2}} + \boldsymbol{S_2}\,\boldsymbol{B_{N2}} = -\frac{1}{S}\,\boldsymbol{V}, \tag{2-26a}$$

$$\boldsymbol{A_{N1}} = \frac{1}{2}\frac{e^{-jk_{z,m}(L_z-z_0)}}{\cos(k_z z_0)}(\boldsymbol{A_{N2}}+\boldsymbol{B_{N2}}), \tag{2-26b}$$

and

$$\boldsymbol{B_{N1}} = e^{2jk_{z,m}z_0}\boldsymbol{A_{N1}}\,, \tag{2-26c}$$

where $k_{z,m}$ is dependent on the pressure modes, not the velocity modes. Note that $\boldsymbol{A_{N1}}$ and $\boldsymbol{B_{N1}}$ are dependent only on pressure modes, not velocity modes. One expects this, as there is no pressure-particle velocity coupling on the $z=0$ side of the duct.

From here, the Green's function is computed as before in Eqs. (2-3), (2-4), (2-5), (2-12), (2-15). This leads to the final expression for the pressure for a point source located inside a finite-length rectangular duct, given by

$$p(x,y,z) = j\rho_0 ckQ$$

$$\times$$

$$\begin{cases} \sum_{m_x,m_y=0}^{\infty} \begin{matrix} \cos\left(\frac{m_x\pi}{L_x}x\right)\cos\left(\frac{m_y\pi}{L_y}y\right) \\ \times\left(\boldsymbol{A}_{N1_{m_x m_y}} e^{-jk_z(z-z_0)} + \boldsymbol{B}_{N1_{m_x m_y}} e^{jk_z(z-z_0)}\right) \end{matrix}, & z < z_0 \\ \sum_{m_x,m_y,n_x,n_y=0}^{\infty} \begin{matrix} \cos\left(\frac{m_x\pi}{L_x}x\right)\cos\left(\frac{m_y\pi}{L_y}y\right) \\ \times\left(A_{N2_{m_x,m_y,n_x,n_y}} e^{-jk_z(z-z_0)} + B_{N2_{m_x,m_y,n_x,n_y}} e^{jk_z(z-z_0)}\right), \end{matrix} & z > z_0 \end{cases}, \qquad \textbf{(2-27)}$$

where $\boldsymbol{A}_{N1}$, $\boldsymbol{B}_{N1}$, $\boldsymbol{A}_{N2}$, and $\boldsymbol{B}_{N2}$ are as defined in Eq. (2-26).

2.4 Minimization of Sound Power

The derivations up to this point have concentrated on finding the pressure field in a finite duct due to only one source. However, in order to minimize the radiated sound power from the duct (the focus of exhaust ANC), the model must include a secondary source.[23]

Figure 2-5 shows the ANC setup that the model simulates. A secondary source with control strength Q_1 is located at (x_1, y_1, z_1). The process detailed in Sec. 2.1-2.3 is applied to each source individually. Each separate solution is then superposed to find the total pressure, given by

$$p = j\rho_0 ck[QG(r|r_0) + Q_1 G(r|r_1)], \qquad \textbf{(2-28)}$$

where r_0 is the location of the primary source and r_1 is the location of the secondary source.

Now, the total power radiated from the duct is equal to

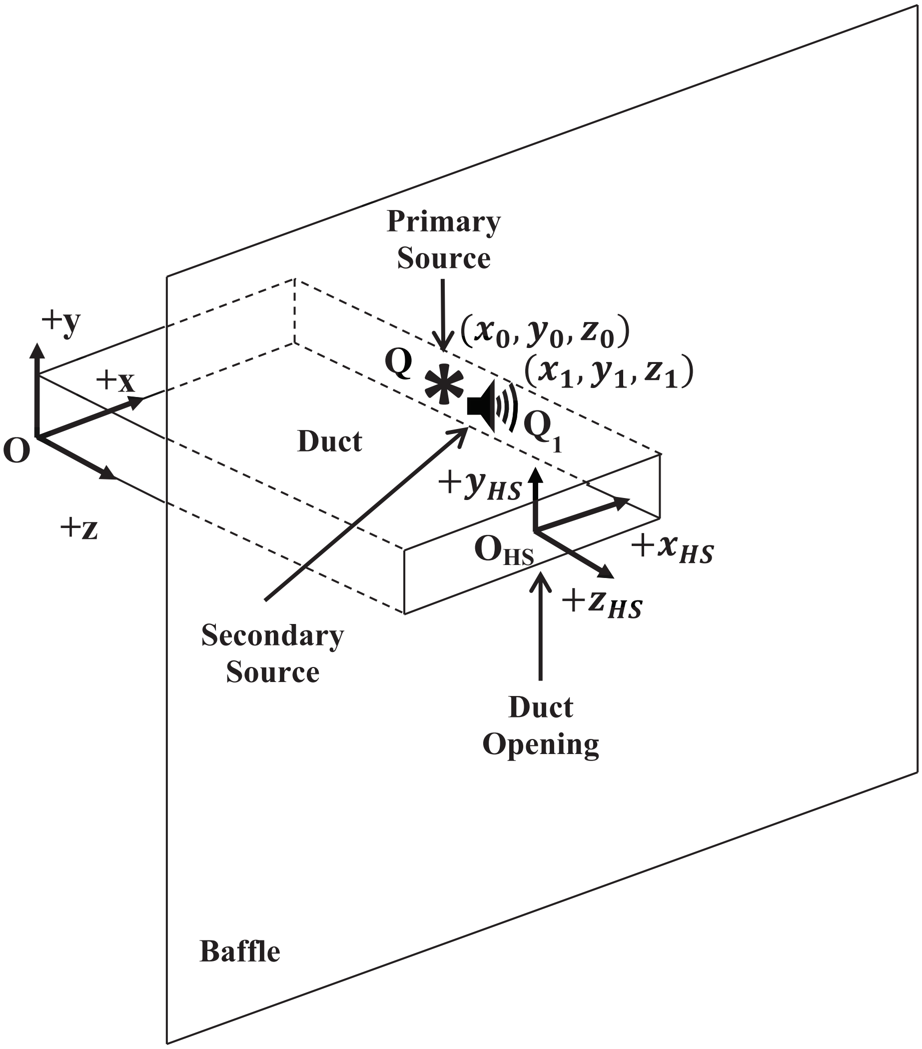

Figure 2-5 – Isometric view of the ideal system pictured in Fig. 2-2 with a secondary source placed at (x_1, y_1, z_1), which is close to the location of the primary source located at (x_0, y_0, z_0).

$$\Pi = \int_0^{L_x} \int_0^{L_y} \frac{1}{2} \Re\{p(x, y, L_z) u_z^*(x, y, L_z)\} \mathrm{d}y \, \mathrm{d}x, \tag{2-29}$$

where r is expanded into its Cartesian components, $\Re$ denotes the real part, $*$ denotes the complex conjugate, and both p and u are evaluated at $z = L_z$.

From Eq. (2-28) we can find the particle velocity in the z direction through Euler's relation. From this, it can be shown that

$$u_z = -\left[Q\frac{\partial G(r|r_0)}{\partial z} + Q_1\frac{\partial G(r|r_1)}{\partial z}\right]. \tag{2-30}$$

If Eqs. (2-28) and (2-30) are substituted into Eq. (2-29), this leads to

$$\Pi = \int_0^{L_x}\int_0^{L_y} \frac{1}{2}\Re\left\{(j\rho_0 ck[QG(r|r_0) + Q_1G(r|r_1)])\right.$$

$$\left.\left.\times\left(-\left[Q^*\frac{\partial G^*(r|r_0)}{\partial z} + Q_1^*\frac{\partial G^*(r|r_1)}{\partial z}\right]\right)\right\}\right|_{\mathrm{z=L_z}} \mathrm{d}y\,\mathrm{d}x \Rightarrow$$

$$\Pi = \frac{\rho_0 ck}{2}\int_0^{L_x}\int_0^{L_y} \Im\left\{|Q|^2G(r|r_0)\frac{\partial G^*(r|r_0)}{\partial z} + QG(r|r_0)Q_1^*\frac{\partial G^*(r|r_1)}{\partial z}\right.$$
$$\left. + Q_1G(r|r_1)Q^*\frac{\partial G^*(r|r_0)}{\partial z} + |Q_1|^2G(r|r_1)\frac{\partial G^*(r|r_1)}{\partial z}\right\}\mathrm{d}y\,\mathrm{d}x, \tag{2-31}$$

where $\Im$ denotes the imaginary part.

There is now an expression for the total power Π in terms of Q_1. In order to find the analytic expression for the minimum power in terms of Q_1, Q_1 is first separated into its real and imaginary parts, such that

$$\Pi = \frac{\rho_0 ck}{2}\Im\{A + BQ_{1,R} - jBQ_{1,I} + CQ_{1,R} + jCQ_{1,I} + D|Q_1|^2\}, \tag{2-32}$$

where A, B, C, and D are the quantities that multiply powers of Q_1 as shown in Eq. (2-31). Note that we incorporate the double integral into each term of the sum.

When the derivative of Π is taken with respect to both $Q_{1,R}$ and $Q_{1,I}$ it can be shown that

$$\frac{\partial\Pi}{\partial Q_{1,R}} = \frac{\rho_0 ck}{2}\Im\{B + C + 2DQ_{1,R}\} \text{ and} \tag{2-33a}$$

$$\frac{\partial\Pi}{\partial Q_{1,I}} = \frac{\rho_0 ck}{2}\Im\{-jB + jC + 2DQ_{1,I}\}. \tag{2-33b}$$

These quantities are set equal to zero in order to solve for $Q_{1,R}$ and $Q_{1,I}$. This leads to

$$Q_{1,R} = \frac{-\Im\{B\} - \Im\{C\}}{2\Im\{D\}} \text{ and} \tag{2-34a}$$

$$Q_{1,I} = \frac{\Re\{B\} - \Re\{C\}}{2\Im\{D\}}. \tag{2-34b}$$

It is known that $Q_1 = Q_{1,R} + jQ_{1,I}$, which leads to

$$Q_1 = \frac{-\Im\{B\} - \Im\{C\} + j(\Re\{B\} - \Re\{C\})}{2\Im\{D\}} = j\frac{B - C^*}{2\Im\{D\}}. \tag{2-35}$$

The secondary source strength that will minimize the sound power radiated from the duct is now known.

The pressure field generated immediately outside the duct outlet when this minimum power condition is met is now determined. This is done through Rayleigh's integral, given by

$$p_{HS}(r_{HS}) = \frac{j\rho_0 ck}{2\pi}\int_0^{L_x}\int_0^{L_y} u_z(x, y, L_z)\frac{e^{-jkR(x,y)}}{R(x,y)}\,\mathrm{d}y\,\mathrm{d}x, \tag{2-36}$$

where p_{HS} is the pressure radiated from the duct into the half-space, r_{HS} is the coordinate system in the half-space (as seen in Fig. 2-5, expanded into Cartesian coordinates), and R is the distance from the source point (x_{HS}, y_{HS}) to the field point r_{HS}.

If Eq. (2-35) is substituted into Eq. (2-30) and evaluated at $z = L_z$, it can be shown that

$$u_z(L_z) = -\left[Q\frac{\partial G(r|r_0)}{\partial z} + j\frac{B - C^*}{2\Im\{D\}}\frac{\partial G(r|r_1)}{\partial z}\right]\Bigg|_{z=L_z}. \tag{2-37}$$

From this result, all that remains is to substitute Eq. (2-37) into Eq. (2-36) to obtain the pressure field for all points in the half-space outside the duct. This produces a figure similar to Fig. 2-6. This figure shows the difference between the uncontrolled pressure radiated from the duct and the pressure radiated from the duct when the total sound power is minimized. The duct outlet is the rectangular box in the middle of the figure. Note that when the minimum power condition is met, a pressure nodal line results. This nodal line is the ideal location for an error sensor to be placed, as referred to in Sec. 1.2.

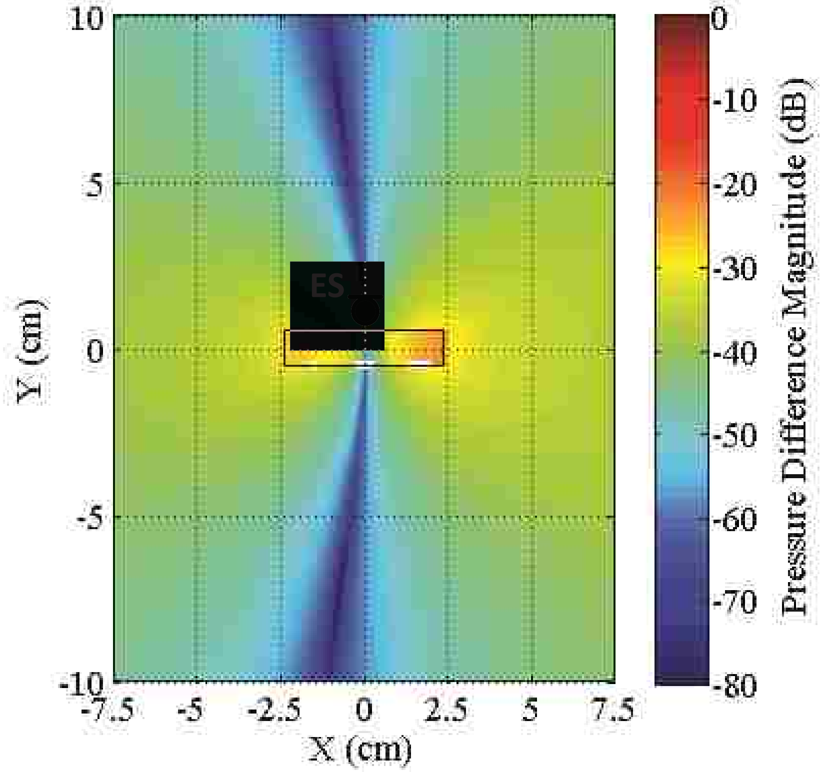

Figure 2-6 – Map of difference in pressure magnitude at 1 kHz that results when the radiation from the finite-length duct is minimized. The rectangle in the middle represents the opening of the duct. For experimental validation, an error sensor (ES) is placed along the nodal line as indicated. Axis units are in centimeters while the color scale is in dB relative to the uncontrolled field.

2.5 Experimental Validation

The final step in this process is to verify this model experimentally. We did this in two different stages. First, we constructed an ideal duct with the same dimensions as the centrifugal fan and its attached duct, shown in Fig. 2-8. This ideal duct has inside dimensions of 4.8 cm x 1 cm x 10 cm. We then inserted two Sonion 0935 loudspeakers inside the duct in close proximity to each other—one for the primary source and one for the secondary source. We mounted this duct assembly in a large baffle (7½ feet x 7½ feet) underneath a rotating semicircular arc. Attached to this arc are thirteen ½" GRAS ICP omnidirectional microphones, placed at 15° increments. The microphones are attached to the arc via metal rods, which place the microphones

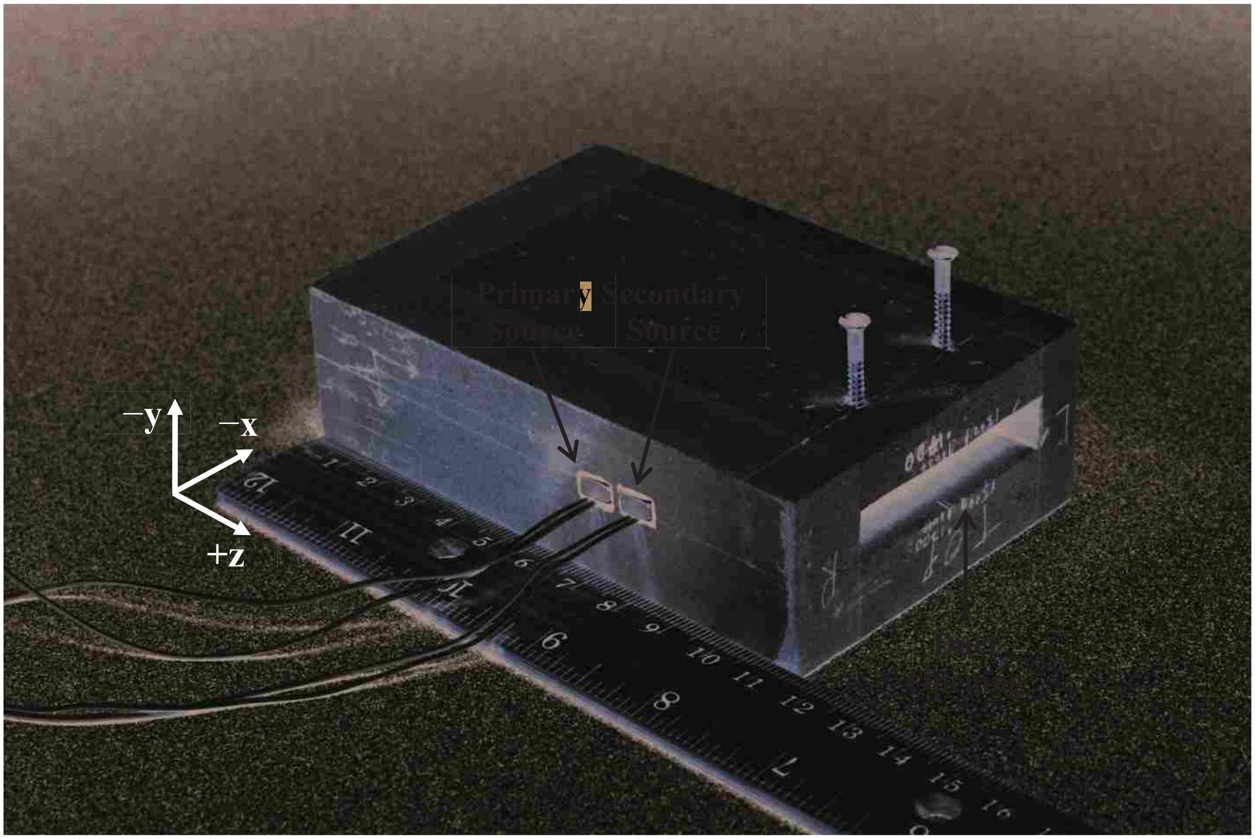

Figure 2-7 – Picture of the ideal duct used to validate the model. Note the primary source and secondary source on the left side of the duct. The ruler is included for scale.

56 cm from the center of the arc. We placed an error sensor (an 1/8” electret microphone) on the baffle in the ideal location predicted by the model, shown in Fig. 2-6. A picture of the microphone array, baffle, and duct is shown in Fig. 2-8, while a close-up of the duct is shown in Fig. 2-9. We then measured the sound power of the system with the aforementioned arc both with and without control. The difference between these two measurements should be close to the predicted reduction. (For details, see Ref. [24].)

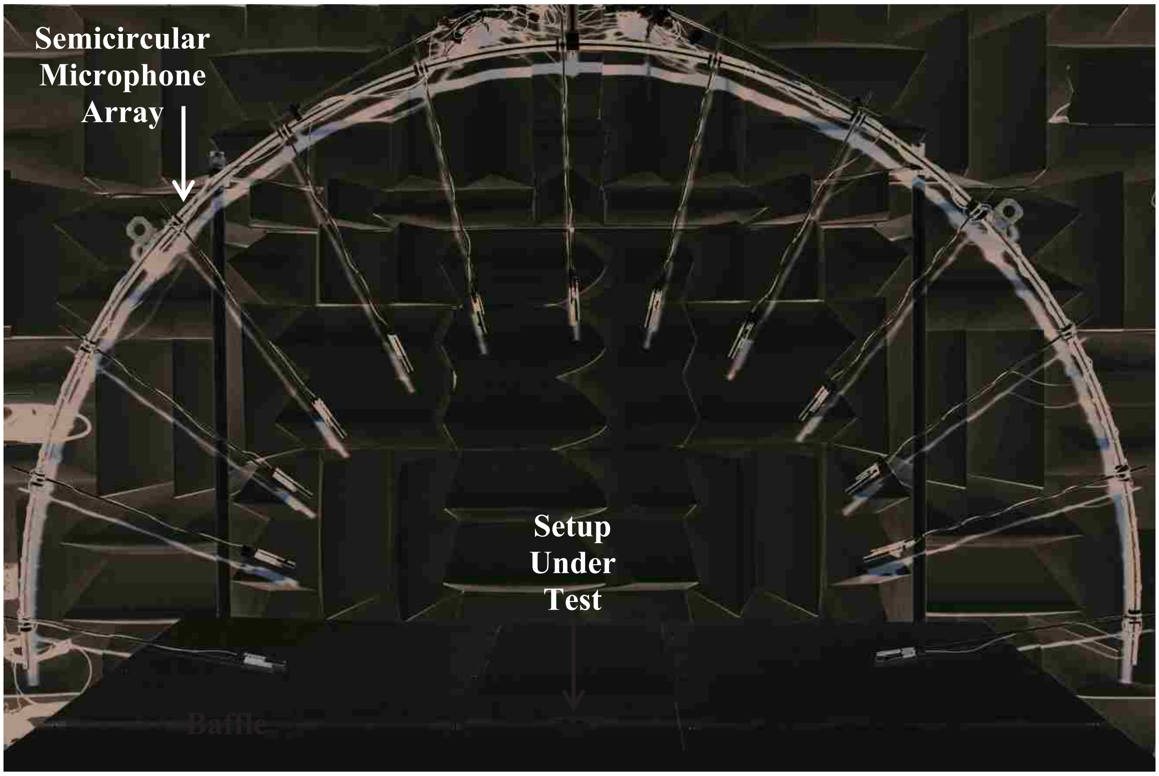

Figure 2-8 – Photograph showing the ideal duct mounted underneath a large baffle (7½ feet square) with a semicircular array of microphones (56 cm radius) suspended overhead.

Figure 2-9 – Photograph showing a close-up of the ideal duct (pictured in Fig. 2-7) mounted in the large baffle pictured in Fig. 2-8. The dots indicate error sensor positions for the frequency indicated.

Figure 2-10 shows the results of this first test. The predicted reduction is shown for frequencies between 500 Hz and 2000 Hz, while the measured reduction for this ideal duct is shown for frequencies between 1000 Hz and 1700 Hz in 100 Hz increments. The measured reductions match quite closely the predicted theoretical maximum up to approximately 1500 Hz, well above the maximum operating range of the fan.

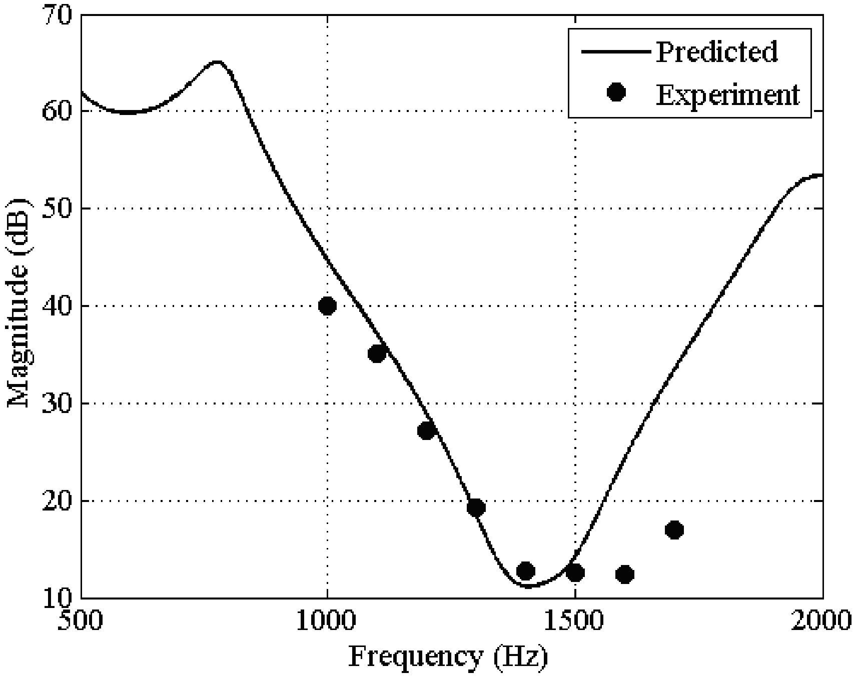

Figure 2-10 – Experimental results showing sound power reduction for the ideal duct pictured in Fig. 2-7. The line shows the theoretical prediction for attenuation, while the dots show experimental results at 100-Hz spacing between 1000 Hz and 1700 Hz. The x-axis is in hertz while the y-axis is in decibels.

The second experimental step is to replace the ideal duct with an actual fan and duct assembly, pictured in Fig. 2-11. This assembly is mounted in the baffle with the error sensor in the same location as before, pictured in Fig. 2-12. A Sonion 0935 loudspeaker was used as the secondary source.

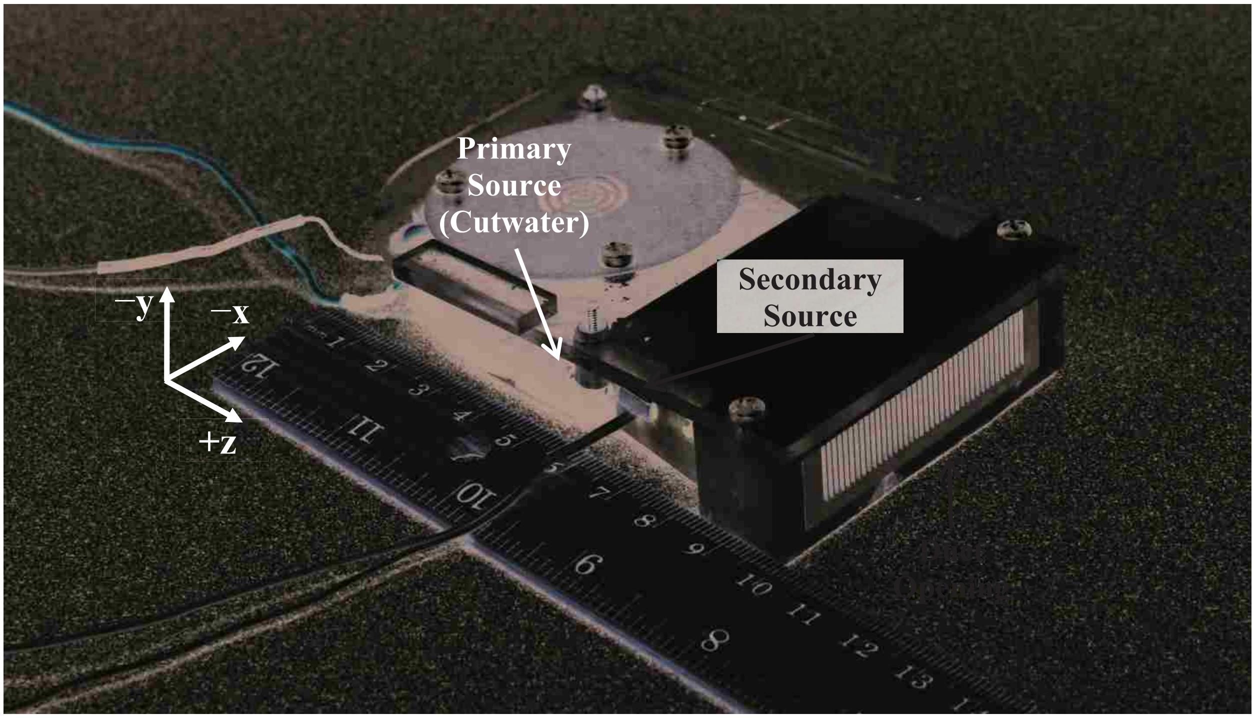

Figure 2-11 – Photograph of the fan and duct assembly used in the second stage of testing. Note the secondary source on its left side, located just downstream of the fan's cutwater. The ruler is included for scale.

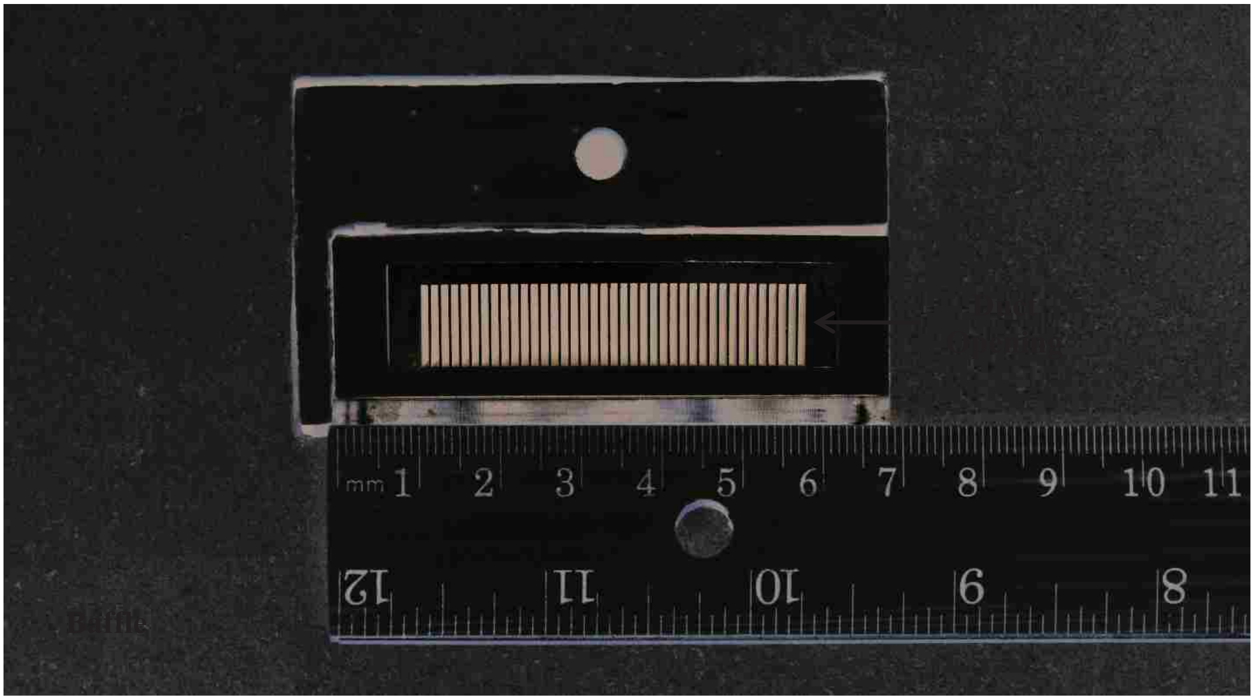

Figure 2-12 – Photograph showing a close-up of the fan and duct assembly (pictured in Fig. 2-11) mounted in the large baffle pictured in Fig. 2-8. The cutwater and secondary source are located on the duct's left side. The ruler is included for scale.

We then followed the same procedure as outlined previously in this section. Figure 2-13 shows the results obtained. The radius of the outer mesh corresponds to the uncontrolled sound field while the colored surface (radius and color) corresponds to the controlled sound field. The fan and duct assembly is oriented such that the cutwater and the secondary source lie perpendicular to the x axis, as shown in Fig. 2-13. It can be seen that the reduction is significant in magnitude (17.1 dB) and global in directionality, as the model predicts. We believe the decrease in magnitude (from 37 dB to 17 dB) is because the sound pressure level of the speaker tone is much higher above the background noise level than the sound pressure level of the fan tone. Furthermore, when the test is repeated, a mean sound power reduction of 17.2 dB is the result with a standard deviation of 0.2 dB.

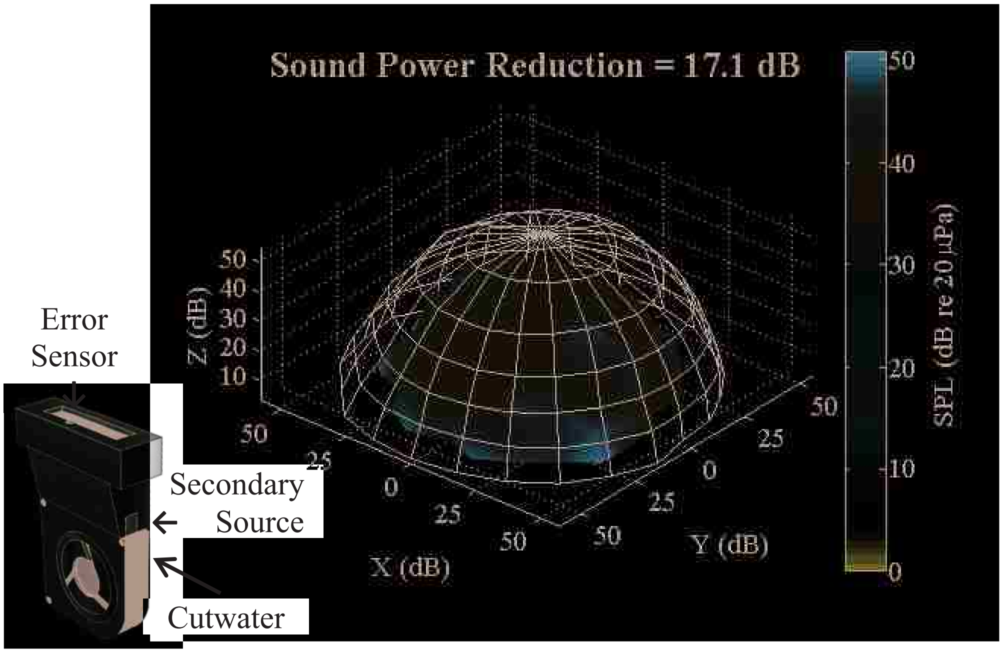

Figure 2-13 – Experimental result for control of fan exhaust. The radius of the outer mesh corresponds to the uncontrolled sound field while the colored surface (radius and color) corresponds to the controlled sound field. The axis units and color scale are in dB re 20 µPa. The fan and duct assembly is oriented as shown.

Chapter 3

ANC of Fan Inlet Noise

Chapter 2 discussed the model used to predict and control the noise propagating through the fan's exhaust. However, as mentioned in Sec. 1.3, there are two different propagation paths for the fan's noise. The first is through the fan's exhaust, while the second is through the fan's inlets. Each of these propagation paths requires a different analytical model because each of these paths is dissimilar to the other. This chapter develops the model used to predict and guide control of the noise propagating through the fan's inlets.

3.1 Two-Dimensional Free-Space Model

The first step in the development process is to determine how to best model the fan inlet system. To a first approximation, the fan mounted inside the laptop enclosure is modeled as shown in Fig. 3-1. In subplot (a), a cross-section of the laptop is shown. Note how the fan enclosure occupies almost the entire cross-section. This gives rise to subplot (b), where the fan is modeled as a line source occupying the cross-section. If the top and bottom boundaries of the laptop enclosure are assumed to be rigid, the environment looks like a line source inside a cylindrical waveguide. Mathematically, this reduces to a point source inside a circular waveguide. This leads to the first model used, the two-dimensional free-space model, where the fan is represented as a point source in an infinite two-dimensional space. This model is developed in this section, but will be discarded in favor of a superior model in the Sec. 3-2.

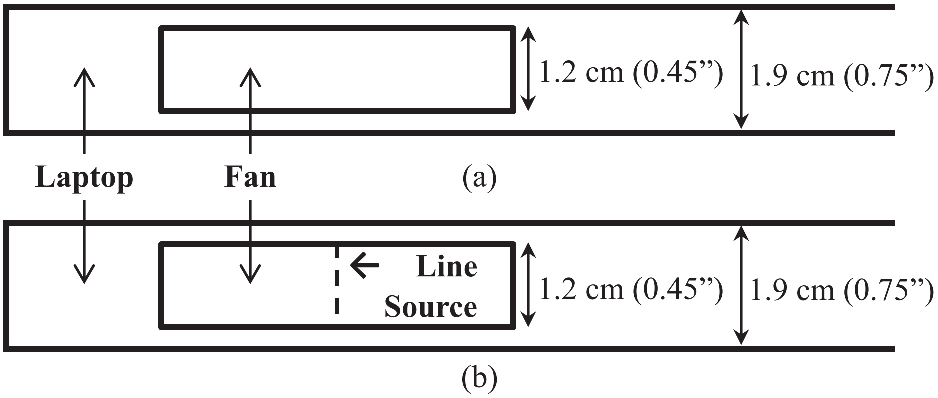

Figure 3-1 – Simplified schematic of the laptop enclosure cross-section to establish the relative scales of the fan to the laptop enclosure. Subplot (a) shows how much of the laptop enclosure cross-section is taken up by the fan. Subplot (b) shows the line source used in place of the fan as the primary source.

Readers interested in selected consequences of the two-dimensional free-space model can refer to Appendix B where comparisons between the two-dimensional free-space model and the common three-dimensional free-space model are made.

3.1 (a) Theory

The equation describing the pressure radiated from a point source in a two-dimensional free-space is

$$\nabla^2 p + k^2 p = -j\rho_0 ckQ\delta(r - r_0), \tag{3-1}$$

where p, k, ρ_0, c, and Q are as defined in the previous chapter, and r_0 indicates the location of the point source. As before, Eq. (3-1) can be solved with the use of Green's functions,

$$\nabla^2 G(r|r_0) + k^2 G(r|r_0) = -\delta(r - r_0). \tag{3-2}$$

The solution to this equation is given by

$$G(r|r_0) = \frac{j}{4} H_0^{(2)}(k|r - r_0|), \tag{3-3}$$

where $H_0^{(2)}$ denotes the zeroth-order Hankel function of the second kind, based on $e^{j\omega t}$ time dependence.[25] This is defined as

$$H_0^{(2)}(x) = J_0(x) - jY_0(x), \tag{3-4}$$

where $J_0(x)$ is the zeroth-order Bessel function of the first kind and $Y_0(x)$ is the zeroth-order Bessel function of the second kind.

Equation (3-3) defines the pressure just as was done in Sec. 2.1, yielding

$$p = j\rho_0 ckQG(r|r_0), \tag{3-5}$$

which implies that

$$p = -\frac{\rho_0 ck}{4} QH_0^{(2)}(k|r - r_0|). \tag{3-6}$$

An expression for the total power radiated by more than one point source must now be found. For this, a technique known as source coupling is used, as described in Ref. [3]. Nelson and Elliott begin by defining the total power output from a point source array as

$$\Pi = \frac{1}{2} \Re\{\boldsymbol{p}^H \boldsymbol{Q}\}, \tag{3-7}$$

where $\boldsymbol{p}$ is the vector of total pressures produced at the location of each point source, $\boldsymbol{Q}$ is the vector of complex source strengths for each source, and ^{H} denotes the Hermitian operator.[3] The boldface denotes a matrix or vector quantity. This is functionally equivalent to

$$\Pi = \frac{1}{2} \Re\{pu^*\}, \tag{3-8}$$

which we saw in Eq. (2-25).

The total pressure at any location is equal to

$$p(r) = -\frac{\rho_0 ck}{4}\sum_n Q_n H_0^{(2)}(k|r - r_n|) = -\frac{\rho_0 ck}{4}\boldsymbol{Q}^T\boldsymbol{Z}, \tag{3-9}$$

where Q_n and r_n denote the source strength and location of the nth source, while $\boldsymbol{Q}^T$ is a row vector containing the source strengths and $\boldsymbol{Z}$ is a column vector containing the Hankel function associated with each source.

If the matrix form of Eq. (3-9) is substituted into Eq. (3-7), it can be shown that

$$\Pi = \frac{1}{2}\Re\{\boldsymbol{Q}^H\boldsymbol{Z}^H\boldsymbol{Q}\} = \frac{1}{2}\boldsymbol{Q}^H\Re\{\boldsymbol{Z}^H\}\boldsymbol{Q}, \tag{3-10}$$

where the elements of $\boldsymbol{Z^H}$ are given by

$$Z_{i,j} = -\frac{\rho_0 ck}{4}H_0^{(2)}\left(k\left|r_i - r_j\right|\right), \tag{3-11}$$

where r_i and r_j are the locations of the ith and jth point sources. For details on the equality in Eq. (3-10), see Sec. 8.12 in Ref [3].

Equation (3-10) is now separated into four different parts,

$$\Pi = \frac{1}{2}\left[\boldsymbol{Q}_p^H\Re\left\{\boldsymbol{Z}_{p,p}^H\right\}\boldsymbol{Q}_p + \boldsymbol{Q}_p^H\Re\left\{\boldsymbol{Z}_{p,s}^H\right\}\boldsymbol{Q}_s + \boldsymbol{Q}_s^H\Re\left\{\boldsymbol{Z}_{s,p}^H\right\}\boldsymbol{Q}_p + \boldsymbol{Q}_s^H\Re\left\{\boldsymbol{Z}_{s,s}^H\right\}\boldsymbol{Q}_s\right], \tag{3-12}$$

where $\boldsymbol{Q}_p$ and $\boldsymbol{Q}_s$ are the vectors containing the source strengths of the primary and secondary sources respectively, and

$$\left[Z_{p/s,p/s}\right]_{i,j} = -\frac{\rho_0 ck}{4}H_0^{(2)}\left(k\left|r_{(p/s)_i} - r_{(p/s)_j}\right|\right), \tag{3-13}$$

which is the impedance between the ith and jth primary/secondary sources as the subscripts in Eq. (3-12) indicate. The first term in Eq. (3-12) is the power due to the primary sources operating by themselves, while the last term in Eq. (3-12) is the power due to the secondary sources operating by themselves. The middle two terms are the power due to the primary sources acting on the secondary sources, or vice versa.

Now the overall power, Π, must be minimized. To do this, the derivative of Eq. (3-12) is taken with respect to $\boldsymbol{Q}_s$ and set equal to zero,

$$\frac{\partial \Pi}{\partial \boldsymbol{Q}_s} = \frac{1}{2}\left[2\Re\{\boldsymbol{Z}_{s,p}^{H}\}\boldsymbol{Q}_p + 2\Re\{\boldsymbol{Z}_{s,s}^{H}\}\boldsymbol{Q}_{s_O}\right] = \boldsymbol{0} \Rightarrow \qquad \textbf{(3-15a)}$$

$$\boldsymbol{Q}_{s_O} = \Re\{\boldsymbol{Z}_{s,s}^{H}\}^{-1}\Re\{\boldsymbol{Z}_{s,p}^{H}\}\boldsymbol{Q}_p, \qquad \textbf{(3-15b)}$$

where $\boldsymbol{Q}_{s_O}$ is the optimal secondary source strength needed to minimize the radiated sound power.

When Eq. (3-15b) is substituted into Eq. (3-12), this leads to

$$\Pi_{min} = \frac{1}{2}\left[\boldsymbol{Q}_p^{H}\Re\{\boldsymbol{Z}_{p,p}^{H}\}\boldsymbol{Q}_p + \boldsymbol{Q}_p^{H}\Re\{\boldsymbol{Z}_{p,s}^{H}\}\boldsymbol{Q}_s + \boldsymbol{Q}_s^{H}\Re\{\boldsymbol{Z}_{s,p}^{H}\}\boldsymbol{Q}_p + \boldsymbol{Q}_s^{H}\Re\{\boldsymbol{Z}_{s,s}^{H}\}\boldsymbol{Q}_s\right]$$

$$= \frac{1}{2}\boldsymbol{Q}_p^{H}\left[\Re\{\boldsymbol{Z}_{p,p}^{H}\} + \Re\{\boldsymbol{Z}_{p,s}^{H}\}\Re\{\boldsymbol{Z}_{s,s}^{H}\}^{-1}\Re\{\boldsymbol{Z}_{s,p}^{H}\} + 2\,\Re\{\boldsymbol{Z}_{s,p}\}\Re\{\boldsymbol{Z}_{s,s}\}^{-1}\Re\{\boldsymbol{Z}_{s,p}^{H}\}\right]\boldsymbol{Q}_p. \qquad \textbf{(3-16a)}$$

Furthermore, when Eq. (3-15b) is substituted into an expanded version of Eq. (3-5), it can be shown that

$$p = -\frac{\rho_0 ck}{4}\left[\sum_{p} Q_p H_0^{(2)}\left(k|r - r_p|\right) + \sum_{s} Q_{s_O} H_0^{(2)}\left(k|r - r_s|\right)\right], \qquad \textbf{(3-16b)}$$

which yields the pressure field corresponding to maximum attenuation of the radiated power. This pressure field shows near-field nodal lines that, as before, are the ideal locations for error sensors.

In order to more easily test this theory, this development needs a small modification. An infinite rigid plane is placed such that it bisects the two-dimensional free space. This transforms the free-space model into a half-space model. This causes all point sources to have duplicate or “imaged” point sources across the aforementioned plane. When these additional sources are

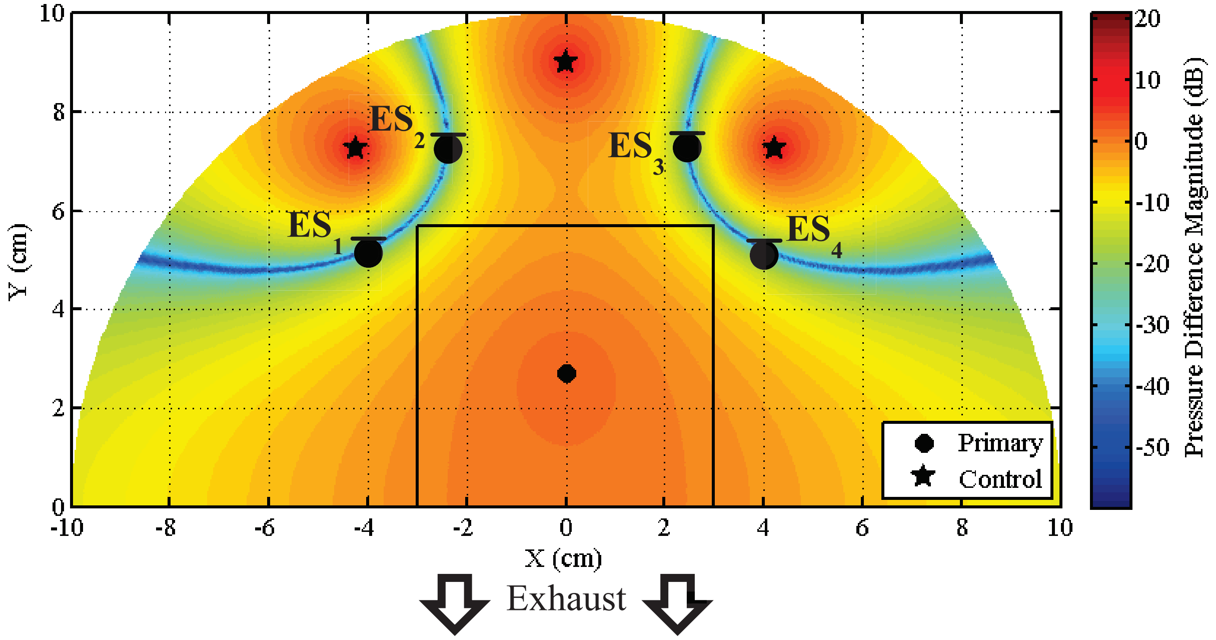

Figure 3-2 – Minimized pressure map that results when the radiation from the two-dimensional half space model is minimized. The square in the middle represents the fan enclosure. The dot represents the primary source location (fan), while the stars represent the secondary source locations. For experimental validation, error sensors (ES$_1$–ES$_4$) are placed along nodal lines as indicated. Axis units are in centimeters while the color scale is in dB relative to the uncontrolled field.

incorporated into Eq. (3-16b), the resultant pressure field is shown for one source configuration in Fig. 3-2.

With this modification the predicted power reduction as a function of frequency is calculated, according to Eq. (3-16a). This is shown in Fig. 3-3. Observe that below approximately 1500 Hz, the power reduction in dB increases linearly as a function of frequency. Furthermore, the point of zero power reduction occurs at $f = 1650$ Hz, which corresponds to a kd of approximately 0.6π. For comparisons between these results and those for a three-dimensional free-space model, see Appendix B.

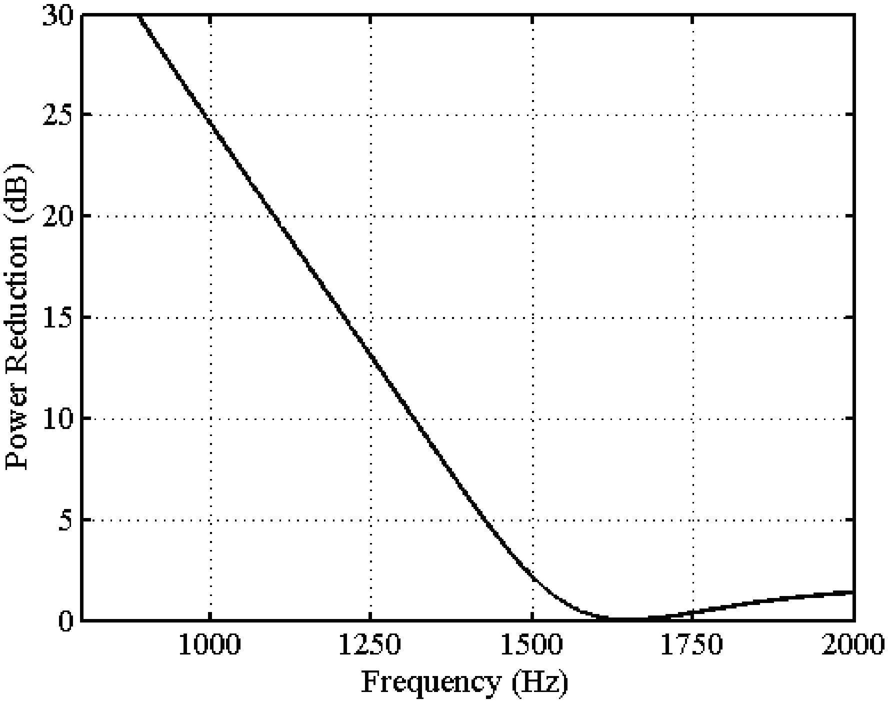

Figure 3-3 – Predicted power reduction in dB as a function of frequency for the two-dimensional half-space model for the source configuration shown in Fig. 3-2.

3.1 (b) Experiment

The next step in the development process is to experimentally verify the two-dimensional half-space model. To do this, we constructed a two-dimensional waveguide from two semicircular (36” radius) sheets of 1/16” thick Plexiglas. We first mounted the fan, secondary sources (Sonion 0935 loudspeakers), and error sensors (1/8” electret microphones) inside the waveguide close to the focus of the semicircle (the point that is equidistant from all points that lie along the perimeter of the semicircle), as indicated in Fig. 3-2. Then, we placed the entire assembly on a large baffle. Third, we took measurements with the semicircular array of microphones (described in Sec. 2.5) that we inserted into the waveguide. This setup is shown in Fig. 3-4.

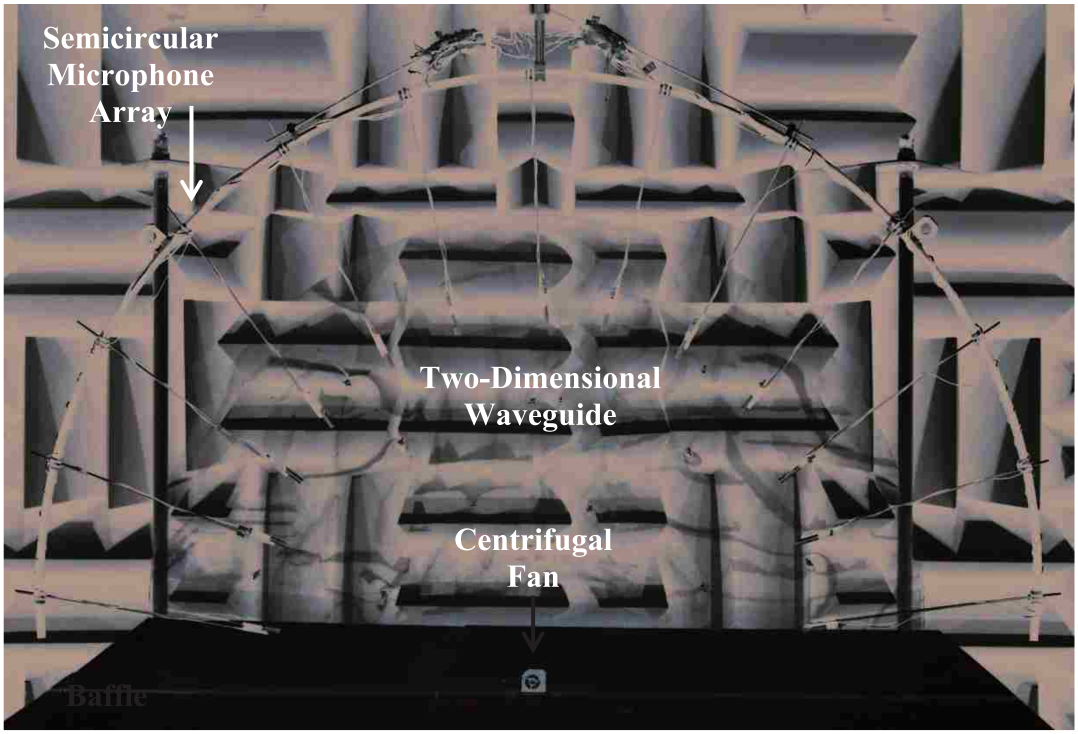

Figure 3-4 – Photo showing the experimental setup used to validate the two-dimensional free space model. The fan is placed between two semicircular plexiglas sheets and mounted on a large wooden baffle. A semicircular array of microphones extends into the waveguide, as pictured above.

However, when we performed this experiment the power reduction did not match predicted values. Figure 3-5 shows that at 1 kHz, the reduction obtained is only 8.9 dB. Though this result is significant, the reduction is significantly less than the approximately 24 dB predicted by the model, as shown in Fig. 3-3.

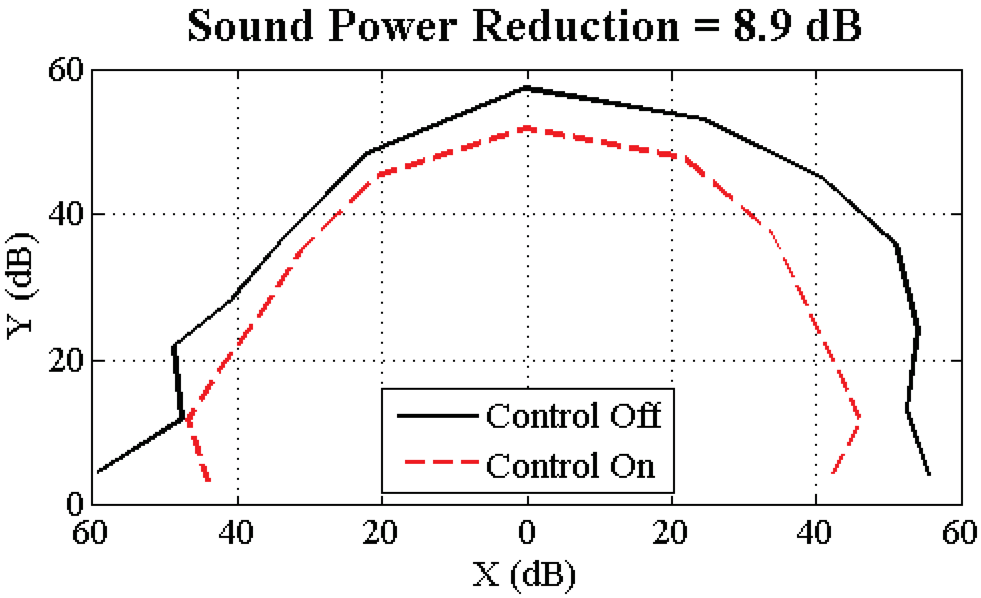

Figure 3-5 – Figure showing 11.7 dB of power reduction of the fan at approximately 1 kHz in the two-dimensional half-space waveguide. The solid line is the sound field with control off, while the dashed line is the sound field with control on. The difference of the sum of the two curves squared is equal to the sound power reduction.

There are three possible reasons for this discrepancy. First, we assumed point source excitations for both the primary and secondary sources. In reality, this is not the case, especially when considering the fan. Second, it is possible that the fan does not produce enough tonal energy to permit 25 dB of power reduction before the noise floor limits the performance. Third, even though the waveguide is meant to simulate a free-space environment, there are modal effects present which invalidate the model.

To test the first and second reasons, we replaced the fan with a Sonion 0935 loudspeaker and performed the test again. This loudspeaker's output is much louder than the fan's tonal noise, which provides some indication of whether the attained power reduction is limited by noise. Furthermore, this loudspeaker is very small with respect to a wavelength (6.3 mm x 4.29 mm x 2.96 mm). This means that it can be approximated as a point source. This test also gives

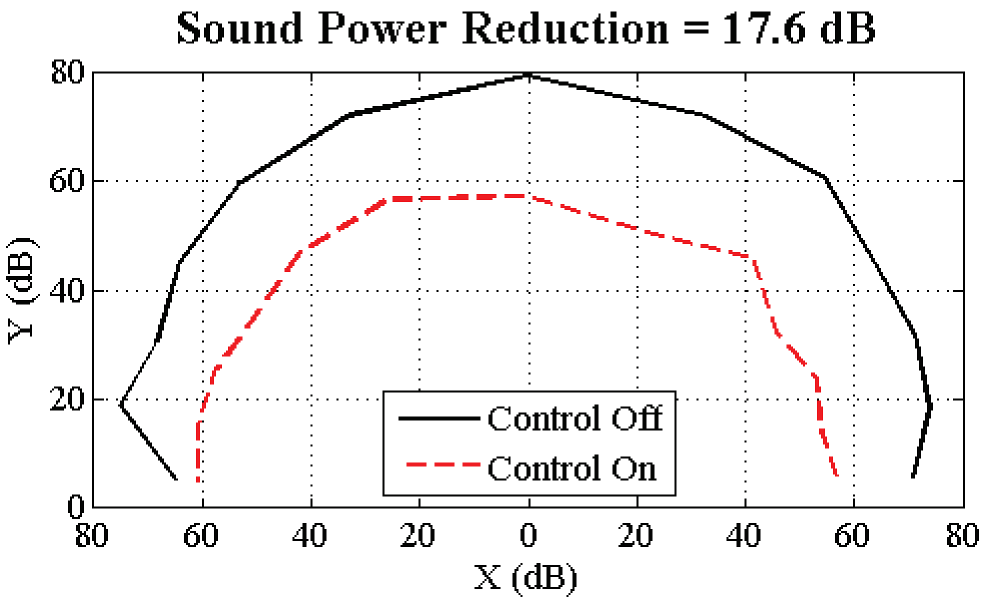

Figure 3-6 – Figure showing 16.4 dB of power reduction of a loudspeaker at 1 kHz in the two-dimensional half-space waveguide. The solid line is the sound field with control off, while the dashed line is the sound field with control on. The difference of the sum of the two curves squared is equal to the sound power reduction.

some indication whether the attained power reduction is limited by the distributed nature of the fan.

This test resulted in a reduction of 17.6 dB at 1 kHz, shown in Fig. 3-6. This is much greater than the 8.9 dB of sound power reduction obtained with the fan, but still lower than the predicted value of 24 dB of sound power reduction. Thus, both the distributed nature of the fan and its relatively high noise floor could play a part in the lower-than-predicted result, but cannot account for the entire discrepancy. This led us to consider the possible modal effects of the waveguide.

Evidence that the waveguide is modal is shown in Fig. 3-7. This figure shows a measurement of the power radiated from the fan as a function of frequency. The black curve corresponds to when the fan is in the waveguide, while the red curve corresponds to when the fan

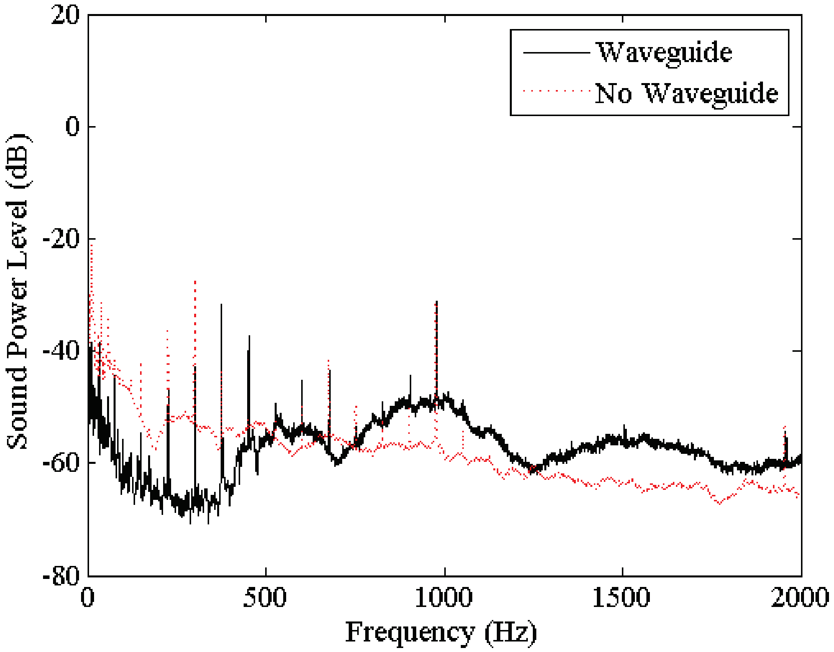

Figure 3-7 – Power radiated from fan when inside and outside the two-dimensional waveguide. The spikes correspond to the fan's tones, while the uneven noise floor is an indication of modes in the supposedly half-space waveguide.

is removed from the waveguide. The harmonic spikes in the spectrum correspond to the fan's tones, which are integer multiples of the fan's angular velocity in revolutions per second. What is relevant to this discussion, however, is the differences in the respective noise floors. The broad peaks in the broadband noise floor on the waveguide curve suggest the presence of modes, especially since these broad peaks are not present when the fan is removed from the waveguide.

To more conclusively determine the origin of the reduced performance, we performed two sets of power reduction tests from 900 Hz to 1400 Hz in 100 Hz increments. In one set, we used the fan as the noise source. In the other set, we replaced the fan with the Sonion loudspeaker mentioned previously. Each test was repeated five times to ensure reproducibility. These results are shown in Fig. 3-8. Notice that from 1200 Hz to 1400 Hz, both the loudspeaker and the fan results follow closely the predicted curve. However, below 1200 Hz the fan and loudspeaker results diverge from the predicted values. This suggests four things. First, the fact that the fan and loudspeaker results are very close from 1200 Hz to 1400 Hz suggests that the distributed nature of the fan is not important—otherwise, there would be a sizeable discrepancy between fan and speaker irrespective of frequency. Second, the difference between the fan and the loudspeaker at lower frequencies is primarily due to the loudspeaker being louder than the fan. Third, above 1200 Hz near-field effects dominate the power reduction. This suggests that modal effects are not important above 1200 Hz, at least for the source configuration shown in Fig. 3-2. However, below 1200 Hz the large discrepancy between the loudspeaker results and the predicted power reduction can be attributed to modal effects. Thus, below 1200 Hz (the frequency range in which we are most interested), modal effects must be included in the model in order to be accurate.

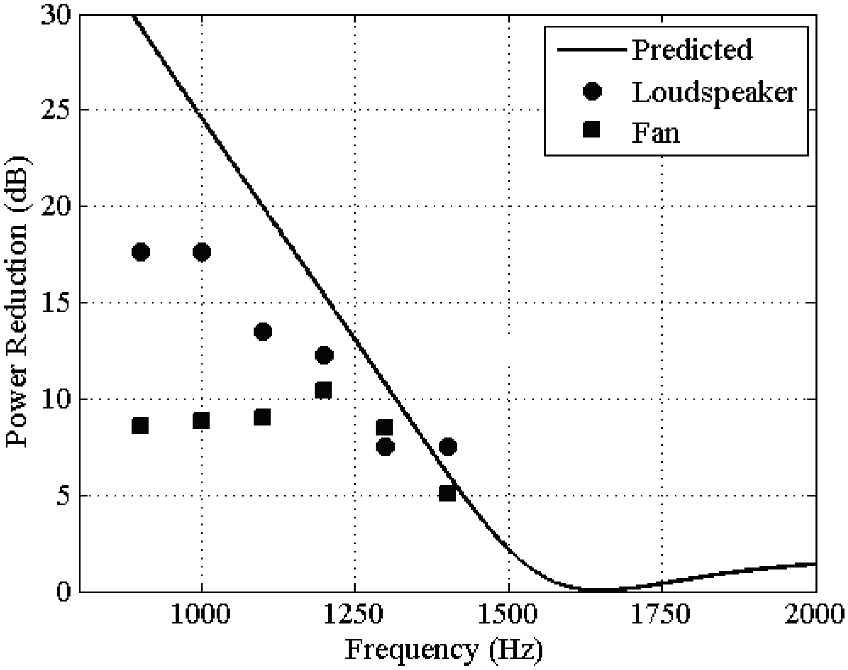

Figure 3-8 – Power reduction in dB using both the loudspeaker and the fan as the primary source in the two-dimensional free space model. The source configuration is as shown in Fig. 3-2. The line shows the predicted power reduction, the circles show experimental data for the loudspeaker, and the squares show experimental data for the fan.

3.2 Two-Dimensional Modal Model

Section 3.1 shows the necessity of including modal effects in the theoretical development. This prompts a severe modification to the model.

Instead of a two-dimensional half-space, line sources are placed inside of a rectangular enclosure, sized such that one of its dimensions (z) is much smaller than the other two; this is meant to model the mock laptop enclosure that is used for this research.

Because the wavelengths of the frequencies of interest are much larger than the smallest dimension of this enclosure, it is neglected in the analysis. This leaves a collection of point sources inside a two-dimensional rectangular box. This is the final framework for the second model used, the two-dimensional modal model, shown in Fig. 3-9.

3.2 (a) Theory

The equation for the radiation of a point source in a two-dimensional rectangular enclosure is given by

$$\nabla^2 p + k^2 p = -j\rho_0 ckQ\delta(x - x_0)\delta(y - y_0), \tag{3-17}$$

which follows the same form as all other governing equations shown in this thesis. Again, this can be solved through the use of Green's functions,

$$\nabla^2 G(r|r_0) + k^2 G(r|r_0) = -\delta(x - x_0)\delta(y - y_0). \tag{3-18}$$

When Eq. (3-18) is solved, it is found that

$$G(r|r_0) = -\sum_{N=0}^{\infty} \frac{\Psi_N(r_0)\Psi_N(r)}{(k^2 - k_N^2)A\Lambda_N}, \tag{3-19}$$

where N is the modal index (composed of the ordered pair (n_x, n_y)), k is the wavenumber, A is the area of the enclosure, r_0 is the location of the point source,

$$\Lambda_N = \begin{cases} 1, & n_x = 0 \text{ and } n_y = 0 \\ \frac{1}{2}, & n_x \neq 0 \text{ or } n_y \neq 0 \\ \frac{1}{4}, & \text{otherwise} \end{cases}, \tag{3-20}$$

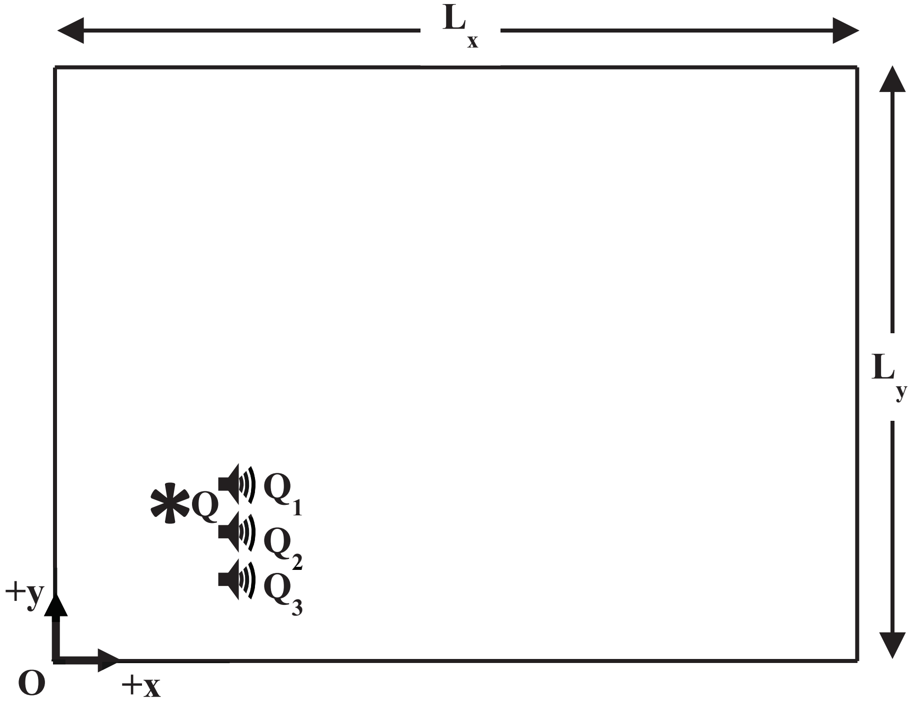

Figure 3-9 – Drawing of the two-dimensional rectangular enclosure the model simulates. The primary source that models the fan is located as indicated with a source strength Q, while secondary sources are placed as shown with source strengths Q_1, Q_2, and Q_3.

and

$$k_N^2 = \left(\frac{n_x \pi}{L_x}\right)^2 + \left(\frac{n_y \pi}{L_y}\right)^2, \tag{3-21}$$

where n_x and n_y are modal indices in each direction.[26]

When the boundaries of the enclosure are assumed to be rigid, this leads to

$$\Psi_N(x, y) = \cos\left(\frac{n_x \pi}{L_x} x\right) \cos\left(\frac{n_y \pi}{L_y} y\right). \tag{3-22}$$

This yields the result

$$G(r|r_0) = -\sum_{N=0}^{\infty} \frac{\cos\left(\frac{n_x \pi}{L_x} x_0\right) \cos\left(\frac{n_y \pi}{L_y} y_0\right)}{(k^2 - k_N^2) A \Lambda_N} \cos\left(\frac{n_x \pi}{L_x} x\right) \cos\left(\frac{n_y \pi}{L_y} y\right). \tag{3-23}$$

The mock laptop enclosure has ports along the boundaries at $x = 0$ and $x = L_x$ from which sound radiates. The radiation from these ports can be modeled by incorporating damping into the model along these boundaries. We do this by making k_N complex,

$$\tilde{k}_N^2 = \left(\frac{n_x\pi}{L_x} + j\frac{\delta_b}{c}\right)^2 + \left(\frac{n_y\pi}{L_y}\right)^2, \tag{3-24}$$

where δ_b is a constant proportional to the damping of the boundaries in x.[26]

This leads to the full equation for the pressure radiated from a point source in a two-dimensional rectangular enclosure with lossy boundaries, given by

$$p(r) = -j\rho_0 ckQ \sum_{N=0}^{\infty} \frac{\cos\left(\frac{n_x\pi}{L_x}x_0\right)\cos\left(\frac{n_y\pi}{L_y}y_0\right)}{\left(k^2 - \tilde{k}_N^2\right)A\Lambda_N} \cos\left(\frac{n_x\pi}{L_x}x\right)\cos\left(\frac{n_y\pi}{L_y}y\right). \tag{3-25}$$

Next, the power radiated from the enclosure must be solved for and minimized. This is represented by the power dissipated by the losses in the model. Using the source coupling concept developed by Nelson and Elliott,[3] the total power radiated from the enclosure is given by

$$\Pi = \frac{1}{2}\boldsymbol{Q}^H \Re\{\boldsymbol{Z}^H\}\boldsymbol{Q}, \tag{3-26}$$

where $\boldsymbol{Q}$ is the vector of complex source strengths, ^{H} denotes the Hermitian operator, and the elements of $\boldsymbol{Z^H}$ are given by

$$Z_{i.j} = -j\rho_0 ck \sum_{N=0}^{\infty} \frac{\cos\left(\frac{n_x\pi}{L_x}x_i\right)\cos\left(\frac{n_y\pi}{L_y}y_i\right)\cos\left(\frac{n_x\pi}{L_x}x_j\right)\cos\left(\frac{n_y\pi}{L_y}y_j\right)}{\left(k^2 - \tilde{k}_N^2\right)A\Lambda_N}. \tag{3-27}$$

As before, Eq. (3-26) is separated into primary and secondary components,

$$\Pi = \frac{1}{2}\left[\boldsymbol{Q}_p^H \Re\{\boldsymbol{Z}_{p,p}^H\}\boldsymbol{Q}_p + \boldsymbol{Q}_p^H \Re\{\boldsymbol{Z}_{p,s}^H\}\boldsymbol{Q}_s + \boldsymbol{Q}_s^H \Re\{\boldsymbol{Z}_{s,p}^H\}\boldsymbol{Q}_p + \boldsymbol{Q}_s^H \Re\{\boldsymbol{Z}_{s,s}^H\}\boldsymbol{Q}_s\right]. \tag{3-28}$$

Following the analysis of Eqs. (3-15a) – (3-15b), it can be shown that

$$\boldsymbol{Q}_{s_o} = \Re\{\boldsymbol{Z}_{s,s}^H\}^{-1}\Re\{\boldsymbol{Z}_{s,p}^H\}\boldsymbol{Q}_p. \quad \textbf{(3-29)}$$

When Eq. (3-29) is substituted into an expanded form of Eq. (3-25), this leads to

$$p(r) = -j\rho_0 ck \sum_{N=0}^{\infty} \frac{\sum_p Q_p \Psi_N(r_p) + \sum_s Q_{s_o} \Psi_N(r_s)}{(k^2 - \tilde{k}_N^2) A \Lambda_N} \Psi_N(r), \quad \textbf{(3-30)}$$

where the sums over p and s denote summing over all primary and secondary sources respectively.

Equation (3-30) generates the pressure field which is a consequence of the minimum power condition. As before, the nodal lines which result are the ideal locations for error sensors to be placed. The result of Eq. (3-30) for the source configuration pictured in Fig. 3-9 is shown in Fig. 3-10.

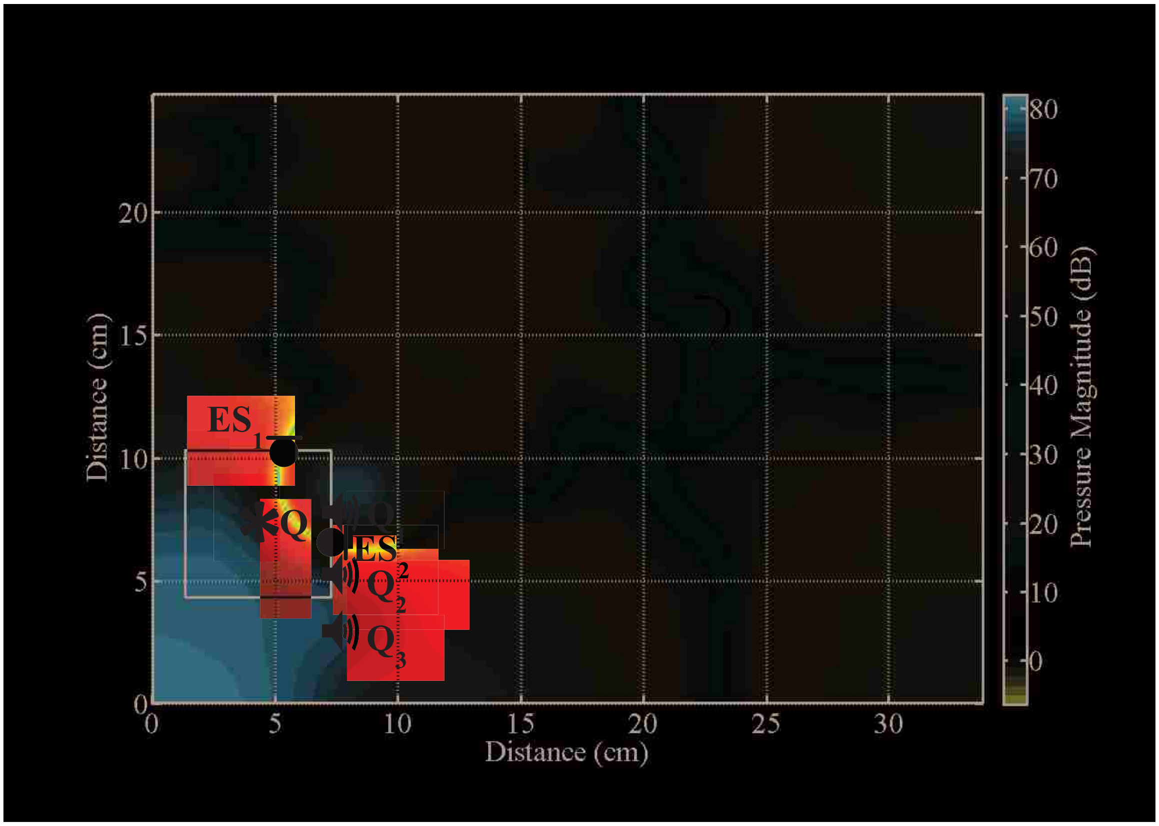

Figure 3-10 – Minimized pressure map that results when the radiation from the rectangular enclosure is minimized. The square in the bottom-left represents the fan, while the secondary sources are placed in the locations indicated. For experimental validation, error sensors are placed along nodal lines as indicated. Axis units are in centimeters while the color scale is in dB.

3.2 (b) Experiment

The final step in the development of the model is to validate this new theoretical model experimentally. To do so, we placed the fan, secondary sources (Regal R-15-E), and error sensors (1/8" electret microphones) in the mock laptop enclosure according to Fig. 3-10. This is pictured in Fig. 3-11. We mounted the enclosure in the baffle mentioned in Sec. 2-5 with the exhaust of the fan venting below it. We used the semicircular array of microphones shown in Sec. 2-5 to take accurate sound power measurements, both with and without control. This experimental setup is shown in Fig. 3-12, with a close-up in Fig. 3-13. The difference between

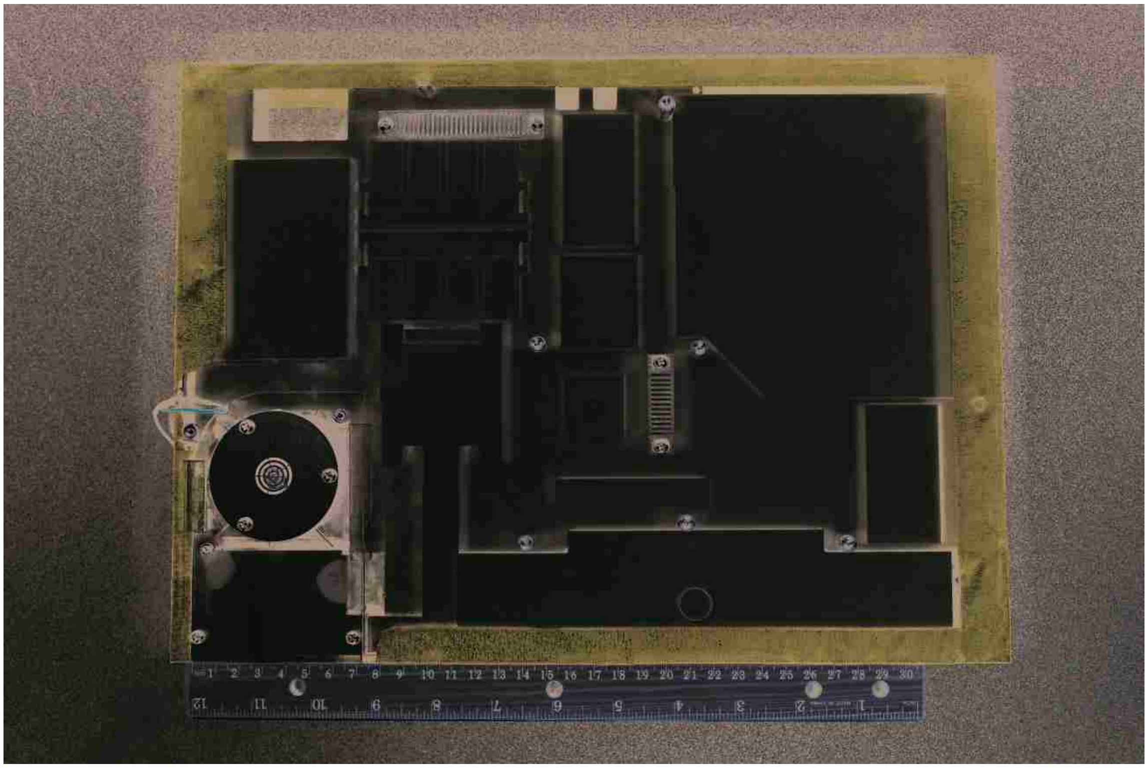

Figure 3-11 - Photograph of the mock laptop enclosure. The fan and duct assembly is mounted in the bottom-left corner of the enclosure. The ruler is included for scale.

the two pressure measurements is the pressure reduction in any direction. When we took the difference of the summed squared pressures, we obtained the overall sound power reduction.

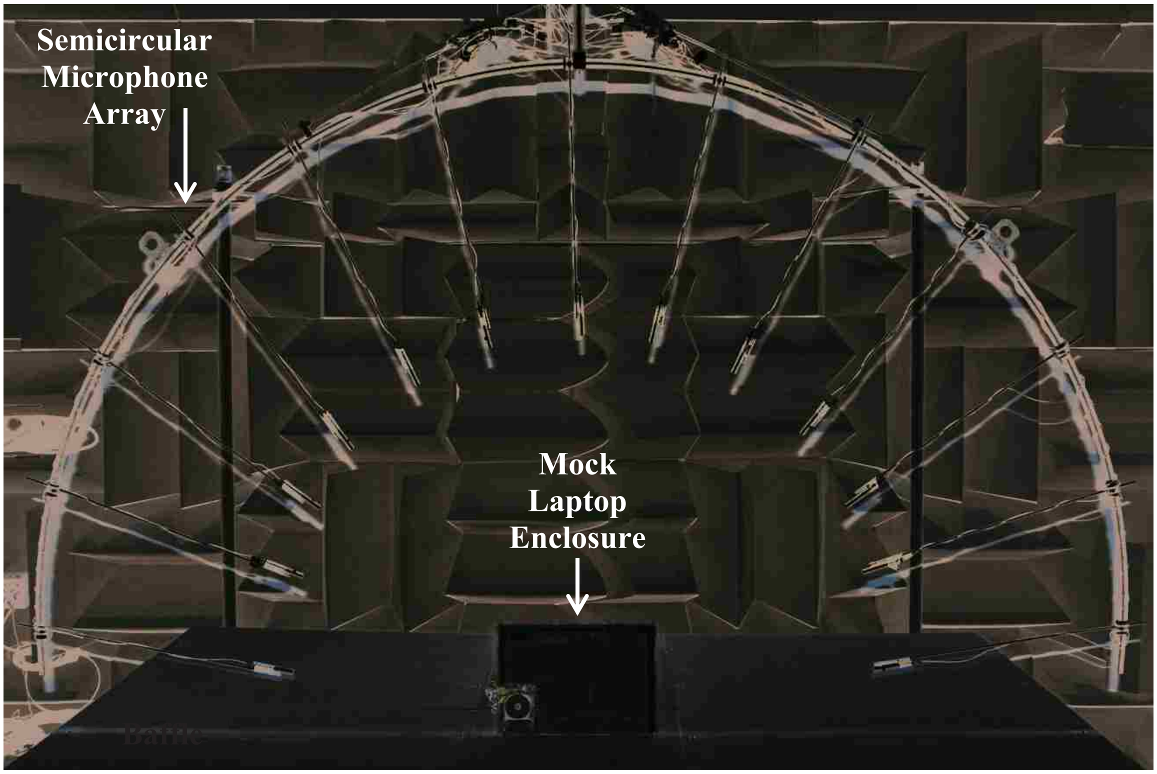

Figure 3-12 – Photograph showing the experimental setup used to validate the two-dimensional modal model. The fan is placed in a mock laptop enclosure and mounted on a large wooden baffle (7½ feet square) such that the fan's exhaust vents below the baffle. A semicircular array of microphones (56 cm radius) is suspended overhead.

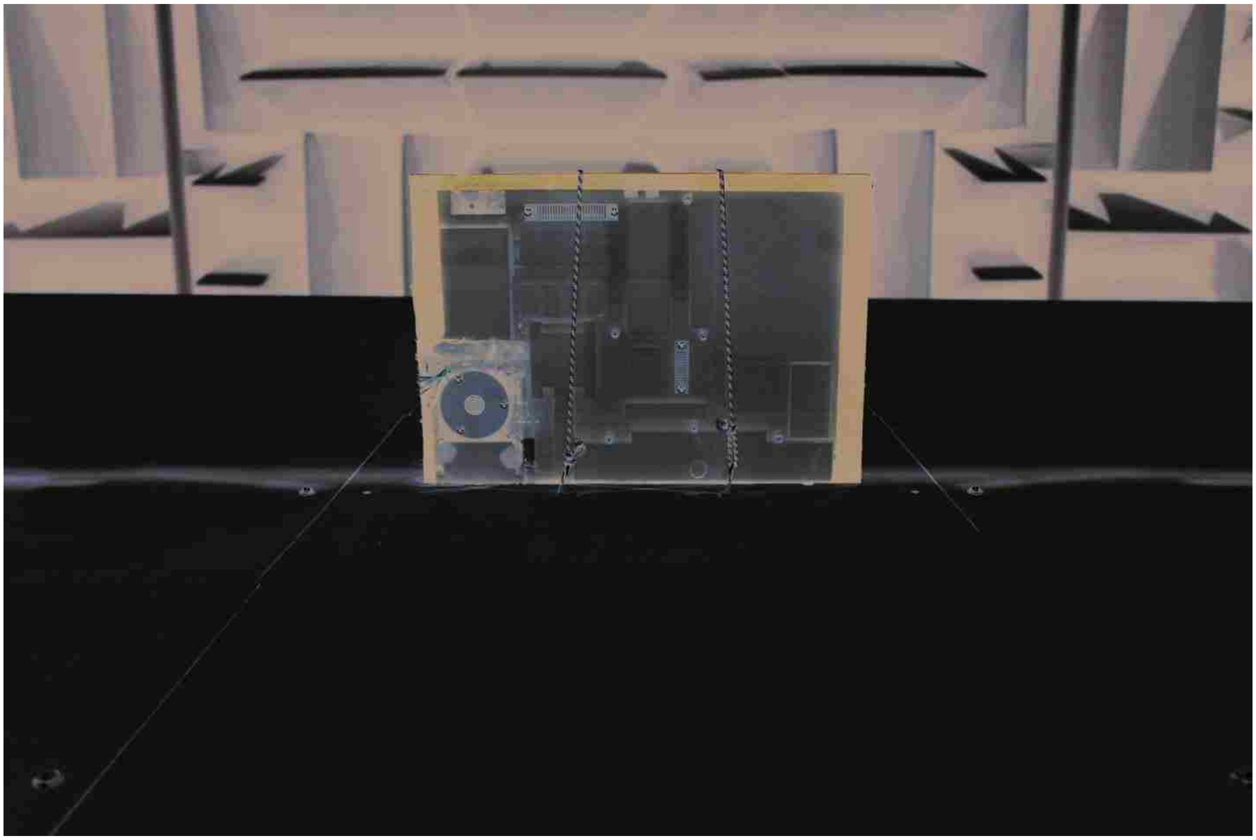

Figure 3-13 – Close-up of the experimental setup shown in Fig. 3-13.

Figure 3-14 shows the results of this study. When the fan operates at approximately 1 kHz, there is a 12.5 dB reduction in global sound power. Additionally, there is an 21.6 dB reduction in pressure in the direction of the operator position, *i.e.* the direction the operator would be when he/she uses the laptop. For these tests, it is located along the y-axis at a 50^o angle from the baffle plane. Note the location is indicated by a dot in Fig. 3-14.

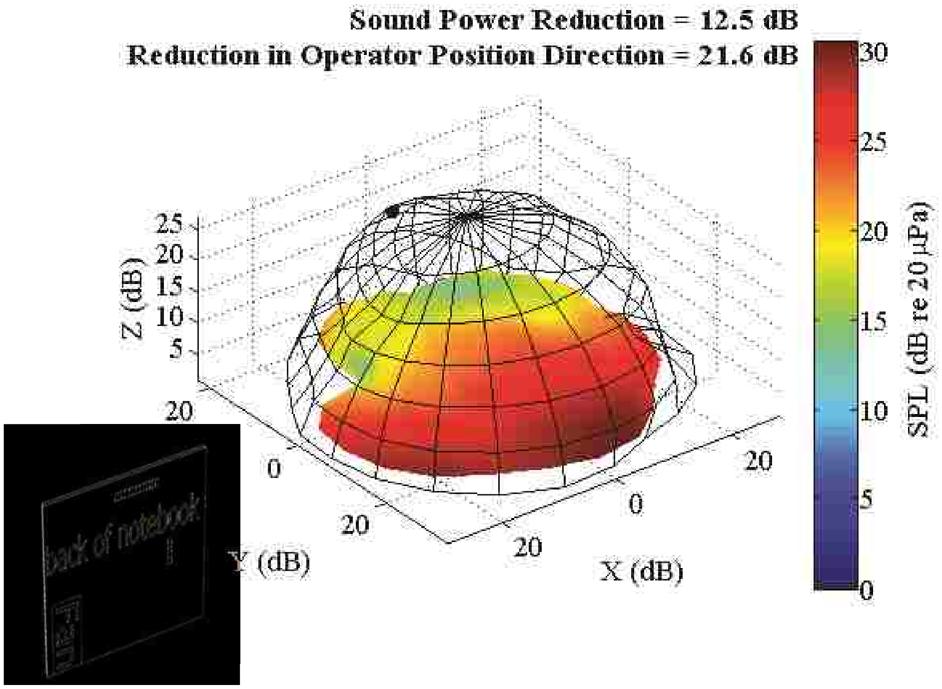

Figure 3-14 – Experimental result for control of fan inlet when the model's recommendations are followed. The outer mesh is the uncontrolled sound field while the colored surface is the controlled sound field. The operator position direction is indicated by the black dot on the back side of the figure. The axis units and color scale are in dB re 20 μPa. The laptop enclosure is oriented as shown.

The final step was to move the error sensors from their predicted ideal locations to see if the sound power reduction is truly maximized when the model's predictions are followed. Figure 3-15 shows the positions used for this test. Note that three error sensors were used for this test instead of two. This is to ensure that the near-field pressure generated from this sensor set has no resemblance to the predicted ideal near-field pressure.

Figure 3-16 shows the results for this test. Note that the reduction we obtained when we followed the model's recommendations disappears. This suggests that the model derived in this section is useful in determining the proper configuration of the control system in order to achieve significant attenuation of the sound field.

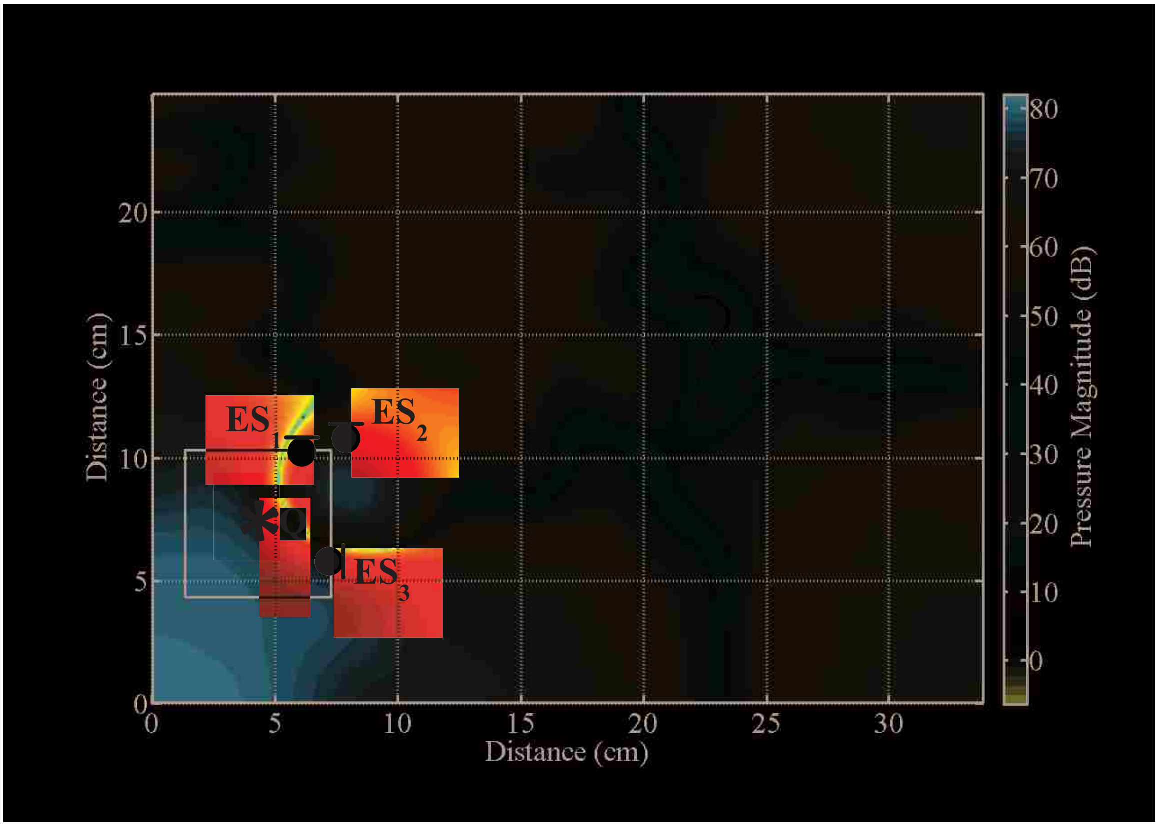

Figure 3-15 – Incorrect error sensor positions used to validate the two-dimensional modal model. The minimized pressure map that results when the radiation from the rectangular enclosure is minimized is shown for reference. The square in the bottom-left represents the fan. Axis units are in centimeters while the color scale is in dB.

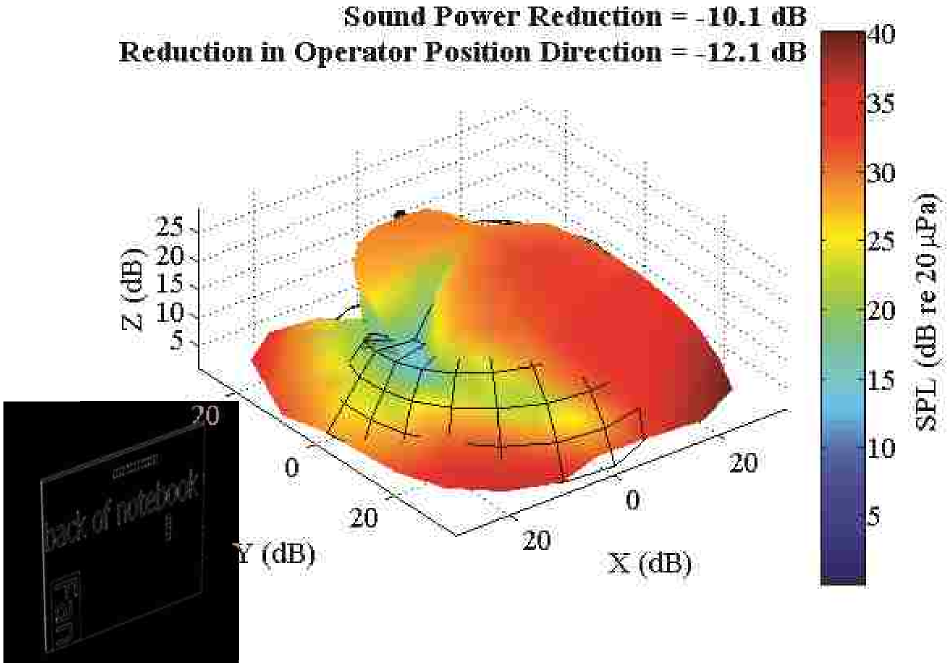

Figure 3-16 – Experimental result for control of fan inlet when the model's recommendations are *not* followed, as shown in Fig. 3-15. The outer mesh is the uncontrolled sound field while the colored surface is the controlled sound field. The operator position direction is indicated by the black dot on the back side of the figure. The axis units and color scale are in dB re 20 μPa. The laptop enclosure is oriented as shown.

Chapter 4

ANC of the Combined System

The previous two chapters discussed the individual analytical models used to predict and control the noise propagating through the fan's inlets and exhaust. However, these models need to be combined in order to control the noise radiated from the entire laptop enclosure. This chapter explains the results obtained when the combined model is applied to the fan radiating from the mock laptop enclosure. It considers two versions of the combined model: an uncoupled model, and a coupled model.

4.1 Uncoupled Model

The models developed in Chap. 2–3 are first assumed to be uncoupled (*i.e.* when combined, they act independently of each other). This gives rise to the uncoupled model. To test this model, we placed secondary sources (Regal R-15-E) in the mock laptop enclosure as shown in Figs. 2-5 (for the exhaust) and 3-11 (for the inlet). We then placed error sensors (1/8" electret microphones) in the ideal locations shown in Figs. 2-6 (for the exhaust) and 3-11 (for the inlet). This gives rise to the configuration shown in Fig. 4-1. Q_1, Q_2, and Q_3 are the inlet secondary sources, while Q_4 is the exhaust secondary source. ES_1 and ES_2 are the inlet error sensors, while ES_3 is the exhaust error sensor.

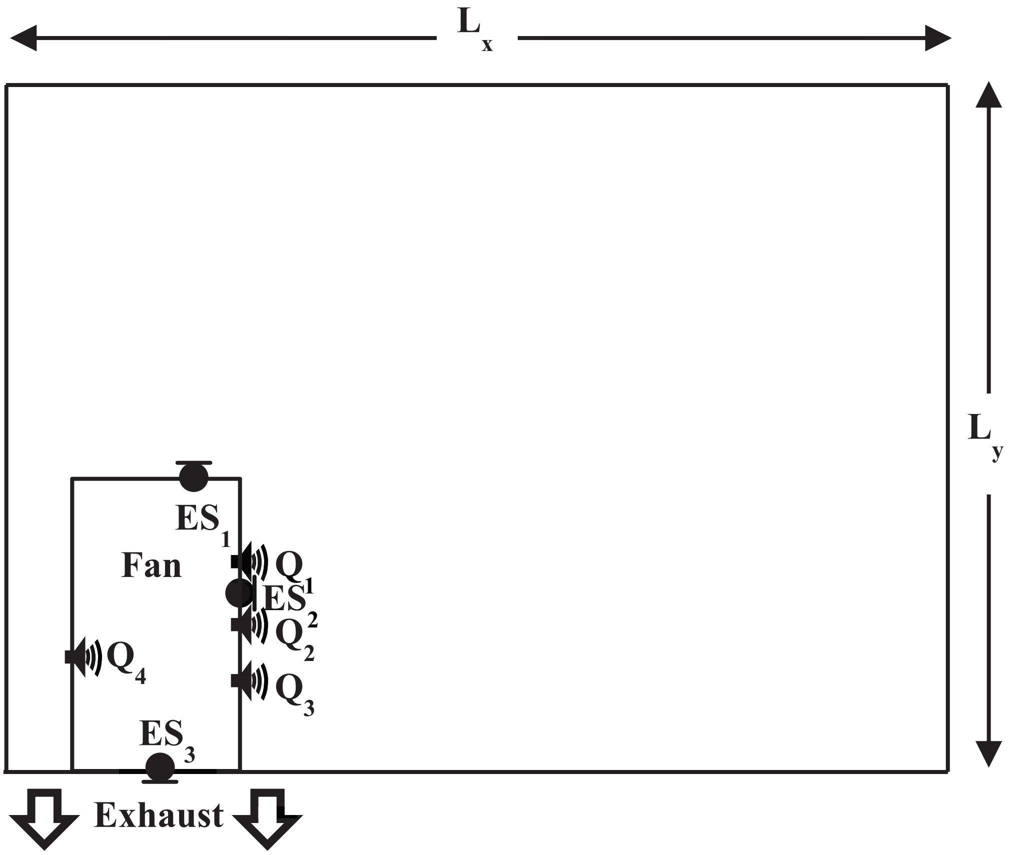

Figure 4-1 – Drawing of the two-dimensional rectangular enclosure the model simulates. The larger rectangle represents the enclosure itself while the smaller rectangle represents the fan and exhaust duct assembly. Secondary sources are placed as shown with source strengths Q_1, Q_2, Q_3, and Q_4, while error sensors are placed at locations ES_1, ES_2, and ES_3.

We first placed the entire assembly (pictured in Fig. 4-2) underneath the semicircular array of microphones as shown in Fig. 4-3. We ran the fan without the ANC system and measured the total sound power radiated from the enclosure. We then operated the fan with exhaust and inlet control systems running simultaneously. We optimized each set of secondary sources and error sensors independently of the other set. The results of this test are shown in Fig. 4-4. Note that reductions on the order of 13–14 dB were achieved for both global sound power and pressure at the operator position, *i.e.* the position the operator would be when he/she uses the laptop as defined by ISO 7779 (25 cm in front of the laptop enclosure and 45 cm above it).

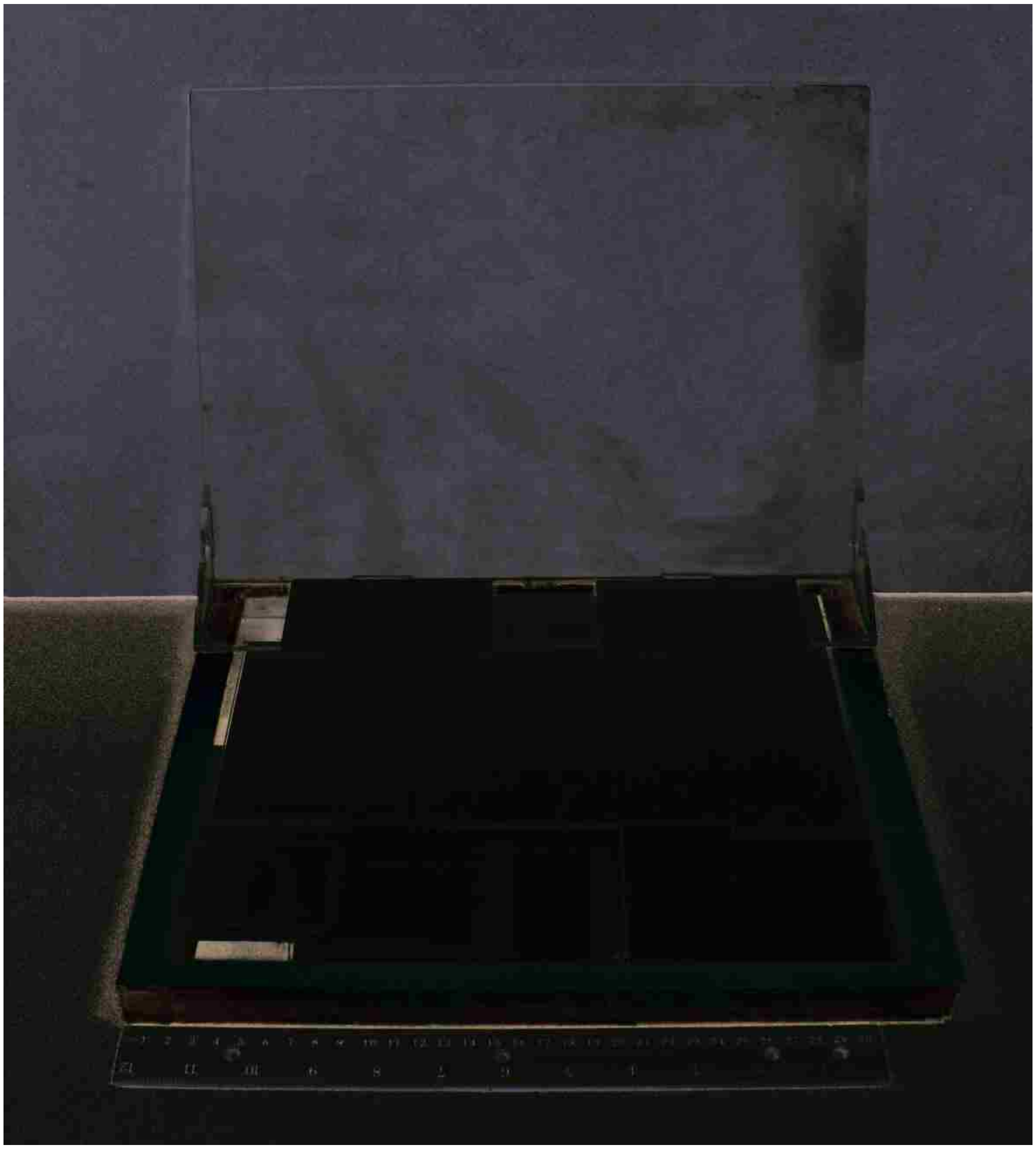

Figure 4-2 – Picture showing the mock laptop enclosure with the faux LCD screen attached. The fan and duct assembly shown in Fig. 2-11 is mounted in the back left-hand corner with the exhaust venting backwards. The ruler is included for scale.

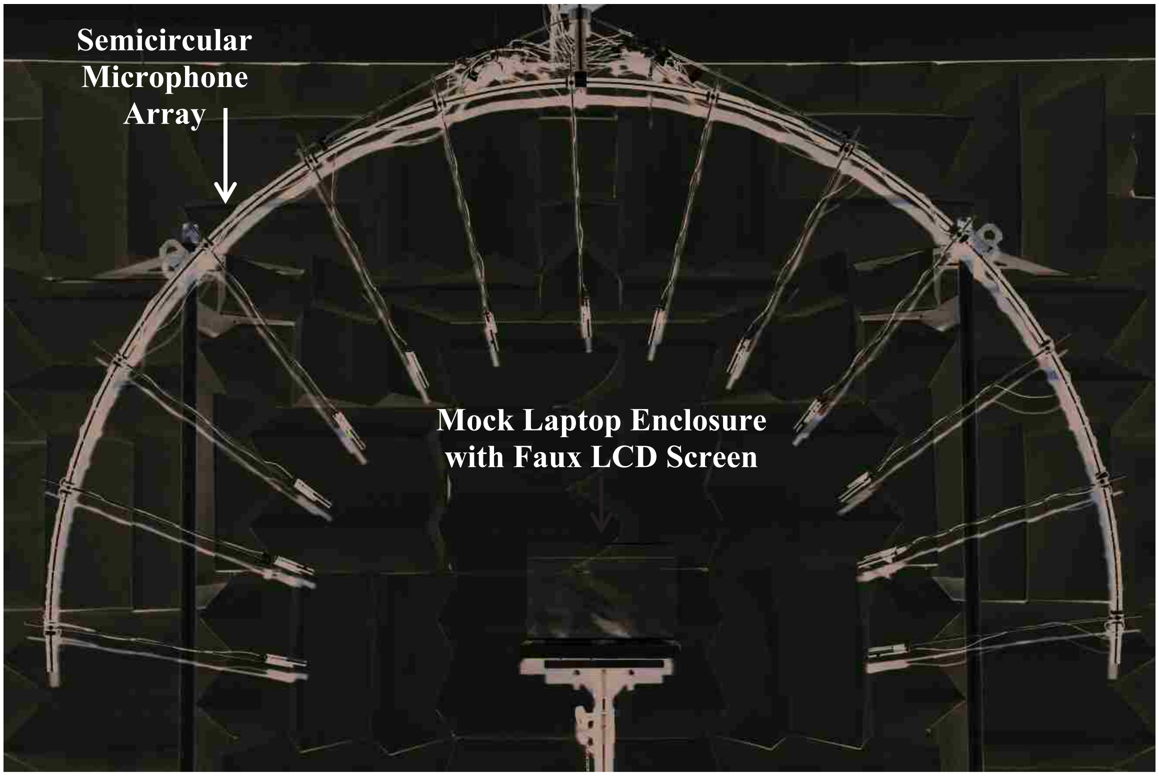

Figure 4-3 – Picture showing the mock laptop enclosure pictured in Fig. 4-2 placed beneath the semicircular array of microphones (56 cm radius).

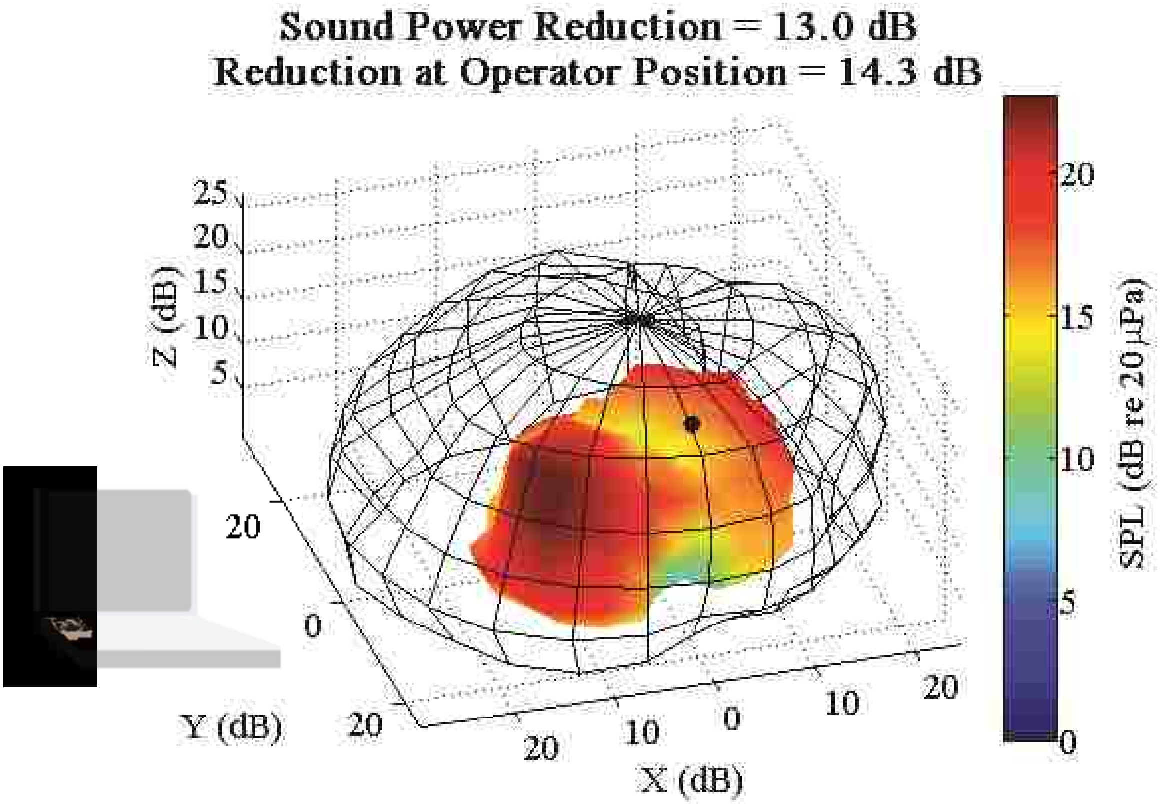

Figure 4-4 – Experimental result for control of the entire laptop when the two individual models are not coupled. The outer mesh is the uncontrolled sound field while the colored surface is the controlled sound field. The operator position direction is indicated by the black dot. The axis units and color scale are in dB re 20 μPa. The laptop enclosure is oriented as shown.

4.2 Coupled Model

The next step was to repeat the above experiment, but to assume the two models are coupled (*i.e.* the radiation from one affects the other and vice versa). To do this, we left the secondary sources and error sensors in the same locations, but operated both sets of secondary sources and error sensors as if they were one system. This was done experimentally by forcing the ANC algorithm to consider all secondary sources and error sensors simultaneously, rather than segregating the inlet and exhaust systems as was done previously. The results of this test are shown in Fig. 4-5. Note that there is an improvement (on the order of 2–3 dB) both in global power reduction and in pressure reduction at the operator position.

To ensure reproducibility, we repeated the control of the coupled system a number of times. The results for this series of tests are shown in Fig. 4-6. The red circles denote individual experiments, the black squares show the means for all experiments, while the error bars show the standard deviations. Note that though the mean reduction for both the power and the operator position pressure is approximately 16 dB, there is a standard deviation of approximately 1.5 dB, with outliers lying as far as 2.5 dB from the mean. This we attribute to small differences with the operating conditions of the laptop [*e.g.* slightly different screen angle (which was fixed at

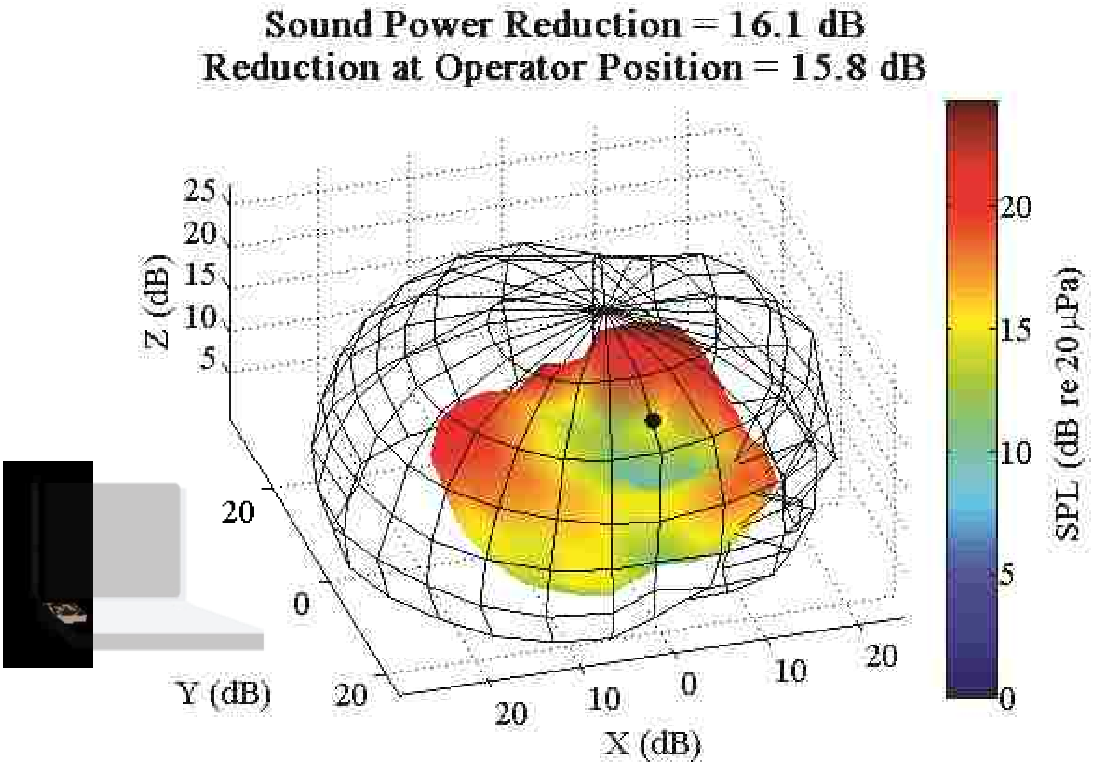

Figure 4-5 – Experimental result for control of the entire laptop when the two individuals models *are* coupled. The outer mesh is the uncontrolled sound field while the colored surface is the controlled sound field. The operator position direction is indicated by the black dot. The axis units and color scale are in dB re 20 μPa. The laptop enclosure is oriented as shown.

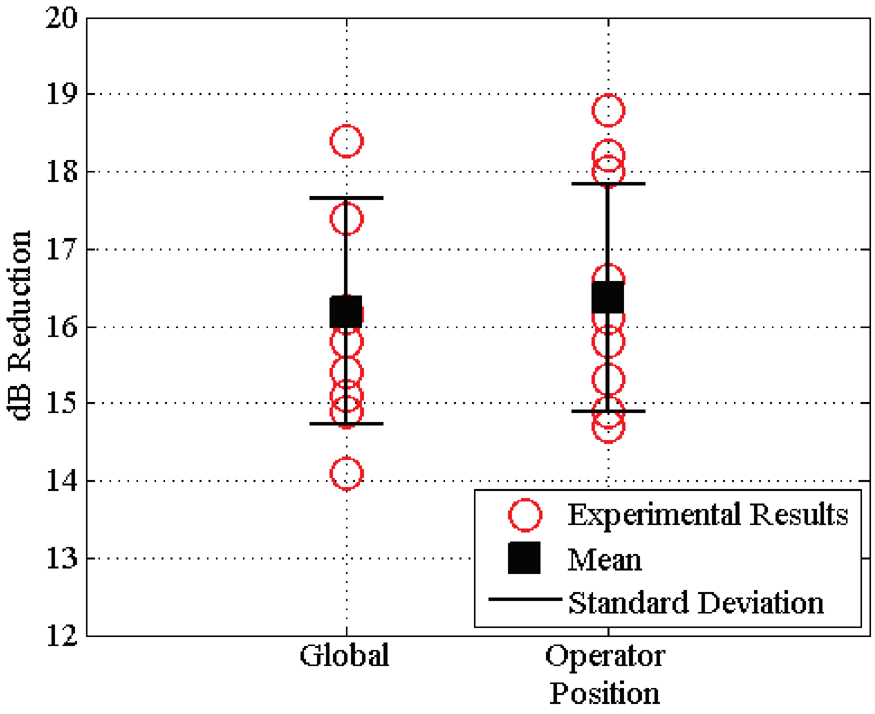

Figure 4-6 – Experimental results for control of the entire laptop when the two individuals models *are* coupled. The red circles denote individual experiments. The black squares show the means of the experimental results, while the error bars show the standard deviations. Both the results for global power reduction and operator position pressure reduction are shown. The y-axis units are in decibels.

nominally 115°), small changes in bottom clearance (which was fixed at nominally 4 mm), small changes in airflow (which depend on the bottom clearance), etc.].

We then varied the laptop screen angle and bottom clearances to see how the mean and standard deviation change. The screen angle was varied from 110° to 130°. The bottom clearances were varied from 4 mm to 1 cm, sometimes such that the laptop enclosure was level, sometimes not. The results of this study are shown in Fig. 4-7. Again, the red circles denote individual experiments, the black squares show the means for all experiments, while the error bars show the standard deviation. Note that while the mean reduction at the operator position remains nominally unchanged, the mean global power reduction drops by approximately 3 dB.

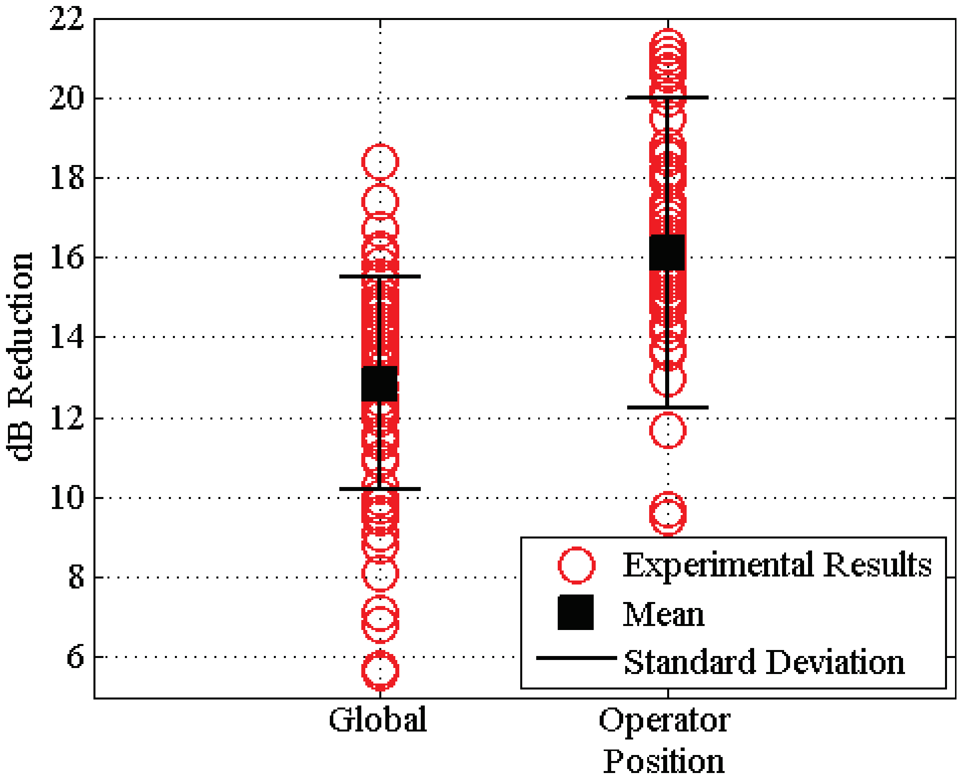

Figure 4-7 – Experimental results for control of the entire laptop when the laptop screen angle and bottom clearances are varied between tests. The red circles denote individual experiments. The black squares show the means of the experimental results, while the error bars show the standard deviation. Both the results for global power reduction and operator position pressure reduction are shown. The y-axis units are in decibels.

More importantly, the standard deviation for both the global power reduction and the pressure reduction at the operator position increases from 1.5 dB to 3 dB for power reduction and 4 dB for operator position reduction. Outliers lie as far as 8–9 dB away from the mean. This demonstrates that while on average the coupled model provides a good framework for implementation of an ANC system, changes in operating conditions often produce significantly varying results.

Notwithstanding their limitations, the models do an acceptable job at predicting good locations for ANC error sensors. Figure 4-8 shows the error sensor configuration used to test how drastically the amount of sound power reduction is reduced when the error sensors are

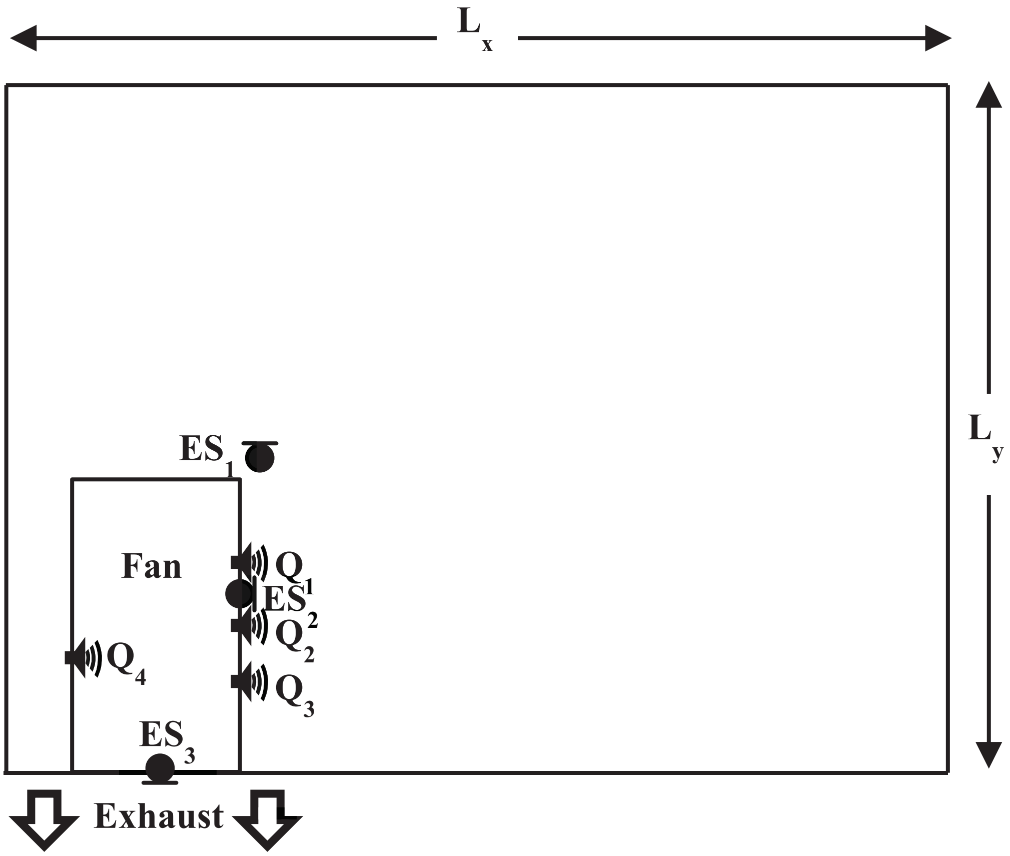

Figure 4-8 – Incorrect error sensor positions used to validate the combined model (compare with Fig. 4-1). The larger rectangle represents the enclosure itself while the smaller rectangle represents the fan and exhaust duct assembly. Secondary sources are placed as shown with source strengths Q_1, Q_2, Q_3, and Q_4, while error sensors are placed at locations ES_1, ES_2, and ES_3.

moved away from the predicted ideal locations. Figure 4-9 shows the results of this test. One notes the drastic reduction in performance—global power reduction reduces from 16 dB (as seen in Fig. 4-5) to 2.6 dB, while pressure reduction at the operator position decreases from 16 dB (again, as seen in Fig. 4-5) to 5.3 dB. This implies that even though the model needs improvement in order to account for changes in operating conditions, it does provide considerable guidance for implementing an ANC system with a small centrifugal fan mounted in a laptop enclosure.

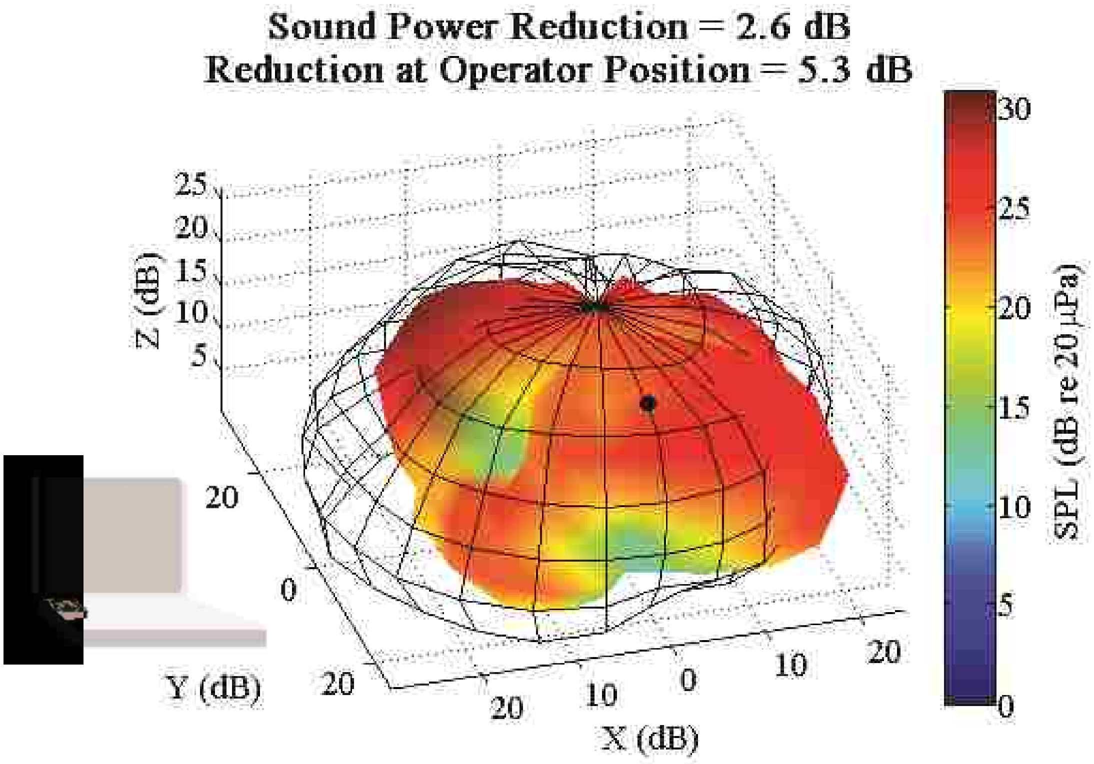

Figure 4-9 – Experimental result for control of the entire laptop when the model's recommendations are *not* followed. The outer mesh is the uncontrolled sound field while the colored surface is the controlled sound field. The operator position direction is indicated by the black dot. The axis units and color scale are in dB re 20 μPa. The laptop enclosure is oriented as shown.

Chapter 5

Conclusions

As stated in Sec. 1.1, noise from IT equipment is a significant problem in today's contemporary society.[1] From computers and projectors to printers and copiers, IT equipment noise permeates many facets of our everyday lives in a technology-driven world. Due to its prevalence, there is an intense interest in reducing, controlling, and eliminating IT noise in all of its many forms, including noise produced by fans of IT equipment.[2] This research has developed a model one may use to reduce the noise produced by laptop fans, thereby improving the quality of life for the user while enabling him/her to be more productive.

5.1 Results of Research

This research has developed two models meant to guide construction and implementation of an ANC system for a small centrifugal fan mounted in a rectangular laptop enclosure. The first model predicts and controls the noise propagating through the fan's exhaust, while the second model predicts and controls the noise propagating through the fan's inlets. Each model is experimentally verified both separately and then as a combined system.

First, the exhaust model is developed and tested. For the secondary source configuration shown in Fig. 2-5, the exhaust model recommends that one places an error sensor on the nodal line shown in Fig. 2-6. When this recommendation is followed, the actual power reduction mirrors the predicted values very closely when an ideal duct is used, as shown in Fig. 2-7. In addition, 11.7 dB global power reduction is achieved when the model is applied to a baffled centrifugal fan.

Second, the inlet model is developed and tested. For the secondary source configuration shown in Fig. 3-10, the inlet model recommends that we place error sensors on the nodal line shown in Fig. 3-11. When this recommendation is followed, the sound power is reduced by 12.5 dB while the pressure in the operator position direction is reduced by 18.7 dB, as seen in Fig. 3-12. However, when the model's recommendations are not followed, the sound power is amplified by 10.1 dB while the pressure in the operator position direction is reduced only marginally, by 0.6 dB as seen in Fig. 3-13.

Third, the exhaust and inlet models are combined. When the models are assumed to be independent, the sound power is reduced by 13 dB while the pressure at the operator position is reduced by 14.3 dB. However, when the models are assumed to be coupled, both the sound power and the pressure at the operator position are reduced by an average of 16 dB, with a standard deviation of approximately 1.5 dB. Furthermore, when the model's recommendations are not followed, the sound power is reduced by only 2.6 dB while the pressure at the operator position is reduced by only 5.3 dB.

5.2 Future Work

There are fundamental assumptions with the individual models that need to be addressed in order to create a truly robust model. First, the exhaust model assumes that the exhaust duct was mounted in an infinite baffle. This could be improved by assuming the exhaust duct instead radiated into free-space. If nodal line locations do not change dramatically, one can safely say that the nodal line positions when the exhaust duct is mounted in an enclosure will be similar to those predicted by the model.

Second, the inlet model assumes that radiation from the enclosure is uniform over the two boundaries at $x = 0$ and $x = L_x$ [see Eq. (3-24)]. In reality, the noise radiates from a collection of ports along these two boundaries. Thus, the model can be modified to take into account the cross-sectional area and position of these ports on these boundaries, which will improve the applicability of the model. It also assumes that there are no losses through the top or bottom plates, which ignores the presence of air vents that exist on the bottom of many laptops.

Third, and most importantly, the combined model assumes that the nodal line positions in one model are not affected by the other. These models must be coupled analytically, *i.e.* the secondary sources of one model must be included in the power minimization equation of the other and vice versa. It is possible that the predicted nodal lines may shift when this is done, leading to a more optimized solution.

If these improvements to the model are completed, it is expected that the control achieved by the test assembly may be increasingly repeatable and much less dependent on variations in operating conditions. This is because the model will more accurately reflect how the fan/enclosure system actually behaves.

5.3 Concluding Remarks

Centrifugal fans are ubiquitous in today’s society, especially when considering IT equipment noise. The average person in today’s modern world encounters several of these fans every single day. Because of their prevalence, their collective influence on one’s daily noise exposure should not be underestimated. These fans cannot be easily removed from everyday life due to the necessary role they fill in the modern workplace. This research has demonstrated a viable solution for controlling this noise using ANC. The hope is that because of this work, the quality of life for many people will improve without compromising their productivity in the workplace or elsewhere.[1]

Bibliography

1 G. W. Evans and D. Johnson, "Stress and open-office noise," J. Appl. Psych. **85**, 5 (2000).

2 G. C. Maling Jr., "Historical developments in the control of noise generated by small air-moving devices," Noise Con. Eng. J. **42** (5), 11 (1994).

3 P. A. Nelson and S. J. Elliott, *Active control of sound.* (Academic Press Limited, 1993).

4 K. L. Gee, *Multichannel active control of axial cooling fan noise,* MS Thesis, Brigham Young University, 2004.

5 K. L. Gee and S. D. Sommerfeldt, "Application of theoretical modeling to multichannel active control of cooling fan noise," J. Acoust. Soc. Am. **115**, 8 (2004).

6 K. L. Gee and S. D. Sommerfeldt, "A compact active control implementation for axial cooling fan noise," Noise Con. Eng. J. **51** (6), 325-334 (2003).

7 A. Gerard, A. Berry, P. Masson, and Y. Gervais, "Experimental validation of tonal noise control from subsonic axial fans using flow control obstructions," J. Sound Vib. **321**, 18 (2009).

8 A. Maaloum, "Effect of inlet duct contour and lack thereof on the noise generated of an axial flow fan," App. Acoust. **64** (10), 999-1010 (2003).

9 F. Orduna-Bustamente, A. Tavares-Mancillas, and R. d. l. Guardia-Gonzalez, "Enhancement by linear prediction of acoustic reference signals for active noise control of computer cooling fans," *Inter-Noise 2006* (Honolulu, Hawaii), *InterNoise Proc.*, **115**, p. 3548 (2006)

10 B. M. Shafer, K. L. Gee, and S. D. Sommerfeldt, "Verification of a near-field error sensor placement method in active control of compact noise sources," J. Acoust. Soc. Am. **127** (2), EL66 (2010).

11 T. F. W. Embleton, "Experimental study of noise reduction in centrifugal blowers," J. Acoust. Soc. Am. **35** (5), 700-705 (1963).

12 E. Baugh, "Acoustic limitations in notebook thermal design," *10th Electronics Packaging Technology Conference, 2008.* (Singapore), *IEEE Conference Publications*, p. 725-730 (2008)

13 G. H. Koopmann, D. J. Fox, and W. Nezse, "Active source cancellation of the blade tone fundamental and harmonics in centrifugal fans," J. Sound Vib. **126** (2), 11 (1988).

14 G. H. Koopmann, W. Neise, and W. Chen, "Active noise control to reduce the blade tone noise of centrifugal fans," J. Vib. Acoust. Stress Rel. Des. **110**, 7 (1988).

15 J. Wu, "Application of feedforward adaptive active-noise control for reducing blade passing noise in centrifugal fans," J. Sound Vib. **239** (5), 1051-1062 (2001).

16 D. Wolfram and T. H. Carolus, "Experimental and numerical investigation of the unsteady flow field and tone generation in an isolated centrifugal fan impeller," J. Sound Vib. **329** (21), 4380-4397 (2010).

[17] W. Neise, "Noise reduction in centrifugal fans: A literature survey," J. Sound Vib. **45** (3), 375-403 (1976).

[18] W. Neise and G. H. Koopmann, "Reduction of centrifugal fan noise by use of resonators," J. Sound Vib. **73** (2), 297-308 (1980).

[19] H. A. Cordourier-Maruri and F. Orduna-Bustamente, "Active control of periodic fan noise in laptops: Spectral width requirements in a delayed buffer implementation," J. Appl. Res. Tech. **7** (2), 124-135 (2009).

[20] H. Cordourier-Maruri and F. Orduna-Bustamante, "Multichannel active control of tonal fan noise in laptops," J. Acoust. Soc. Am. **128** (4), 2286 (2010).

[21] J. A. Kemp, D. M. Campbell, and N. Amir, "Multimodal radiation impedance of a rectangular duct terminated in an infinite baffle," Acta Acustica **87**, 5 (2001).

[22] A. D. Pierce, R. O. Cleveland, and M. Zampolli, "Radiation impedance matrices for rectangular interfaces within rigid baffles: Calculation methodology and applications," J. Acoust. Soc. Am. **111** (2), 672 (2002).

[23] L. Burian and P. Fuchs, "A simple active noise control in acoustic duct," *Proceedings on the 2005 European Conference on Circuit Theory and Design* **3**, p. 265-268 (2005)

[24] J. K. Boyle, *Active noise control of a small, baffled centrifugal fan,* Capstone Report, Brigham Young University, 2012.

[25] G. B. Arfken and H. J. Weber, *Mathematical methods for physicists*, 6th ed. (Elseveir, 2005).

[26] A. D. Pierce, *Acoustics: An introduction to its physical principles and applications*, 1994 ed. (Acoustical Society of America, Melville, 1989).

Appendices

The appendices contain a detailed investigation into pressure-particle velocity modal coupling patterns, a comparison between the two-dimensional and three-dimensional free-space models, and the MATLAB code constructed for each of the analytic models mentioned in this study. Appendix A investigates the pressure-particle velocity modal coupling patterns that are a consequence of the multimodal radiation impedance matrix, developed in Ref. [21] and described in Sec. 2.2. Appendix B compares the 2-d free-space model developed in Sec. 3.1. to the common 3-d free-space model contained in Nelson and Elliott.[3] Appendix C contains the MATLAB codes designed for all models. Section C.1 covers the code used for the point source in a finite-length duct model, explained in Chap. 2. Section C.2 contains the code used to calculate the multimodal radiation impedance for the finite-length duct model, described in Sec. 2.2. Section C.3 holds the code made for the two-dimensional free-space model, found in Sec. 3.1. Section C.4 shows the code used for the two-dimensional modal model, explained in Sec. 3.2.

Appendix A
Analysis of the Multimodal Radiation Impedance Matrix

In order to more fully understand which pressure modes couple with which particle velocity modes and why, a radiation impedance matrix containing the first eight modes of the rectangular duct is computed, akin to Fig. 2-4. These results are shown in Fig. A-1. Notice how

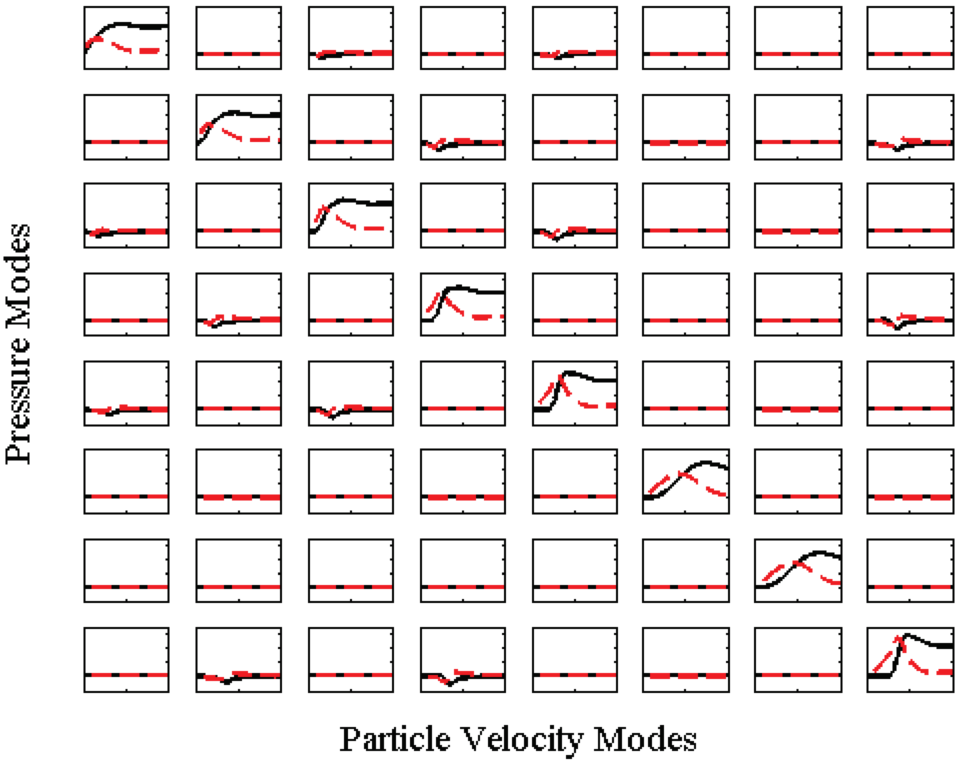

Figure A-1 – 8x8 radiation impedance matrix for the duct used in this study. Note how there is no coupling between the 6th or 7th mode and any other mode (*i.e.* the entries in the 6th and 7th rows are all zero except the entries that lie on the main diagonal of the matrix). The x-axes units for each entry are the dimensionless quantity $k\sqrt{S}$, where k is the wavenumber and S is the cross-sectional area of the duct. The y-axes units for each entry are normalized impedance magnitude.

after a certain number of modes are included, the assertion that even modes couple exclusively with even modes and odd modes couple exclusively with odd modes can no longer be made.

The reason that this pattern no longer holds is because of the different types of cross modes in the duct. In any two-dimensional space (like the cross-section of a duct) there are two types of modes: axial and tangential. Axial modes are those modes whose pressure and particle velocity are functions of only one dimension. For a rectangular duct, there exist axial modes for both the x and y dimensions. Tangential modes are those modes whose pressure and particle velocity are functions of two dimensions.

Because three different types of modes exist in the duct, four different types of coupling need to be considered. First, coupling between axial modes in one dimension and axial modes in the same dimension must be considered. Second, coupling between axial modes in one dimension and axial modes in the other dimension must be explored. Third, coupling between tangential modes and tangential modes must be studied. Fourth, coupling between axial modes and tangential modes must be investigated.

For these studies, a large number of modes must be analyzed. Due to the size of the data set, this does not lend itself to a figure like unto Fig. A-1. In place of a figure, a radiation impedance table will be used. Each entry will show whether coupling occurs between its respective pressure and particle velocity mode. For example, Table A-1 shows the data contained in Fig. A-1—there is strong coupling along the main diagonal of the matrix, and weak coupling in other places. In this table, p_m denotes the mth pressure mode, u_n denotes the nth particle velocity mode, S denotes strong coupling $\left(\max\left|\Re\left\{\frac{Z_{rad_{m,n}}}{\rho_0 c}\right\}\right| > 1\right)$, W denotes weak coupling $\left(\max\left|\Re\left\{\frac{Z_{rad_{m,n}}}{\rho_0 c}\right\}\right| < 1\right)$, and an empty cell denotes no coupling $\left(\Re\left\{\frac{Z_{rad_{m,n}}}{\rho_0 c}\right\} = 0\right)$. All radiation impedances are normalized by $\rho_0 c$ for ease of comparison.

u_n p_m	1	2	3	4	5	6	7	8
1	S		W		W			
2		S		W				W
3	W		S		W			
4		W		S				W
5	W		W		S			
6						S		
7							S	
8		W		W				S

Table A-1 – Table which shows the presence of coupling between the first eight modes of the rectangular duct used in this study, as seen in Fig. A-1. p_m denotes the m^{th} pressure mode, while u_n denotes the n^{th} particle velocity mode. S denotes strong coupling $\left(\max\left|\Re\left\{\frac{Z_{rad_{m,n}}}{\rho_0 c}\right\}\right| > 1\right)$, W denotes weak coupling $\left(\max\left|\Re\left\{\frac{Z_{rad_{m,n}}}{\rho_0 c}\right\}\right| < 1\right)$, and an empty cell denotes no coupling $\left(\Re\left\{\frac{Z_{rad_{m,n}}}{\rho_0 c}\right\} = 0\right)$.

A.1 Coupling of Axial Modes in One Dimension to Axial Modes in the Same Dimension

The first type of coupling to be considered is axial modes in one dimension coupling to other axial modes in the same dimension. To this end, an analysis is conducted on a hypothetical duct with an aspect ratio $\frac{L_y}{L_x} = 0.95$. This ensures that modes in both dimensions happen regularly but avoids degenerate modes. The plane wave mode and the first eight axial modes in one dimension are considered and radiation impedance matrices are constructed. Table A-2 shows the results of this study. In this table, p_m denotes the m^{th} pressure mode, u_n denotes the n^{th} particle velocity mode. PW denotes the plane wave mode and x_n denotes the n^{th} axial mode in the x dimension. As before, S denotes strong coupling $\left(\max\left|\Re\left\{\frac{Z_{rad_{m,n}}}{\rho_0 c}\right\}\right| > 1\right)$, W denotes weak coupling $\left(\max\left|\Re\left\{\frac{Z_{rad_{m,n}}}{\rho_0 c}\right\}\right| < 1\right)$, and an empty cell denotes no coupling $\left(\Re\left\{\frac{Z_{rad_{m,n}}}{\rho_0 c}\right\} = 0\right)$.

u_n p_m	PW	x_1	x_2	x_3	x_4	x_5	x_6	x_7	x_8
PW	S		W		W		W		W
x_1		S		W		W		W	
x_2	W		S		W		W		W
x_3		W		S		W		W	
x_4	W		W		S		W		W
x_5		W		W		S		W	
x_6	W		W		W		S		W
x_7		W		W		W		S	
x_8	W		W		W		W		S

Table A-2 – Table which shows the presence of coupling between the plane wave mode and the first eight axial modes in one dimension for the hypothetical duct. p_m denotes the m^{th} pressure mode, while u_n denotes the n^{th} particle velocity mode. PW denotes the plane wave mode and x_n denotes the n^{th} axial mode in the x dimension. S denotes strong coupling $\left(\max\left|\Re\left\{\frac{Z_{rad_{m,n}}}{\rho_0 c}\right\}\right| > 1\right)$, W denotes weak coupling $\left(\max\left|\Re\left\{\frac{Z_{rad_{m,n}}}{\rho_0 c}\right\}\right| < 1\right)$, and an empty cell denotes no coupling $\left(\Re\left\{\frac{Z_{rad_{m,n}}}{\rho_0 c}\right\} = 0\right)$.

Note that the same trend observed in Sec. 2.2 is shown here. Thus, when axial modes along one dimension are considered, even pressure modes couple with even particle velocity modes, while odd pressure modes couple with odd particle velocity modes. However, even pressure modes do not couple with odd particle velocity modes and vice versa. In short, if two axial modes in the same dimension couple with each other, their modal numbers must have the same parity.

A.2 Coupling of Axial Modes in One Dimension to Axial Modes in a Different Dimension

The next type of coupling to be explored is axial modes in one dimension coupling to other axial modes in another dimension (*i.e.* coupling axial modes in the x direction to axial modes in the y direction). To this end, an analysis is conducted on the same hypothetical duct as before. The plane wave mode and the first eight axial modes in both dimensions are considered and radiation impedance matrices are constructed. Entries where modal coupling occurs are identified. Table A-3 shows the results of this study. In this table, x_n denotes the n^{th} axial mode in the x dimension, y denotes the n^{th} axial mode in the y dimension, W denotes weak coupling $\left(0.1 < \max\left|\Re\left\{\frac{Z_{rad_{m,n}}}{\rho_0 c}\right\}\right| < 1\right)$, and w denotes very weak coupling $\left(0 < \max\left|\Re\left\{\frac{Z_{rad_{m,n}}}{\rho_0 c}\right\}\right| < 0.1\right)$. All other variables are as defined previously.

This tells us that even axial modes in one dimension only couple to even axial modes in another dimension. Odd axial modes in one dimension do not couple to any modes in another dimension. Furthermore, the higher the order of the even axial mode, the less significantly it couples with other unlike even axial modes. For example, the x_4 pressure mode couples weakly to the y_4 particle velocity mode and very weakly to the y_8 particle velocity mode, but the x_3 pressure mode does not couple to any axial mode in y.

u_n p_m	PW	x_1	x_2	x_3	x_4	x_5	x_6	x_7	x_8	y_1	y_2	y_3	y_4	y_5	y_6	y_7	y_8
PW	S		W		W		W		W		W		W		W		W
x_1		S		W		W		W									
x_2	W		S		W		W		W		W		W		W		w
x_3		W		S		W		W									
x_4	W		W		S		W		W		W		W		w		w
x_5		W		W		S		W									
x_6	W		W		W		S		W		W		W		w		w
x_7		W		W		W		S									
x_8	W		W		W		W		S		w		w		w		w
y_1										S		W		W		W	
y_2	W		W		W		W		w		S		W		W		W
y_3										W		S		W		W	
y_4	W		W		W		W		w		W		S		W		W
y_5										W		W		S		W	
y_6	W		W		w		w		w		W		W		S		W
y_7										W		W		W		S	
y_8	W		w		w		w		w		W		W		W		S

Table A-3 – Table which shows the presence of coupling between the plane wave mode and the first eight axial modes in both dimensions for the hypothetical duct. p_m denotes the m^{th} pressure mode, u_n denotes the n^{th} particle velocity mode. PW denotes the plane wave mode, x_n denotes the n^{th} axial mode in the x dimension, and y_n denotes the n^{th} axial mode in the y dimension. S denotes strong coupling $\left(\max\left|\Re\left\{\frac{Z_{rad_{m,n}}}{\rho_0 c}\right\}\right| > 1\right)$, W denotes weak coupling $\left(0.1 < \max\left|\Re\left\{\frac{Z_{rad_{m,n}}}{\rho_0 c}\right\}\right| < 1\right)$, w denotes very weak coupling $\left(0 < \max\left|\Re\left\{\frac{Z_{rad_{m,n}}}{\rho_0 c}\right\}\right| < 0.1\right)$, and an empty cell denotes no coupling $\left(\Re\left\{\frac{Z_{rad_{m,n}}}{\rho_0 c}\right\} = 0\right)$.

A.3 Coupling of Tangential Modes to Other Tangential Modes

The third type of coupling to be studied is tangential modes coupling to other tangential modes. To this end, an analysis is conducted on the hypothetical duct mentioned previously. The first sixteen tangential modes are considered and radiation impedance matrices are constructed. Entries where modal coupling occurs are identified. Table A-4 shows the results of this study. In this table, $x_m y_n$ denotes the tangential mode that is the superposition of the mth axial mode in x and the nth axial mode in y. All other variables are as defined previously.

Observe that tangential modes follow a version of the even-even and odd-odd coupling manifested before. In this case, however, the parity of the x components must match and the parity of the y components must match. If they do not, no coupling occurs (*e.g.* the $x_2 y_2$ pressure mode couples with the $x_4 y_4$ particle velocity mode, but not with the $x_2 y_3$ mode nor with the $x_1 y_2$ mode). In short, in order for two tangential modes to couple, both their parity in the x dimension and their parity in the y dimension must match.

u_n p_m	x_1 y_1	x_2 y_1	x_3 y_1	x_4 y_1	x_1 y_2	x_2 y_2	x_3 y_2	x_4 y_2	x_1 y_3	x_2 y_3	x_3 y_3	x_4 y_3	x_1 y_4	x_2 y_4	x_3 y_4	x_4 y_4
$x_1 y_1$	S		W						W		W					
$x_2 y_1$		S		W						W		W				
$x_3 y_1$	W		S						W		W					
$x_4 y_1$		W		S						W		W				
$x_1 y_2$					S		W						W		W	
$x_2 y_2$						S		W						W		W
$x_3 y_2$					W		S						W		W	
$x_4 y_2$						W		S						W		W
$x_1 y_3$	W		W						S		W					
$x_2 y_3$		W		W						S		W				
$x_3 y_3$	W		W						W		S					
$x_4 y_3$		W		W						W		S				
$x_1 y_4$					W		W						S		W	
$x_2 y_4$						W		W						S		W
$x_3 y_4$					W		W						W		S	
$x_4 y_4$						W		W						W		S

Table A-4 – Table which shows the presence of coupling between the first sixteen tangential modes for the hypothetical duct. $x_m y_n$ denotes the tangential mode that is the superposition of the m^{th} axial mode in x and the n^{th} axial mode in y. p_m denotes the m^{th} pressure mode, while u_n denotes the n^{th} particle velocity mode. S denotes strong coupling $\left(\max\left|\Re\left\{\frac{Z_{rad_{m,n}}}{\rho_0 c}\right\}\right| > 1\right)$, W denotes weak coupling $\left(\max\left|\Re\left\{\frac{Z_{rad_{m,n}}}{\rho_0 c}\right\}\right| < 1\right)$, and an empty cell denotes no coupling $\left(\Re\left\{\frac{Z_{rad_{m,n}}}{\rho_0 c}\right\} = 0\right)$.

A.4 Coupling of Axial Modes to Tangential Modes

The final type of coupling to be investigated is axial modes coupling to tangential modes. To this end, an analysis is conducted on the same hypothetical duct as before. The plane wave mode, first four axial modes in each dimension, and the first sixteen tangential modes are considered and radiation impedance matrices are constructed. Entries where modal coupling occurs are identified. Table A-5 shows the results of this study. All variables are as defined previously.

Note that Table A-5 only includes the tangential pressure modes, and the plane wave and axial particle velocity modes. Because of the largeness of the data set, it is not feasible to place the entire table in this document. Thus, only the part dealing with axial-tangential coupling was included. Since the radiation impedance matrix is symmetric, Table A-5 also applies to coupling between plane wave and axial pressure modes with tangential particle velocity modes.

There are three observations to be drawn from Table A-5. First, the plane wave mode and even axial modes only couple with tangential modes with even mode components (*e.g.* the x_2 mode couples with the x_4y_4 tangential mode, but not with the x_2y_1 mode, nor the x_3y_4 mode). Second, odd axial modes only couple with tangential modes whose like-dimension component has the same parity, but unlike-dimension component has different parity (*e.g.* the y_3 axial mode couples with the x_2y_1 tangential mode, but not with the x_3y_3 mode, nor with the x_2y_2 mode). Third, very weak coupling is observed when the above conditions are met, but the tangential mode components are further removed from the axial mode components.

u_n p_m	PW	x_1	x_2	x_3	x_4	y_1	y_2	y_3	y_4
x_1y_1									
x_2y_1						W		W	
x_3y_1									
x_4y_1						W		w	
x_1y_2		W		W					
x_2y_2	W		W		W		W		W
x_3y_2		W		W					
x_4y_2	w		W		W		W		w
x_1y_3									
x_2y_3						W		W	
x_3y_3									
x_4y_3						w		W	
x_1y_4		W		w					
x_2y_4	w		W		w		W		W
x_3y_4		w		W					
x_4y_4	w		w		W		w		W

Table A-5 – Table which shows the presence of coupling between the plane wave mode, the first four axial modes in both dimensions, and the first sixteen tangential modes for the hypothetical duct. PW denotes the plane wave mode, x_n denotes the n^{th} axial mode in the x dimension, and y_n denotes the n^{th} axial mode in the y dimension. $x_m y_n$ denotes the tangential mode that is the superposition of the m^{th} axial mode in x and the n^{th} axial mode in y, p_m denotes the m^{th} pressure mode, and u_n denotes the n^{th} particle velocity mode. W denotes weak coupling $\left(0.1 < \max\left|\Re\left\{\frac{Z_{rad_{m,n}}}{\rho_0 c}\right\}\right| < 1\right)$, w denotes very weak coupling $\left(0 < \max\left|\Re\left\{\frac{Z_{rad_{m,n}}}{\rho_0 c}\right\}\right| < 0.1\right)$, and an empty cell denotes no coupling $\left(\Re\left\{\frac{Z_{rad_{m,n}}}{\rho_0 c}\right\} = 0\right)$.

A.5 Application to Rectangular Duct

When put together, the four types of coupling developed in this Appendix are able to explain the modal coupling behavior exhibited in Table A-1. The first mode is the plane wave mode. Modes 2-5 are the first four axial modes in x (x_1–x_4). Mode 6 is the first axial mode in y (y_1), mode 7 is the x_1y_1 tangential mode, while mode 8 is the fifth axial mode in x (x_5). Note how modes 1-5 and mode 8 follow the rules for the first type of axial coupling described in Sec. A.1. Mode 6 follows the rules developed in Sec. A.2 for unlike dimension axial mode coupling, while mode 7 follows the rules for axial-tangential coupling developed in Sec. A.4. Thus the coupling between all of the modes included in the exhaust model used in this study can be explained in terms of the general rules developed here.

Appendix B
Comparison between 2-d and 3-d Free-Space Models

In order to understand more fully the two-dimensional free space, it is useful to compare it to the three-dimensional free space model found in Nelson and Elliott.[3] They state that for a single secondary source a distance d away from the primary source, the optimum source strength is given by

$$Q_{sO} = -Q_p \frac{\sin(kd)}{kd}, \tag{B-1}$$

where Q_{sO} is the optimum source strength, Q_p is the primary source strength, and k is the wavenumber. Furthermore, the minimum power output from such a system is given by

$$\Pi_{min} = \Pi_p \left(1 - \left[\frac{\sin(kd)}{kd}\right]^2\right), \tag{B-2}$$

where Π_{min} is the minimized power and Π_p is the power output by the primary source alone. For details, see Sec. 8.4 in Ref. [3].

In order to make a correct comparison, it is necessary to begin with Eq. (3-12) and assume a single secondary source a distance d away from the primary source. When Eq. (3-13) is substituted into this simplified version of Eq. 3-12, this leads to

$$\Pi = -\frac{\rho_0 ck}{8}\left[\left|Q_p\right|^2 + 2Q_pQ_s J_0(kd) + |Q_s|^2\right], \tag{B-3}$$

where ρ_0 is the ambient density of air, c is the speed of sound in air, k is the wavenumber, Q_p is the primary source strength, Q_s is the secondary source strength, and J_0 is the zeroth-order Bessel function.

Following the process of Sec. 3.1, the derivative of Eq. (B-3) is taken with respect to Q_s and set it equal to zero in order to minimize the power radiated from the system. This leads to

$$\frac{\partial \Pi}{\partial Q_s} = -\frac{\rho_0 ck}{8}\left[2Q_p J_0(kd) + 2Q_s\right] = 0 \Longrightarrow$$

$$Q_{sO} = -Q_p J_0(kd), \tag{B-4}$$

where Q_{sO} is the optimum secondary source strength needed to minimize the overall radiated power. Note how the factor multiplying Q_p differs from that shown in Eq. (B-1). A graphical comparison is shown in Fig. B-1.

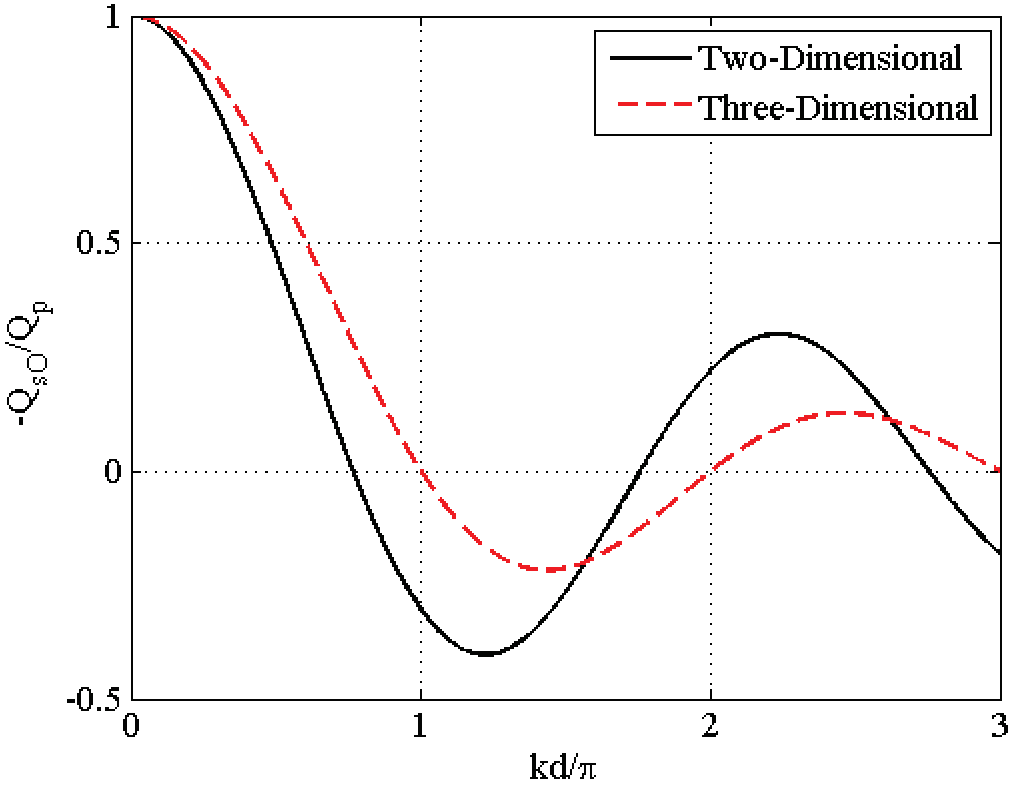

Figure B-1 – Figure comparing the optimum secondary source strength for a single primary/secondary source pair in a 2-d and 3-d free-space.

Equation (B-4) is then substituted into Eq. (A-3) to find the minimum power output, which is given by

$$\Pi_{min} = \Pi_p[1 - J_0^2(kd)], \tag{B-5}$$

where Π_{min} is the minimum power output of the system. Again, note how the term multiplying Π_p has changed. A graphical comparison is shown in Fig. B-2.

Some general conclusions can be drawn from this simple comparison. First, though the general forms for the optimum secondary source strength and the minimum power output for a single primary/secondary source pair is the same for the two-dimensional and three-dimensional models, there are significant differences between the two models. In both cases, a Bessel

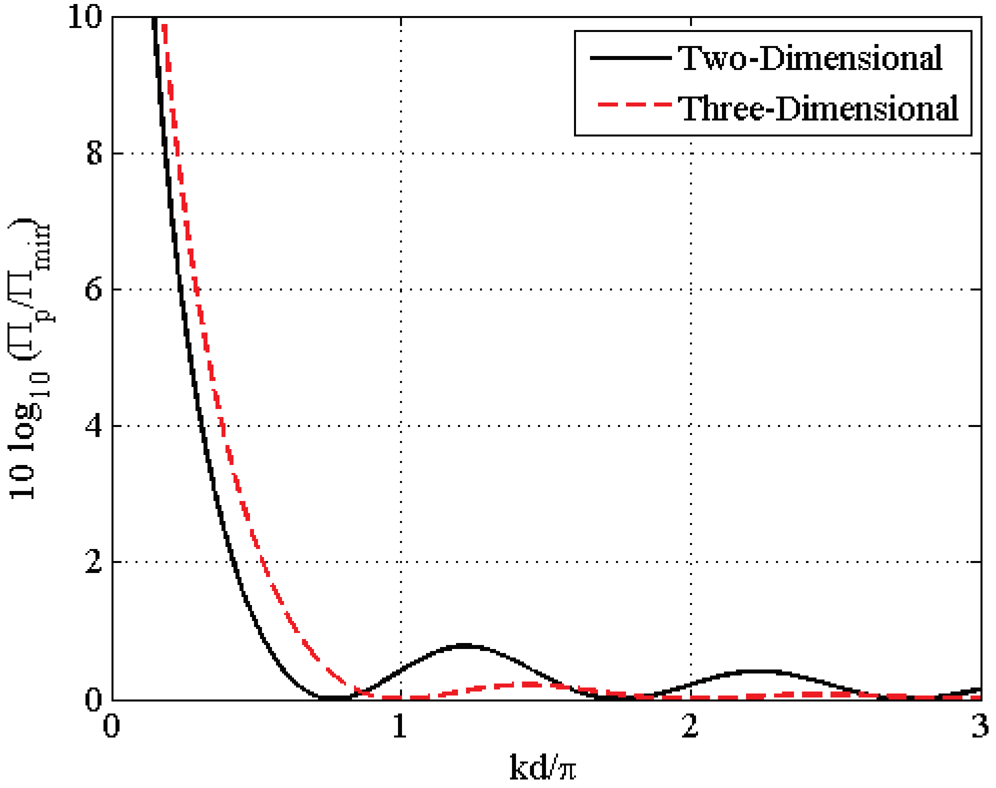

Figure B-2 – Figure comparing the minimum power output for a single primary/secondary source pair in a 2-d and 3-d free-space.

function is substituted for a decaying sinusoid. Second, lower values of kd are required in order to obtain appreciable power reduction, as seen in Fig. A-2. This means that secondary sources must be placed closer to primary sources in a two-dimensional environment in order to adequately couple. Both of these conclusions are the result of the cylindrical spreading that occurs in a two-dimensional free-space, as opposed to the spherical spreading that occurs in a three-dimensional space.

Appendix C
MATLAB Code

C.1 Exhaust Model MATLAB Code

```
%% Point Source in a Finite Duct Model
% James Esplin
% 8/7/10

clc;
close all;
clear all;

matlabpool close force local
matlabpool

tic

% Set Physical Constants

c = 343; % Speed of Sound
p0 = 1.21; % Density of Air

% Here are the dimensions of the duct and the locations of the primary
% and secondary sources.

Lx = .048;
Ly = .01;
Lz = .1;

xP1 = Lx;
yP1 = Ly/2;
zP1 = .0575;

xC1 = Lx;
yC1 = Ly/2;
zC1 = .0625;

%  Here  are  the  variables  over  the  range  of  the  duct  and  frequency
% range.

x = 0:.001:Lx;
y = 0:.001:Ly;
z = 0:.001:Lz;

f = linspace(500,2000,1501);
frange = [500,2000];

% Now we define the number of modes to include in the model and load
% the precomputed multimodal radiation impedance matrix.

nummodes = 8;
```

```
load(['Zrad\Zrad_',num2str(min(f)),'_',num2str(length(f)),'_',...
      num2str(max(f)),'_8_modes']);
clear Zerror;
if exist('frange','var')
    f = f(frange(1):frange(2));
    for m = 1:nummodes
        for n = 1:nummodes
            Zrad{m,n} = Zrad{m,n}(frange(1):frange(2));
        end
    end
end

% Now we calculate the lowest eight modes of the duct given the
% cross-sectional area.

fres = zeros(nummodes);
for m = 0:nummodes-1;
    for n = 0:nummodes-1;
        fres(m+1,n+1) = c/2*sqrt((m/Lx)^2+(n/Ly)^2);
    end
end
clear l m n;


[temp,fresind] = sort(fres(:));
[fresr,fresc] = ind2sub([nummodes,nummodes],fresind);
clear fresind fres temp;
fresr = fresr(1:nummodes);
fresc = fresc(1:nummodes);
fresr = fresr-1;
fresc = fresc-1;

% We now truncate Zrad to include only the number of modes we wish to
% include in the model.

Zrad = Zrad(1:nummodes,1:nummodes);

% We now define our wavenumber, modal wavenumber, and the assumed
% source strength of the primary source.

k = 2*pi*f/c;

kn = zeros(nummodes,1);
kz = zeros(length(k),nummodes);

Q0 = 1;

%% Coefficient Calculation

% Now I calculate the coefficients to the z-dimension eigenfunction, as
% given by Eqs. (2-23) and (2-24).

Lambda = zeros(1,nummodes);
F0 = zeros(length(z),length(k),nummodes);
F1 = zeros(length(z),length(k),nummodes);
Psi = zeros(length(x),length(y),nummodes);
Psi0 = zeros(nummodes,1);
```

```
Psi1 = zeros(nummodes,1);
Ans0 = zeros(2*nummodes,1);
Ans1 = zeros(2*nummodes,1);
R10 = cell(nummodes);
S10 = cell(nummodes);
R0temp = R10;
S0temp = S10;
R0temp{1,1} = zeros(length(k),1);
R0temp(1:end,1:end) = R0temp(1,1);
S0temp{1,1} = zeros(length(k),1);
S0temp(1:end,1:end) = S0temp(1,1);
R20 = R0temp;
S20 = S0temp;
AB0 = zeros(nummodes*2,length(k));
R11 = cell(nummodes);
S11 = cell(nummodes);
R1temp = R11;
S1temp = S11;
R1temp{1,1} = zeros(length(k),1);
R1temp(1:end,1:end) = R1temp(1,1);
S1temp{1,1} = zeros(length(k),1);
S1temp(1:end,1:end) = S1temp(1,1);
R21 = R1temp;
S21 = S1temp;
AB1 = zeros(nummodes*2,length(k));
for indmode = 1:nummodes

    m = fresr(indmode);
    n = fresc(indmode);

    % First we start by calculating k and kz.
    kn(indmode) = sqrt((m*pi/Lx)^2+(n*pi/Ly)^2);
    kz(:,indmode) = sqrt(k.^2-kn(indmode).^2);

    % Next, we make kz complex to account for damping.
    for indkz = 1:length(k)
        kz(indkz,indmode) = real(kz(indkz,indmode))...
            -1i*abs(imag(kz(indkz,indmode)));
    end

    % Now we calculate the cross-modes.
    Psi(:,:,indmode) = cos(m*pi/Lx*x).'*cos(n*pi/Ly*y);
    Psi0(indmode,:) = cos(m*pi/Lx*xP1).*cos(n*pi/Ly*yP1);
    Psi1(indmode,:) = cos(m*pi/Lx*xC1).*cos(n*pi/Ly*yC1);

    % Next we calculate the scaling factor based on the mode number.

    if m == 0 && n == 0
        Lambda(indmode) = 1;
    elseif m == 0 && n > 0
        Lambda(indmode) = 1/2;
    elseif m > 0 && n == 0
        Lambda(indmode) = 1/2;
    else
        Lambda(indmode) = 1/4;
    end

```

```
    % Now we begin to assemble the components to the R and S matrices,
    % as seen in Eqs. (2-23b) and (2-24a).

        R10{1,indmode} = ...
            -kz(:,indmode).*exp(-1i*kz(:,indmode)*(Lz-zP1));
        R20{indmode,indmode} = ...
            (-1i+tan(kz(:,indmode)*zP1)).*kz(:,indmode);

        S10{1,indmode} = kz(:,indmode).*exp(1i*kz(:,indmode)*(Lz-zP1));
        S20{indmode,indmode} = ...
            (1i+tan(kz(:,indmode)*zP1)).*kz(:,indmode);

        R10(2:nummodes,indmode) = R10(1,indmode);
        S10(2:nummodes,indmode) = S10(1,indmode);

        R0temp{indmode,indmode} = ...
            p0*c*k.'.*exp(-1i*kz(:,indmode)*(Lz-zP1));
        S0temp{indmode,indmode} = ...
            p0*c*k.'.*exp(1i*kz(:,indmode)*(Lz-zP1));

        R11{1,indmode} = ...
            -kz(:,indmode).*exp(-1i*kz(:,indmode)*(Lz-zC1));
        R21{indmode,indmode} = ...
            (-1i+tan(kz(:,indmode)*zC1)).*kz(:,indmode);

        S11{1,indmode} = kz(:,indmode).*exp(1i*kz(:,indmode)*(Lz-zC1));
        S21{indmode,indmode} = ...
            (1i+tan(kz(:,indmode)*zC1)).*kz(:,indmode);

        R11(2:nummodes,indmode) = R11(1,indmode);
        S11(2:nummodes,indmode) = S11(1,indmode);

        R1temp{indmode,indmode} = ...
            p0*c*k.'.*exp(-1i*kz(:,indmode)*(Lz-zC1));
        S1temp{indmode,indmode} = ...
            p0*c*k.'.*exp(1i*kz(:,indmode)*(Lz-zC1));

    % Now we assemble the answer vector.
    Ans0(indmode+nummodes) = -Psi0(indmode)/Lx/Ly/Lambda(indmode);
    Ans1(indmode+nummodes) = -Psi1(indmode)/Lx/Ly/Lambda(indmode);
end

% Now we set up the matrices that are multiplied by our A2 and B2
% coefficients.

if iscell(Zrad)
    R10 = cellfun(@(x,y)x.*y,R10,Zrad,'uni',0);
    S10 = cellfun(@(x,y)x.*y,S10,Zrad,'uni',0);
    R11 = cellfun(@(x,y)x.*y,R11,Zrad,'uni',0);
    S11 = cellfun(@(x,y)x.*y,S11,Zrad,'uni',0);
else
    R10 = cellfun(@(x)x*Zrad,R10,'uni',0);
    S10 = cellfun(@(x)x*Zrad,S10,'uni',0);
    R11 = cellfun(@(x)x*Zrad,R11,'uni',0);
    S11 = cellfun(@(x)x*Zrad,S11,'uni',0);
end
R10 = cellfun(@(x,y)x+y,R10,R0temp,'uni',0);
```

```
S10 = cellfun(@(x,y)x+y,S10,S0temp,'uni',0);
R11 = cellfun(@(x,y)x+y,R11,R1temp,'uni',0);
S11 = cellfun(@(x,y)x+y,S11,S1temp,'uni',0);
RS0 = [R10,S10;R20,S20];
RS1 = [R11,S11;R21,S21];
clear R10 R20 S10 S20 R11 R21 S11 S21 R0temp S0temp R1temp S1temp;

RS0 = permute(reshape(cell2mat(RS0),length(k),nummodes*2,nummodes*2),
      [2 3 1]);
RS1 = permute(reshape(cell2mat(RS1),length(k),nummodes*2,nummodes*2),
      [2 3 1]);

% Now we calculate the coefficients.
parfor indk=1:length(k)
    AB0(:,indk)  = RS0(:,:,indk)\Ans0;
    AB1(:,indk)  = RS1(:,:,indk)\Ans1;
end

clear RS0 RS1;

A20 = AB0(1:nummodes,:).'; B20 = AB0(nummodes+1:2*nummodes,:).';
A21 = AB1(1:nummodes,:).'; B21 = AB1(nummodes+1:2*nummodes,:).';

A10 = (A20+B20)./(2*cos(kz*zP1)).*exp(-1i*kz*zP1);
B10 = A10.*exp(1i*2*kz*zP1);

A11 = (A21+B21)./(2*cos(kz*zC1)).*exp(-1i*kz*zC1);
B11 = A11.*exp(1i*2*kz*zC1);
clear Ans0 Ans1 AB0 AB1;

%% Green's Function Calculation

% Next we place those coefficients in the general function
% describing the duct, shown in Eq. (2-11).

for indz = 1:length(z)
    if z(indz)<zP1
        F0(indz,:,:)  = A10.*exp(-1i*(z(indz)-zP1)*kz)
            +B10.*exp(1i*(z(indz)-zP1)*kz);
    else
        F0(indz,:,:)  = A20.*exp(-1i*(z(indz)-zP1)*kz)
            +B20.*exp(1i*(z(indz)-zP1)*kz);
    end
    if z(indz)<zC1
        F1(indz,:,:)  = A11.*exp(-1i*(z(indz)-zC1)*kz)
            +B11.*exp(1i*(z(indz)-zC1)*kz);
    else
        F1(indz,:,:)  = A21.*exp(-1i*(z(indz)-zC1)*kz)
            +B21.*exp(1i*(z(indz)-zC1)*kz);
    end
end

clear A10 A20 A11 A21 B10 B20 B11 B21;

% Now we calculate the Green's Function over all frequencies and
% cross-modes.

```

```
G0 = zeros(length(x)*length(y),length(z)*length(k));
G1 = zeros(length(x)*length(y),length(z)*length(k));

for indmode = 1:nummodes
    PSI = Psi(:,:,indmode);
    FF0 = F0(:,:,indmode);
    FF1 = F1(:,:,indmode);
    G0 = G0+PSI(:)*FF0(:).';
    G1 = G1+PSI(:)*FF1(:).';
end
clear PSI FF0 FF1 F0conj F1conj F0 F1;

G0 = reshape(G0,length(x),length(y),length(z),length(k));
G1 = reshape(G1,length(x),length(y),length(z),length(k));

clear kz kn Psi Psi0 Psi1 Lambda D0 D1 m n u v C ...
    Gtemp0 Gtemp1 a indk indkz indx indy indz;

%% Optimal Secondary Source Strength Calculation

% Now we solve for the optimal secondary source strength Q1opt, as
% shown in Eq. (2-32).

dA = (x(2)-x(1))*(y(2)-y(1));

dG0(:,:,:) = conj(squeeze((3*G0(:,:,end,:)...
      -4*G0(:,:,end-1,:)+G0(:,:,end-2,:))/(2*(z(2)-z(1)))));
dG1(:,:,:) = conj(squeeze((3*G1(:,:,end,:)...
      -4*G1(:,:,end-1,:)+G1(:,:,end-2,:))/(2*(z(2)-z(1)))));

B = sum(sum(squeeze(G0(:,:,end,:)).*dG1,1),2)*dA;
C = sum(sum(squeeze(G1(:,:,end,:)).*dG0,1),2)*dA;
D = sum(sum(squeeze(G1(:,:,end,:)).*dG1,1),2)*dA;

Q1opt = squeeze((-imag(B+C)+1i*real(B-C))./(2*imag(D)));

clear dG0 dG1 G0conj G1conj B C D;

%% Internal Pressure and Velocity Field Calculation

p = zeros(length(x),length(y),length(z),length(k));
uz = zeros(length(x),length(y),length(k));
P = zeros(length(k),1);

p1 = zeros(length(x),length(y),length(z),length(k));
uz1 = zeros(length(x),length(y),length(k));
P1 = zeros(length(k),1);

% Finally, we calculate the pressure at any point in the duct, where Q
% is the strength of the primary source and Q1opt is the optimal
% secondary source strength solve for above. The variable p is the
% uncontrolled pressure while the variable p1 is the controlled
%  pressure.  P  is  the  uncontrolled  power  while  P1  is  the  controlled
% power.

for indk=1:length(k);

```

```
    p(:,:,:,indk) = 1i*k(indk)*c*p0*(Q0*G0(:,:,:,indk));
    p1(:,:,:,indk) = ...
      1i*k(indk)*c*p0*(Q0*G0(:,:,:,indk)+Q1opt(indk)*G1(:,:,:,indk));

    uz(:,:,indk) = 1i/(p0*k(indk)*c)*squeeze((3*p(:,:,end,indk)...
      -4*p(:,:,end-1,indk)+p(:,:,end-2,indk))/(2*(z(2)-z(1))));
    uz1(:,:,indk) = 1i/(p0*k(indk)*c)*squeeze((3*p1(:,:,end,indk)...
      -4*p1(:,:,end-1,indk)+p1(:,:,end-2,indk))/(2*(z(2)-z(1))));

    P(indk) = sum(sum(1/2*real(squeeze(p(:,:,end,indk))...
        .*conj(uz(:,:,indk)))))*dA;
    P1(indk) = sum(sum(1/2*real(squeeze(p1(:,:,end,indk))...
        .*conj(uz1(:,:,indk)))))*dA;

end
clear G0 G1 temp indk;

% Now we take the difference between the controlled and uncontrolled
% pressure. This accentuates nodal lines that appear due to the effects
% of the secondary source.

ptot = 20*(log10(abs(p1(:,:,:,:)))-log10(abs(p(:,:,:,:))));

toc

%% Radiated Pressure and Velocity Field Calculation

%  Now  we  define  the  variables  that  describe  the  infinite  baffle  in
which
% the duct is set. This baffle forms the boundary of our half-space.

xout = 0:.001:.15;
yout = 0:.001:.2;
pout = zeros(length(k),length(xout),length(yout));
pout1 = pout;
xd = (max(xout)-Lx)/2;
yd = (max(yout)-Ly)/2;

% Now we calculate the pressure along the face of the baffle due to the
% radiation from the duct through Rayleigh's integral, shown in Eq.
% (2-33).

C = 1i*k.'*c*p0/(2*pi);
for indy = 1:length(y)
    ytemp = y(indy);
    for indx = 1:length(x)
        uztemp = C.*squeeze(uz(indx,indy,:));
        uz1temp = C.*squeeze(uz1(indx,indy,:));
        xtemp = x(indx);
        for indyout = 1:length(yout)
            youttemp = yout(indyout);
            for indxout = 1:length(xout)

                R = sqrt(abs(xd-xout(indxout)+xtemp)^2+...
                    (abs(yd-youttemp+ytemp))^2);

                pout(:,indxout,indyout) = pout(:,indxout,indyout)+...
```

```
                    uztemp.*exp(-1i*k.'*R)/R;

                pout1(:,indxout,indyout) = pout1(:,indxout,indyout)+...
                    uz1temp.*exp(-1i*k.'*R)/R;

            end
        end
    end
    y(indy)
end

pout = pout*dA;
pout1 = pout1*dA;

% We again take the difference between the controlled and uncontrolled
% pressure. This accentuates nodal lines that appear due to the effects
% of the secondary source.

pouttot = 20*(log10(abs(pout1(:,:,:)))-log10(abs(pout(:,:,:))));

matlabpool close;

clear xtemp ytemp youttemp indx indy indxout indyout C;

toc
```

C.2 Radiation Impedance MATLAB Code

```matlab
%% Multimodal Radiation Impedance Calculator for a Baffled Rectangular Duct

% Based on Kemp, J. A., Campbell, D. M., and Amir, N. (2001).
% "Multimodal Radiation Impedance of a Rectangular Duct Terminated in
% an Infinite Baffle," Acta Acustica 87, 5.

% James Esplin
% 7/26/10

clc;
close all;
clear all;

matlabpool close force local
matlabpool

% First, we define how many modes we wish to compute, some physical
% constants, and the dimensions of the duct.

nummodes = 8; % # of modes
p0 = 1.21; % Density of fluid
c = 343; % Speed of Sound

% Dimensions of the duct
Lx = .048;
Ly = .01;

% Now we define the frequency range of interest.

f = 500:2000; % Frequency

k = 2*pi/c*f; % Wavenumber

% Now we define the constant that is multiplied by all terms in Kemp's
% equation, also shown in Eq. (2-15).

C = 1i*p0*c/(2*pi*Lx*Ly);

% Now we find the modal indices that correspond to the modes we wish to
% include in the calculation.

fres = zeros(nummodes,nummodes);
for m = 0:nummodes-1;
    for n = 0:nummodes-1;
        fres(m+1,n+1) = c/2*sqrt((m/Lx)^2+(n/Ly)^2);
    end
end

[temp,fresind] = sort(fres(:));
[fresx,fresy] = ind2sub([nummodes,nummodes],fresind);
clear fres fresind;
```

```
fresx = fresx-1;
fresy = fresy-1;
fresx = fresx(1:nummodes).';
fresy = fresy(1:nummodes).';

Zradtemp = zeros(length(k),1);
Z1error = zeros(length(k),1);
Z2error = zeros(length(k),1);
Zrad = cell(nummodes);
Zerror = cell(nummodes);

%% Multimodal Radiation Impedance Calculation

tic

% Now we start calculation of the multimodal radiation impedance. Note
% the triple for loop--one for the velocity modes (m), one for the
% pressure modes (n), and one for the frequency index.

for indm = 1:8
    mx = fresx(indm);
    my = fresy(indm);
    for indn = 1:indm
        nx = fresx(indn);
        ny = fresy(indn);

        m = find(fresx == mx & fresy == my);
        n = find(fresx == nx & fresy == ny);

        parfor indk = 1:length(k)

            % Here we calculate N for pressure and velocity modes
            % for both x and y, as given in Eq. (2-19).

            if mx == 0
                Nmx = 1;
            else
                Nmx = sqrt(2);
            end
            if nx == 0
                Nnx = 1;
            else
                Nnx = sqrt(2);
            end
            if my == 0
                Nmy = 1;
            else
                Nmy = sqrt(2);
            end
            if ny == 0
                Nny = 1;
            else
                Nny = sqrt(2);
            end

            % Here we determine the value of f_{m,n} as listed in
            % the Kemp paper and in Eq. (2-17).
```

```

fmn = Nmx*Nnx*Nmy*Nny*...
    (sinc((mx+nx))+sinc((mx-nx)))*...
    (sinc((my+ny))+sinc((my-ny)));

% Here we start the integration code.

% Gx and Gy are the Green's functions as defined in
% the paper and in Eq. (2-16).

Gx = @(u) Nmx.*Nnx...
    .*(cos((mx-nx).*pi.*u./(2.*k(indk).*Lx)).*...
    1/2.*((2.*Lx-u./k(indk)).*sinc((mx+nx)...
    .*(1-u./(2.*k(indk).*Lx)))-...
    u/k(indk).*sinc((mx+nx).*u./(2.*k(indk).*Lx)))+...
    cos((mx+nx).*pi.*u./(2.*k(indk).*Lx)).*...
    1/2.*((2.*Lx-u./k(indk)).*sinc((mx-nx)...
    .*(1-u./(2.*k(indk).*Lx)))-...
    u/k(indk).*sinc((mx-nx).*u./(2.*k(indk).*Lx))));
Gy = @(v) Nmy.*Nny...
   .*(cos((my-ny).*pi.*v./(2.*k(indk).*Ly)).*...
    1/2.*((2.*Ly-v./k(indk)).*sinc((my+ny)...
   .*(1-v./(2.*k(indk).*Ly)))-...
    v/k(indk).*sinc((my+ny).*v./(2.*k(indk).*Ly)))+...
    cos((my+ny).*pi.*v./(2.*k(indk).*Ly)).*...
    1/2.*((2.*Ly-v./k(indk)).*sinc((my-ny)...
   .*(1-v./(2.*k(indk).*Ly)))-...
    v/k(indk).*sinc((my-ny).*v./(2.*k(indk).*Ly))));

% Here we do the integration. Z1 is the double integral, Z2
% is the single integral, and Z3 is the constant at the end
% of Eq. (2-15).

Z1f = @(u,v)C.*(1-u./(2.*k(indk).*Lx))...
    .*(1-v./(2.*k(indk).*Ly))./sqrt(u.^2+v.^2).*...
    (exp(-1i.*sqrt(u.^2+v.^2)).*...
    Gx(u)./(1-u./(2.*k(indk).*Lx)).*Gy(v)...
    ./(1-v./(2.*k(indk).*Ly))-fmn);

Z2f = @(u)C.*(1-u./(2.*k(indk).*Lx)).*...
    (log(k(indk).*Ly+sqrt(u.^2+(k(indk).*Ly).^2))...
    +u/(2.*k(indk).*Ly)-...
    1/(2.*k(indk).*Ly).*sqrt(u.^2+(k(indk).*Ly).^2)).*fmn;

if rem(m+n,2)
    Z1 = dblquad(Z1f,0,Lx*k(indk),1e-20,Ly*k(indk),1e-18);
else
    Z1 = dblquad(Z1f,0,Lx*k(indk),1e-20,Ly*k(indk),1e-5);
end

Z2 = quad(Z2f,0,Lx*k(indk),1e-5);

Z3 =
(-3/4.*k(indk).*Lx.*log(k(indk).*Lx)
+7/8.*k(indk).*Lx).*fmn.*C;

% Here we add all the terms together to find the final
```

```
            % quantity.

            Zradtemp(indk) = (Z1+Z2+Z3);
        end

        sprintf('(%d,%d,%d,%d), (%d,%d)',mx,my,nx,ny,n,m)
        Zrad{n,m} = Zradtemp;
        Zerror{n,m} = [Z1error,Z2error];
    end
end

clear Zradtemp Z1error Z2error;

toc

matlabpool close;
```

C.3 *Two-Dimensional Half-Space Model MATLAB Code*

```
%% Point Source in a Two-Dimensional Half-Space Model
% James Esplin
% 6/10/11

close all;
clear all
clc;

matlabpool close force local
matlabpool

% Set Physical Constants

p0 = 1.21; % Density of air
c = 343; % Speed of sound

% Set frequency range

f = 500:1:2000;

k = 2*pi*f/c;

a = 36*.0254;

% Define primary and secondary source positions in polar coordinates,
% as well as the assumed primary source control strengths.

% Ensure these positions are in column format (; delimited).

rp = [sqrt(.073^2+.043^2);sqrt(.073^2+.043^2)];
thetap = [atan2(.073,.043);atan2(-.073,.043);];

Qp = 1*ones(length(rp),length(k));

% Ensure these positions are in column format (; delimited).

rs = [sqrt(.068^2+.088^2);...
    sqrt(.118^2+.068^2);...
    sqrt(.118^2+.023^2);...
    sqrt(.068^2+.088^2);...
    sqrt(.118^2+.068^2);...
    sqrt(.118^2+.023^2)];
thetas = [atan2(.068,.088);...
    atan2(.118,.068);...
    atan2(.118,.023);...
    atan2(-.068,.088);...
    atan2(-.118,.068);...
    atan2(-.118,.023)];

```

```
% Now we define the spatial variables r and theta.

r = 0:.0005:.2;
theta = 0:1*pi/180:pi/2;

% Now we prompt the user to confirm that the source positions entered
% are correct.

Xp = rp.*cos(thetap);
Yp = rp.*sin(thetap);

Xs = rs.*cos(thetas);
Ys = rs.*sin(thetas);

figure
h1 = plot(Xp*100,Yp*100,'o',...
    'MarkerEdgeColor','k','MarkerFaceColor','k',...
    'MarkerSize',10);
hold all;
rectangle('Position',[1.3,4.3,6,6],'LineWidth',2);
hold all;
rectangle('Position',[1.3,-4.3-6,6,6],'LineWidth',2);
hold all;
h2 = plot(Xs*100,Ys*100,'kp',...
    'MarkerEdgeColor','k','MarkerFaceColor','k',...
    'MarkerSize',12);
hold off;
legend([h1,h2],'Primary','Control','location','best')
axis equal;

Pos_Test = input('Are these the correct source positions? 1/0\n');

drawnow;

if ~Pos_Test
    matlabpool close force local
    break;
end

%% Calculation of Uncontrolled and Controlled Pressure Fields
% First, we calculate the Green's function for the 2-d waveguide, as
% given by Eq. (3-3).

tic

Hp = zeros(length(r),length(theta),length(k),length(rp));
Hs = zeros(length(r),length(theta),length(k),length(rs));

for indr = 1:length(r)
    for indp = 1:length(thetap)
        parfor indk = 1:length(k)
            Hp(indr,:,indk,indp) = ...
                  besselh(0,2,k(indk)*abs(sqrt(rp(indp)^2+r(indr).^2...
                  -2*rp(indp)*r(indr)*cos(abs(theta-thetap(indp))))));
```

```
        end
    end
    for inds = 1:length(thetas)
        parfor indk = 1:length(k)
            Hs(indr,:,indk,inds) = ...
                  besselh(0,2,k(indk)*abs(sqrt(rs(inds)^2+r(indr).^2...
                  -2*rs(inds)*r(indr)*cos(abs(theta-thetas(inds))))));
        end
    end
end

toc

% Now we calculate the Z matrices, given by Eqs. (3-11) and (3-13).

Zpp = zeros(length(rp),length(rp),length(k));

for indp1 = 1:length(rp)
    for indp2 = 1:length(rp)
        Zpp(indp1,indp2,:) = ...
            -p0*c*k/2.*besselj(0,k*abs(sqrt(rp(indp1)^2+rp(indp2)^2...
            -2*rp(indp1)*rp(indp2)...
            *cos(abs(thetap(indp1)-thetap(indp2))))));
    end
end

Zss = zeros(length(rs),length(rs),length(k));

for inds1 = 1:length(rs)
    for inds2 = 1:length(rs)
        Zss(inds1,inds2,:) = ...
            -p0*c*k/2.*besselj(0,k*abs(sqrt(rs(inds1)^2+rs(inds2)^2...
            -2*rs(inds1)*rs(inds2)...
            *cos(abs(thetas(inds1)-thetas(inds2))))));
    end
end

Zsp = zeros(length(rs),length(rp),length(k));

for inds1 = 1:length(rs)
    for indp2 = 1:length(rp)
        Zsp(inds1,indp2,:) = ...
            -p0*c*k/2.*besselj(0,k*abs(sqrt(rs(inds1)^2+rp(indp2)^2...
            -2*rs(inds1)*rp(indp2)...
            *cos(abs(thetas(inds1)-thetap(indp2))))));
    end
end

toc

% Now we solve for the optimum secondary source strength Qs (shown in
% Eq. (3-15b), the uncontrolled power P, and the minimized power Pmin.

Qs = zeros(length(rs),length(k));
P = zeros(length(k),1);
```

```
Pmin = zeros(length(k),1);

parfor indk = 1:length(k)
    Qs(:,indk) = -(1/2*Zss(:,:,indk))\(1/2*Zsp(:,:,indk)*Qp(:,indk));
    P(indk) = -(1/2*Qp(:,indk)'*Zpp(:,:,indk)*Qp(:,indk))./2;
    Pmin(indk) = (-(1/2*Qp(:,indk)'*Zpp(:,:,indk)*Qp(:,indk)...
        -(1/2*Zsp(:,:,indk)*Qp(:,indk))'...
        /(1/2*Zss(:,:,indk))*(1/2*Zsp(:,:,indk)*Qp(:,indk))))./2;
end

toc

% Finally, we calculate the uncontrolled pressure field p and the
% controlled pressure field pmin, as given by Eqs. (3-9) and (3-16)
% respectively.

p = zeros(length(r),length(theta),length(k));
pmin = zeros(length(r),length(theta),length(k));

parfor indk = 1:length(k)

    [~,~,QP] = ndgrid(r,theta,Qp(:,indk));
    QP = squeeze(QP);
    p(:,:,indk) = sum(-p0*c*k(indk)/4*QP.*squeeze(Hp(:,:,indk,:)),3);

    [~,~,QS] = ndgrid(r,theta,Qs(:,indk));
    QS = squeeze(QS);
    pmin(:,:,indk) =
      -p0*c*k(indk)/4*(sum(QP.*squeeze(Hp(:,:,indk,:)),3)+...
        sum(QS.*squeeze(Hs(:,:,indk,:)),3));

end

toc

matlabpool close
```

C.4 Two-Dimensional Modal Model MATLAB Code

```
%% Point Source in a Two-Dimensional Modal Model
% James Esplin
% 6/28/11

close all;
clear all;
clc;

% Here we define the physical constants, the dimensions of the
% rectangular enclosure, the number of modes we want to include in the
% expansion, and the amount of energy loss at the boundaries.

nummodes = 100; % # of modes
deltab = .25; % Damping factor at boundaries

p0 = 1.21; % Density of air
c = 343; % Speed of sound

% Dimensions of rectangular enclosure
Lx = (13+5/16)*.0254;
Ly = 9.75*.0254;

% Here we find the resonant frequencies and modal indices that
% correspond to the first nummodes modes.

for indfresx = 0:nummodes
    for indfresy = 0:nummodes
        fres(indfresx+1,indfresy+1) =
c*sqrt((indfresx/Lx/2)^2+(indfresy/Ly/2)^2);
    end
end

fres = reshape(fres,[],1);
[fres,fresind] = sort(fres);
fres = fres(1:nummodes+1);
fresind = fresind(1:nummodes+1);
[m,n] = ind2sub([nummodes+1,nummodes+1],fresind);
m = m-1;
n = n-1;

% Here we define our frequency range.

f = 500:1:2000;
k = 2*pi*f/c;

% Here we define the locations of our primary and secondary sources, as
% well as the primary source strength.

Ppx = [.043];
Ppy = [.073];
```

```
Psx = [.075,.075,.075];
Psy = [.073,.053,.033];

Qp = 1*ones(length(Ppx),length(k));

% Here we define our spatial measurement grid.

x = 0:.001:Lx;
y = 0:.001:Ly;

%% Calculation of Optimal Secondary Source Strengths

% Here we calculate Lambda, kn, and the matrices and vectors
% needed to solve for the minimum Qs (the secondary source strength).

kn2 = zeros(length(k),length(nummodes+1));
Lambda = zeros(length(nummodes+1),1);

PsiP = zeros(length(Ppx),length(k));
PsiS = zeros(length(Psx),length(k));

QsPsiMat = zeros(length(Psx),length(Psx),length(k));
QsPsiMatTemp = zeros(1,1,length(k));
AnsQsR = zeros(length(Psx),1,length(k));
AnsQsI = zeros(length(Psx),1,length(k));
AnsQsRTemp = zeros(1,1,length(k));
AnsQsITemp = zeros(1,1,length(k));

for indmode = 1:nummodes+1

    % Here we define the complex modal wave number, given in Eq.
    % (3-24).

    kn2(indmode) = (m(indmode)*pi/Lx)^2+(n(indmode)*pi/Ly)^2 ...
        +2i*(m(indmode)*pi/Lx)*deltab/c-(deltab/c)^2;

    % Here we define Lambda, given in Eq. (3-20).

    if m(indmode) == 0 && n(indmode) == 0
        Lambda(indmode) = 1;
    elseif (m(indmode) ~= 0 && n(indmode) == 0) || ...
            (m(indmode) == 0 && n(indmode) ~= 0)
        Lambda(indmode) = 1/2;
    else
        Lambda(indmode) = 1/4;
    end

    % Here we define the elements of Z, given in Eq. (3-27).

    for indQsr = 1:length(Psx)
        for indQsc = 1:length(Psx)
            QsPsiMatTemp(1,1,:) = real((-1i*p0*c*k)./...
                (Lx*Ly*Lambda(indmode)*(k.^2-kn2(indmode))))*...
```

```
                cos(m(indmode)*pi/Lx*Psx(indQsr))...
                *cos(n(indmode)*pi/Ly*Psy(indQsr)).*...
                cos(m(indmode)*pi/Lx*Psx(indQsc))...
                *cos(n(indmode)*pi/Ly*Psy(indQsc));
            QsPsiMat(indQsr,indQsc,:) =
                QsPsiMat(indQsr,indQsc,:)+QsPsiMatTemp;

        end
        AnsQsRTemp(1,1,:) = (real((-1i*p0*c*k)./...
            (Lx*Ly*Lambda(indmode)*(k.^2-kn2(indmode))))*...
            cos(m(indmode)*pi/Lx*Psx(indQsr))...
            *cos(n(indmode)*pi/Ly*Psy(indQsr)).*...
            ((cos(m(indmode)*pi/Lx*Ppx)...
            .*cos(n(indmode)*pi/Ly*Ppy))*real(Qp)));
        AnsQsR(indQsr,1,:) = AnsQsR(indQsr,1,:)-AnsQsRTemp;

        AnsQsITemp(1,1,:) = (real((-1i*p0*c*k)./...
                (Lx*Ly*Lambda(indmode)*(k.^2-kn2(indmode))))*...
                cos(m(indmode)*pi/Lx*Psx(indQsr))...
                *cos(n(indmode)*pi/Ly*Psy(indQsr)).*...
                ((cos(m(indmode)*pi/Lx*Ppx)...
                .*cos(n(indmode)*pi/Ly*Ppy))*imag(Qp)));
        AnsQsI(indQsr,1,:) = AnsQsI(indQsr,1,:)-AnsQsITemp;

    end
end

clear QsPsiMatTemp AnsQsRTemp AnsQsITemp;

% Here we solve for the real and imaginary parts (QsR and QsI) of the
% optimum source strength, shown in Eq. (3-29).

QsR = zeros(length(Psx),length(k));
QsI = zeros(length(Psx),length(k));

for indk = 1:length(k)
    QsR(:,indk) = QsPsiMat(:,:,indk)\AnsQsR(:,:,indk);
    QsI(:,indk) = QsPsiMat(:,:,indk)\AnsQsI(:,:,indk);
end

Qs = QsR+1i*QsI;

%% Uncontrolled and Controlled Pressure Field Calculation

% Here we calculate the uncontrolled and controlled pressure fields
% inside the laptop enclosure.

P = zeros(1,length(k));
Pmin = zeros(1,length(k));
p = zeros(length(x),length(y),length(k));
pmin = zeros(length(x),length(y),length(k));
[~,~,K] = ndgrid(x,y,k);

tic
```

```

for indmode = 1:nummodes+1

    % First, we calculate the uncontrolled power P and the minimized
    % power Pmin.

    P = P+1/2*real((-1i*p0*c*k)./...
        (Lx*Ly*Lambda(indmode)*...
        (k.^2-kn2(indmode))).*...
        ((cos(m(indmode)*pi/Lx*Ppx).*cos(n(indmode)*pi/Ly*Ppy)*Qp).*...
        (cos(m(indmode)*pi/Lx*Ppx)...
        .*cos(n(indmode)*pi/Ly*Ppy)*conj(Qp))));

    Pmin = Pmin+1/2*real((-1i*p0*c*k)./...
        (Lx*Ly*Lambda(indmode)*...
        (k.^2-kn2(indmode))).*...
        ((cos(m(indmode)*pi/Lx*Ppx).*cos(n(indmode)*pi/Ly*Ppy)*Qp).*...
        (cos(m(indmode)*pi/Lx*Ppx)...
        .*cos(n(indmode)*pi/Ly*Ppy)*conj(Qp))+...
        (cos(m(indmode)*pi/Lx*Ppx).*cos(n(indmode)*pi/Ly*Ppy)*Qp).*...
        (cos(m(indmode)*pi/Lx*Psx)...
        .*cos(n(indmode)*pi/Ly*Psy)*conj(Qs))+...
        (cos(m(indmode)*pi/Lx*Psx).*cos(n(indmode)*pi/Ly*Psy)*Qs).*...
        (cos(m(indmode)*pi/Lx*Ppx)...
        .*cos(n(indmode)*pi/Ly*Ppy)*conj(Qp))+...
        (cos(m(indmode)*pi/Lx*Psx).*cos(n(indmode)*pi/Ly*Psy)*Qs).*...
        (cos(m(indmode)*pi/Lx*Psx)...
        .*cos(n(indmode)*pi/Ly*Psy)*conj(Qs))));

    % Now we calculate the uncontrolled and controlled pressure fields,
    % given in Eqs. (3-25) and (3-30) respectively.

    Psi = repmat(cos(m(indmode)*pi/Lx*x.')*cos(n(indmode)*pi/Ly*y),...
        [1,1,length(k)]);

    Psip = permute(repmat(cos(m(indmode)*pi/Lx*Ppx)...
        .*cos(n(indmode)*pi/Ly*Ppy)*Qp,...
        [length(x),1,length(y)]),[1,3,2]);
    Psis = permute(repmat(cos(m(indmode)*pi/Lx*Psx)...
        .*cos(n(indmode)*pi/Ly*Psy)*Qs,...
        [length(x),1,length(y)]),[1,3,2]);

    p = p+(-1i*p0*c*K)./...
        (Lx*Ly*Lambda(indmode).*...
        (K.^2-kn2(indmode))).*...
        Psi.*Psip;

    pmin = pmin+(-1i*p0*c*K)./...
        (Lx*Ly*Lambda(indmode).*...
        (K.^2-kn2(indmode))).*...
        Psi.*(Psip+Psis);

    if max(indmode-1==[1,21:10:nummodes+1])
        fprintf('Completed %ist mode\n',indmode-1)
    elseif max(indmode-1==[2,22:10:nummodes+1])
```

```
        fprintf('Completed %ind mode\n',indmode-1)
    elseif max(indmode-1==[3,23:10:nummodes+1])
        fprintf('Completed %ird mode\n',indmode-1)
    else
        fprintf('Completed %ith mode\n',indmode-1)
    end
end

clear K Psi Psip Psis;

toc
```

Index